

# **Stony Brook University**



OFFICIAL COPY

**The official electronic file of this thesis or dissertation is maintained by the University Libraries on behalf of The Graduate School at Stony Brook University.**

**© All Rights Reserved by Author.**

Uncertainty Quantification and Grid-Based  
Geometrical Computations for Turbulent  
Fluid Mixing

A Dissertation Presented

by

Jean Nicolas Pestieau

to

The Graduate School in Partial Fulfillment of the Requirements for the

Degree of

Doctor of Philosophy

in

Applied Mathematics and Statistics

Stony Brook University

May 2007

Stony Brook University

The Graduate School

Jean Nicolas Pestieau

We, the dissertation committee for the above candidate for the Doctor of Philosophy degree, hereby recommend acceptance of this dissertation.

James Glimm

Advisor and Chair

Department of Applied Mathematics and Statistics

Xiaolin Li

Graduate Program Director

Department of Applied Mathematics and Statistics

Joseph Mitchell

Professor

Department of Applied Mathematics and Statistics

James Davenport

Director

Computational Science Center  
Brookhaven National Laboratory

This dissertation is accepted by the Graduate School.

Lawrence Martin

Dean of the Graduate School

## Abstract of the Dissertation

# Uncertainty Quantification and Grid-Based Geometrical Computations for Turbulent Fluid Mixing

by

Jean Nicolas Pestieau

Doctor of Philosophy

in

Applied Mathematics and Statistics

Stony Brook University

2007

There are two major parts to this thesis, both involving averaged quantities in turbulent fluid mixing. In the first part we consider the chaotic flow of a Richtmyer-Meshkov instability resulting from a shock passing through a density discontinuity. From a Bayesian uncertainty quantification framework, we use high-resolution simulations to propose convergence rates for the numerical solution and the solution error of this chaotic flow in a perturbed circular (2D) geometry. After suitable averaging procedures we obtain stable statistics in homogeneous regions for several flow quantities,

including the single-phase densities and wave positions. In the second part we turn our attention to the problem of validating a general closure by Glimm et al. for compressible multi-species, multi-phase flow models. More specifically, we discuss a grid-based algorithm we have implemented in the hydrodynamics front-tracking code *FronTier* that collects simulation data more accurately. This tool was devised to improve the data analysis of averaged quantities in 3D planar Rayleigh-Taylor simulations, a crucial component to the validation of the nonlinear interfacial terms that define the closures. Our method is conservative in nature as it uses the exact (up to modeling assumptions) volume fractions of irregular cells cut by the interface. We discuss at length the geometrical formulas used in our algorithm.

*To my parents & my sister*

# Table of Contents

<b>List of Figures</b> .....	<b>ix</b>
<b>List of Tables</b> .....	<b>xxi</b>
<b>Acknowledgements</b> .....	<b>xxiv</b>
<b>1 Introduction</b> .....	<b>1</b>
1.1 Acceleration-Driven Mixing .....	1
1.1.1 Rayleigh-Taylor Instability .....	2
1.1.2 Richtmyer-Meshkov Instability .....	4
1.2 Direct Numerical Simulations and Compressible Flow Models ..	6
1.2.1 Averaged Microphysical Equations .....	8
1.2.2 Closures .....	11
1.2.3 Validation and Comparison of Closures .....	17
1.3 The Front-Tracking Approach .....	22
<b>2 Uncertainty Quantification for a Chaotic Richtmyer-Meshkov</b>	
<b>Flow</b> .....	<b>25</b>
2.1 Introduction .....	25
2.2 Problem Formulation .....	28
2.3 Homogeneous Region Error Analysis .....	29

2.4	Position Errors of Mixing Zone Edges .....	33
2.5	Conclusions .....	35
<b>3</b>	<b>Grid-Based Geometrical Computations for Conservative Data</b>	
	<b>Collection .....</b>	<b>37</b>
3.1	Introduction .....	37
3.1.1	Objective .....	39
3.1.2	Assumptions .....	40
3.2	Corner Two-Colorings .....	41
3.3	Interface Perimeters .....	48
3.3.1	Perimeter Construction .....	48
3.3.2	Valid Triangulations of Connected Perimeters .....	56
3.4	Computational Procedure .....	65
3.4.1	Volume Fractions .....	66
3.4.2	Surface Areas .....	69
3.4.3	Formulas .....	70
3.5	Implementation in <i>FronTier</i> .....	75
3.5.1	Standard Model .....	76
3.5.2	Area and Volume Functions .....	79
<b>4</b>	<b>Appendix I – Figures and Tables for Mixing Zone Edge Errors ..</b>	<b>83</b>



<b>5 Appendix II – Proof of Proposition 3.6 .....</b>	<b>89</b>
<b>Bibliography .....</b>	<b>116</b>

## List of Figures

1.1	Early-time Rayleigh-Taylor mixing at time $t = 6$ (left) and late-Time Rayleigh-Taylor mixing at time $t = 15$ (right). The grid is $20 \times 20 \times 80$ . .....	3
1.2	Late-time density plots for tin and lucite in a simulation of Richtmyer-Meshkov mixing for a circular implosion problem. The two figures correspond to two grid levels, one fine ( $800 \times 1600$ , left) and one coarse ( $200 \times 200$ , right). .....	5
1.3	The interfacial area $A_I$ per unit volume plotted vs. time. This plot serves to define the parameter $A_I$ for the closure Saurel-2. Left: RT, Right: RM. ....	17
1.4	Comparison of the model error (1.30) for three closures. Of these, only Saurel-1 depends on the value of $A_I$ as a fitting parameter; these plots serve to locate the best fit value of $A_I$ ( $A_I = 0$ ) and thus to define the Saurel-1 closure. Left: RT, Right: RM. ....	19

1.5	Interface reconstruction using grid-free tracking (left) and grid-based tracking (right). Note the bubble/spike formation typical in acceleration-driven mixing and the frequency of ill-conditioned triangles on the right figure. <i>Figure courtesy of Glimm et al. [15].</i> .....	23
2.1	Primary waves and mean density contour plots averaged over a 45 degree circular arc at the equator of the flow region. The grid is 800 x 1600 and the initial contact is offset relative to the origin. Mixing zone edges are shown in green; the shock position is shown in red. ....	30
2.2	3D contour of the relative mean heavy density error averaged over a 5 degree arc located at the equator of the flow region. The grid level is 200 and the circular contact discontinuity is not offset relative to the origin. ....	31
2.3	Mesh convergence of the mixing zone edges position errors, in units of length (cm). The mixing zone is defined relative to the 45° window at the equator, and averaged over an ensemble of N = 5 realizations. Non-offset case. Left: Mixing zone center line. Right: Mixing zone width. ....	34

3.1	14 topologically distinct, or non-isomorphic, corner 2-colorings in 3D cells. The numbering follows the enumeration of isomorphism classes. For later use we give $f$ , the number of faces with opposite black corners, in the corner 2-colorings for which $f > 0$ . .....	44
3.2	Non-isomorphic corner 2-colorings for single cell faces. From top to bottom row, the corner 2-colorings have zero, one, or two black corners. Edge crossings are shown as small black dots. ..	49
3.3	Interface perimeters on single cell faces. They are uniquely determined by the edge crossings for cell faces with two edge crossings (left) and they are two-fold non-unique for cell faces with four edge crossings (right). Edge crossings are shown as small black dots. ....	50
3.4	32 distinct connected interface perimeters that can be formed on the surface of a 3D cell. We group the perimeters according to $f$ , the number of faces with four edge crossings, and the isomorphism classes of perimeters in each non-isomorphic case. Note that we have labeled these perimeter classes and that, in most cases, labels follow the names of polyhedra given by the number of edge crossings on the perimeter. The numbering of the non-isomorphic cases follows the enumeration of isomorphism classes for corner 2-colorings. ....	52

3.5	12 distinct disconnected interface perimeters that can be formed on a 3D cell surface, for $f = 0, 1, 2, 3$ . The numbering of the non-isomorphic cases follows the enumeration of isomorphism classes for corner 2-colorings. ....	53
3.6	48 distinct disconnected interface perimeters that can be formed on a 3D cell surface in the non-isomorphic case with $f = 6$ (case 14). ....	54
3.7	Examples of perimeters in the duodecagonoid-I (left) and duodecagonoid-II (right) isomorphism classes of connected perimeters of case 14, with $f = 6$ . ....	60
3.8	Examples of interface surfaces bounded by valid perimeters belonging to isomorphism classes of connected perimeters with $T > 0$ . They are, from left to right, starting at the top, the corner (case 1), the edge (case 2), the hexagonoid (case 3), the glider (case 5), the twisteroid (case 6), the plane (case 8), the twister-I (case 9), the twister-II (case 10), the hexagon (case 11), and the octagonoid-I (case 12). Note that the perimeter class of case 12 has two distinct elements. All triangulations are picked arbitrarily. ....	62

3.9	Valid triangulations for elements in the isomorphism classes of connected perimeters. In the table, we give for each class $f$ , the number of faces with four edge crossings on a common face; $n$ , the number of edge crossings on the perimeter; $C_{n-2}$ , the Catalan number; and $T$ , the number of valid triangulations. Only triangulations for perimeter classes with $f = 0$ were used in our implementation. In these cases, the identity $T = C_{n-2}$ holds; otherwise, $T < C_{n-2}$ . .....	64
3.10	Decomposition of the space occupied by domain 1 into five tetrahedra in one of five possible triangulations in the glider case (case 5). The crossings are the vertices $\bar{p}_i$ , where $i = 1, \dots, 5$ . The black corners are labeled $A, B$ and $C$ . .....	68
3.11	Standard model for the fourteen cases implemented in <i>FronTier</i> : 1) Plane, 2) Edge, 3) Corner, 4) Glider, 5) Hexagon, 6) Two corners-I, 7) Twister-I, 8) Edge and corner, 9) Two corners-II, 10) Twister-II, 11) Two edges, 12) Three corners, 13) Glider and corner, 14) Four corners. ....	77
3.12	Location of the cell corners used in the standard model. ....	78

4.1	Mesh convergence of the mixing zone edges position errors, in units of length (cm). The mixing zone is defined relative to the $45^\circ$ window $\theta \in [45^\circ, 90^\circ]$ at the north pole, and averaged over an ensemble of $N = 5$ realizations. Non-offset case. Left: Mixing zone center line. Right: Mixing zone width. ....	84
4.2	Mesh convergence of the mixing zone edges position errors, in units of length (cm). The mixing zone is defined relative to the $45^\circ$ window $\theta \in [-90^\circ, -45^\circ]$ at the south pole, and averaged over an ensemble of $N = 5$ realizations. Non-offset case. Left: Mixing zone center line. Right: Mixing zone width. ....	84
4.3	Mesh convergence of the mixing zone edges position errors, in units of length (cm). The mixing zone is defined relative to the $40^\circ$ window $\theta \in [50^\circ, 95^\circ]$ at the north pole, and averaged over an ensemble of $N = 5$ realizations. Offset case. Left: Mixing zone center line. Right: Mixing zone width. ....	85
4.4	Mesh convergence of the mixing zone edges position errors, in units of length (cm). The mixing zone is defined relative to the $40^\circ$ window $\theta \in [-20^\circ, 20^\circ]$ at the equator, and averaged over an ensemble of $N = 5$ realizations. Offset case. Left: Mixing zone center line. Right: Mixing zone width. ....	86

4.5	Mesh convergence of the mixing zone edges position errors, in units of length (cm). The mixing zone is defined relative to the $40^\circ$ window $\theta \in [-90^\circ, -50^\circ]$ at the south pole, and averaged over an ensemble of $N = 5$ realizations. Offset case. Left: Mixing zone center line. Right: Mixing zone width. ....	87
5.1	Examples of valid triangulations for elements in the hexagonoid (left), twisteroid (middle) and octagonoid-I (right) isomorphism classes of connected perimeters (cases 3, 6 and 12). For the left and middle figures, $f = 1$ , and for the right figure, $f = 2$ . Edge crossings belonging to a common face are labeled according to the orientation of that face, namely U, D, E, W, N, and S. Validity is then guaranteed if no edges on a common face are linked by diagonals. This is the case in all three figures: in the left, there are no $\overline{SS}$ diagonals; in the middle, there are no $\overline{EE}$ diagonals; in the right, there are neither $\overline{WW}$ nor $\overline{SS}$ diagonals. ....	90
5.2	Illustration of Lemma 5.1. $P$ is a polygon with the property that two of its adjacent edges give the sequence of vertices $(X, Y, X)$ . ....	91



- 5.3 Illustration of Proposition 5.1 showing that no valid triangulation of the hexagon  $YXXZXX$ , which excludes the diagonal  $\overline{YZ}$ , can be constructed. We show the two valid isomorphic choices for the first diagonal (left) and the only valid choice for diagonal 2 (right) resulting from applying Lemma 5.1 at vertex  $Y$ . The solid line on the left is our arbitrary choice for diagonal 1, and the dotted line is the other isomorphic choice. These two diagonals follow the symmetry about the axis passing through  $Y$  and  $Z$ . ..... 94
- 5.4 Illustration of Proposition 5.2 showing that no valid triangulation of the heptagon  $VXXYZXX$ , which excludes the two diagonals  $\overline{VY}$  and  $\overline{VZ}$ , can be constructed. We show the two valid isomorphic choices for the first diagonal (left) and the only valid choice for diagonal 2 (right) resulting from applying Lemma 5.1 at vertex  $V$ . The solid line on the left is our arbitrary choice for diagonal 1, and the dotted line is the other isomorphic choice. These two diagonals follow the symmetry about the line passing through  $V$  and the mid-point of edge  $\overline{EZ}$ . ..... 96

5.5	Illustration of Proposition 5.2 showing that no valid triangulation of the octagon $XXZYXX(XY)Y$ must include the two diagonals $\overline{ZY}$ and $\overline{ZX}$ , whose endpoints $X$ and $Y$ are adjacent to the vertex $(XY)$ . Cases a, b, and c depict the three valid non-isomorphic choices for the first diagonal. ....	99
5.6	Illustration of Lemmas 5.2 (left) and 5.3 (right). For the hexagon of Lemma 5.3 (right), we show the only valid choice for the first diagonal, which results from applying Lemma 5.1 at the $Y$ vertex adjacent to the two $X$ vertices. This leads to the pentagon of Lemma 5.2 (left). ....	101
5.7	Illustration of Lemmas 5.4 (left) and 5.5 (right). For the octagon of Lemma 5.5 (right), we show the only valid choice for the first diagonal, which results from applying Lemma 5.1 at the $(XY)$ vertex. This leads to the heptagon of Lemma 5.4 (left). ....	103
5.8	Illustration of Proposition 5.4 showing that no valid triangulation of the octagon $XXYYXXYY$ can be constructed. We show all the possible valid choices for the first diagonal, which are partitioned into two diagonal classes (a, b). Dotted lines show isomorphic choices of diagonals. Note from the many isomorphic choices of diagonals, in both classes, the high number of symmetry axes in this case. ....	104

5.9	Examples of perimeters in the octagonoid-II (left) and enneagonoid (right) isomorphism classes of connected perimeters of cases 13 ( $f = 2$ ) and 7 ( $f = 3$ ). All elements in these two perimeter classes are invalid. ....	105
5.10	Illustration of Proposition 5.5 showing that the enneagon $XXYYZZ(XY)ZZ$ has no valid triangulations. We depict the two valid isomorphic choices for the first diagonal resulting from applying Lemma 5.1 at the $(XY)$ vertex. ....	106
5.11	Illustration of Proposition 5.6 showing that the duodecagon $(XP)PY(YP)(PR)(YR)(YQ)(QR)(XR)(XQ)QX$ has no valid triangulations. Cases a, b, and c depict the three non-isomorphic valid choices for the first diagonal. We also show the only valid possibility for diagonal 2 in case b. Solid lines depict the arbitrary choices of diagonals, while dotted lines depict other isomorphic choices. Note that isomorphic diagonals follow the symmetry about the axis passing through vertices $(YQ)$ and $(XP)$ , which separates quintuplets of vertices according to the vertex inversions $X \leftrightarrow P$ and $Q \leftrightarrow Y$ . ....	108

5.12 Illustration of Proposition 5.7 showing that no valid triangulations of the duodecagon  $(XP)(XR)(QR)(YQ)(YZ)(ZQ)(XQ)(XZ)(ZP)(YP)(YR)(PR)$  can be constructed if the diagonal  $\overline{(PR)(ZQ)}$ , the triangle  $(YR)(XP)(ZQ)$ , and the triangle  $(YZ)(XQ)(PR)$  are all excluded. The four vertices in boxes have adjacent vertices on a common cell face. We show the five valid isomorphism classes (cases a through e) for the first diagonal, and the valid isomorphism classes for the second diagonal, all resulting from applying Lemma 5.1 at boxed vertices. Dotted lines depict isomorphic choices of diagonals with respect to the two symmetries about the axis passing through vertices  $(ZQ)$  and  $(PR)$  separating two quintuplets of vertices according to the vertex inversions  $X \leftrightarrow Y$ ,  $P \leftrightarrow R$ , and  $Z \leftrightarrow Q$ , and about the axis passing through vertices  $(ZP)$  and  $(QR)$  separating quintuplets of vertices according to the vertex inversions  $X \leftrightarrow Y$ ,  $Z \leftrightarrow P$ , and  $Q \leftrightarrow R$ . ..... 110

5.13 Illustration of Corollary 5.7. We show that there are  $T = 294$  valid triangulations for duodecagons in the duodecagonoid-II perimeter class resulting from the inclusion of either the diagonal  $\overline{(PR)(ZQ)}$  (a), the triangle  $(YR)(XP)(ZQ)$  (b), or the triangle  $(YZ)(XQ)(PR)$  (c). We depict in boxes the four vertices from which a diagonal must start, according to Lemma 5.1, and with heavy lines the diagonal or triangle that has been included. We only show the possible triangulations on the left side of the diagonal or triangle that is included, since there is a symmetry about the axis passing through vertices  $(PR)$  and  $(ZQ)$  separating two quintuplets of vertices according to the vertex inversions  $X \leftrightarrow Y$ ,  $P \leftrightarrow R$ , and  $Z \leftrightarrow Q$ . In all three cases, we force the first diagonal on the left to start at the vertex  $(YR)$ . ..... 113

## List of Tables

1.1	Summary of $d_k^q$ parameter choices for RT and RM mixing. All choices except that for $d_k^v$ in the RT case are insensitive. ...	15
1.2	Model errors based on comparison to simulation data. ....	19
1.3	Summary properties related to the closures $q^*$ . It is remarkable that the closures depend sensitively on their defining parameter $d_k$ only in the case of the RT data for the $v^*$ closure. ....	21
2.1	Convergence statistics for the errors in the mixing zone edges, averaged over time values and over an ensemble of size $N = 5$ (* $N = 1$ ), in units of cm. Edge position defined relative to an angular window $\theta \in [-45^\circ, 0^\circ]$ . Non-offset case. ....	35

2.2	<p>Summary of convergence properties for and orders, for the heavy and light densities <math>\rho_h</math> and <math>\rho_l</math>, volume fraction <math>\beta</math>, shock position <math>s</math> and mixing zone edges <math>mz</math>. All quantities are averaged over an angular variable, and also over all variables not explicitly present in the table. The variable <math>\rho_h</math> is an ensemble realization variable. The same quantities located in distinct columns indicate possible qualitatively different convergence behavior for distinct realizations, or for different angular regions, or as a distinction between offset and non-offset behavior. ....</p>	36
3.1	<p>Properties of all the valid interface perimeters in 3D cells. Lower roman letters indicate the number of distinct interface perimeters with similar connected components. Note that there are two distinct interface perimeters with two corners, one corresponding to the non-isomorphic case 3, and the other corresponding to the non-isomorphic case 4. Also note that all perimeters with hexagonoid, twisteroid and octagonoid-I components (in bold) were excluded in our implementation. ...</p>	72
4.1	<p>Convergence statistics for the errors in the mixing zone edges, averaged over time values and over an ensemble of size <math>N = 5</math>, in units of cm. Edge position defined relative to the angular window <math>\theta \in [45^\circ, 90^\circ]</math> at the north pole. Non-offset case. ....</p>	83

4.2	Convergence statistics for the errors in the mixing zone edges, averaged over time values and over an ensemble of size $N = 5$ , in units of cm. Edge position defined relative to the angular window $\theta \in [-90^\circ, -45^\circ]$ at the south pole. Non-offset case. ...	85
4.3	Convergence statistics for the errors in the mixing zone edges, averaged over time values and over an ensemble of size $N = 5$ , in units of cm. Edge position defined relative to the angular window $\theta \in [50^\circ, 90^\circ]$ at the north pole. Offset case. ....	86
4.4	Convergence statistics for the errors in the mixing zone edges, averaged over time values and over an ensemble of size $N = 5$ , in units of cm. Edge position defined relative to the angular window $\theta \in [-20^\circ, 20^\circ]$ at the equator. Offset case. ....	87
4.5	Convergence statistics for the errors in the mixing zone edges, averaged over time values and over an ensemble of size $N = 5$ , in units of cm. Edge position defined relative to the angular window $\theta \in [-90^\circ, -50^\circ]$ at the south pole. Offset case. ....	88



## **Acknowledgements**

I would like to extend my deepest gratitude to my advisor, Professor James Glimm, for his guidance and support in these past four years. His experience, dedication and formidable knowledge were a constant source of inspiration to me. I will forever treasure his teachings and hope to emulate in my professional life the rigor and integrity he brings to the scientific endeavor.

I would like to thank Professor Xiaolin Li for his kind and insightful help throughout my years of study and research. He is a remarkable teacher and an exceptional scientist and I was fortunate to have learned so much from him in my time here.

I would also like to extend my thanks and appreciation to Professor Joseph Mitchell, whose help on a fundamental triangulation question proved to be a turning point in my work on devising grid-based geometrical formulas, and to Dr. James Davenport, who kindly accepted to make the journey from Brookhaven National Laboratory and join this committee.

I would like to thank my peers and friends at Stony Brook, both inside and outside the Department, for their constant help and kindness.

Finally, I would like to extend my love and gratitude to my sister, Sarah, and to my parents who never stopped supporting me, even half a world away.

# Chapter 1

## Introduction

### 1.1 Acceleration-Driven Mixing

In this work we discuss the following two problems:

1. The uncertainty quantification - through convergence rates - of a chaotic flow in a perturbed circular (2D) geometry.
2. The grid-based computations of volume fractions and surface areas in 3D grid cells cut by a two-phase interface for the conservative collection of data in compressible flow problems.

Both of these problems involve acceleration-driven mixing processes which, in turn, lead to hydrodynamic instabilities (the Richtmyer-Meshkov and Rayleigh-Taylor instabilities, respectively) characterized by the formation of well-defined coherent structures in the outer portions of the mixing layer.

### 1.1.1 Rayleigh-Taylor Instability

This type of instability owes its name to the British physicists Lord Rayleigh and Sir Geoffrey Taylor. The instability was first discovered by Rayleigh in the 1880's in the case of a heavy and a light fluid mixing in a uniform gravitational field. Taylor later applied this process to all accelerating fluids in 1950 [37]. As the Rayleigh-Taylor (RT) instability develops, the perturbations in the initial contact (*i.e.*, the material interface between the fluids) lead to the formation of bubbles and spikes. In particular, bubbles of light fluid tend to rise up into the heavier fluid while spikes, or “fingers”, of heavy fluid tend to move downward into the lighter fluid. Fig. 1.1 shows early and late times in the development of the instability computed on a 20 x 20 x 80 3D rectangular grid. In the early non-linear regime of the instability, the growth is typically studied using Layzer's model [26] which gives a constant rate of bubble growth using the bubble radius and the gravitational acceleration. However, this model fails for non-planar geometries. A generalization of this model was provided by Kidder [23] using a self-similar spherical implosion. His work showed that after the early-time linear bubble rise rate (with constant velocity) of Layzer's model there is an acceleration of the bubble rise rate in later times, when the instability has gone fully non-linear.

More recently, George et al. [12–14] conducted a Rayleigh-Taylor simulation using the high-resolution front-tracking code *FronTier*, which prevents interfacial mass diffusion, as well as untracked simulations for comparison. The acceleration rates in the tracked simulations were found to fall within the range of experiments. Their results show that the lower acceleration rate found

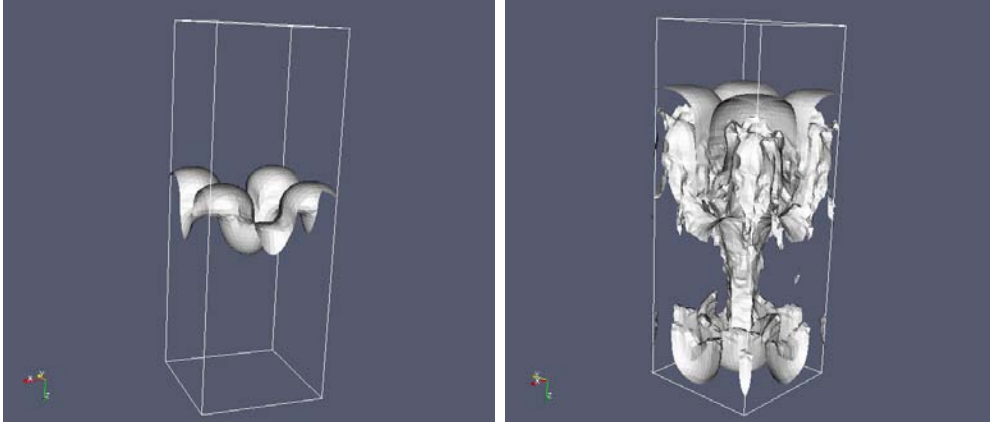


Figure 1.1: Early-time Rayleigh-Taylor mixing at time  $t=6$  (left) and late-time Rayleigh-Taylor mixing at time  $t=15$  (right). The grid is  $20 \times 20 \times 80$ .

in the untracked simulations, such as simulations based on the total variation diminishing (TVD) method, is caused, to a large extent, by a reduced buoyancy force due to numerical interfacial mass diffusion. Thus, all values of the acceleration rate  $\alpha$  (theoretical, experimental, and from simulation), which is defined in the equation

$$h(t) = \alpha A g t^2 \tag{1.1}$$

for bubble height penetration  $h$ , Atwood number  $A = \frac{\rho_2 + \rho_1}{\rho_2 - \rho_1}$  relating the initial phase pressures, gravitational acceleration  $g$ , and time  $t$ , are consistent if the diffusive calculation of  $\alpha$  is renormalized to  $\alpha_{eff}$  using a time dependent Atwood number  $A = A(t)$  to account for mass diffusion. In this case, Eq. 1.1 is rewritten as

$$h(t) = \alpha_{eff} \int_0^t \int_0^{s_1} 2A(s)g ds ds_1 \quad (1.2)$$

See [13] for these latest developments.

We note that the study of Rayleigh-Taylor instabilities is particularly of interest in the study of supernovae explosions, where the instance of a light fluid accelerating against a heavy fluid often occurs. Understanding the mixing rate caused by Rayleigh-Taylor instabilities is also essential to a wide variety of applications, including the design of inertial confinement fusion (ICF) targets and nuclear weapons explosions.

### 1.1.2 Richtmyer-Meshkov Instability

The Richtmyer-Meshkov (RM) instability, which occurs on impulsively-accelerated, or shock-accelerated, density interfaces is also essential in the study of supernovae explosions, ICF, and other practical processes. Moreover, it is a particularly meaningful and convenient test problem for turbulence studies as experimental measurements of the instability provide benchmarks for validation and verification of numerical codes modeling turbulent flows.

It was Markstein who first considered in [28] the case of an interface under impulsive acceleration produced by shock interaction. In 1960, Richtmyer provided the first rigorous treatment of this particular instability through his theoretical and numerical analysis [33]. In 1969, Meshkov's shock-tube work would provide an experimental basis for Richtmyer's predictions [29].

As with the Rayleigh-Taylor instability, the initial perturbations at the

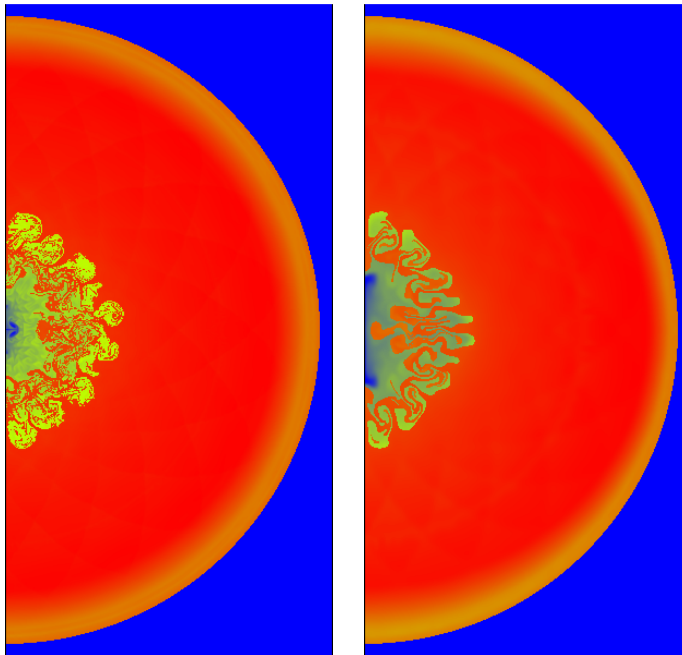


Figure 1.2: Late-time density plots for tin and lucite in a simulation of Richtmyer-Meshkov mixing for a circular implosion problem. The two figures correspond to two grid levels, one fine ( $800 \times 1600$ , left) and one coarse ( $200 \times 400$ , right).

surface of the contact interface between two fluids will grow larger in amplitude once the shock passes through the interface. Thus, if the initial setup consists of a multi-mode perturbed sinusoidal interface between two fluids, one heavy and one light, the perturbations will then grow in amplitude and develop into crests and troughs. These will tend to grow linearly up to a certain point (especially for low initial amplitudes and early times) until the instability has gone into a fully non-linear regime and the mixing layer becomes highly turbulent. At that point, the same formations observed in Rayleigh-Taylor mixing of light bubbles and heavy spikes will develop with the additional features of a roll-up, or “mushrooming”, of the bubbles (due to vorticity diffusion effects) as well as the appearance of smaller-scale structures [4]. Fig. 1.2 shows late-time density plots of tin and lucite subjected to a strong inward shock and Richtmyer-Meshkov mixing for two grid levels, one coarse and one fine, in a circular geometry.

## **1.2 Direct Numerical Simulations and Compressible Flow Models**

In order to study the numerical errors and the convergence properties of several averaged quantities that characterize the flow, or for the purposes of validating proposed closures for systems of fluid dynamic equations, our research program always starts from a series of high-resolution numerical simulations. We use direct numerical simulations (DNS) of the microphysical equations of fluid mixing to extract the data that is subsequently used in our

analysis [2]. The diversity of approaches and the vast spectrum of models that have been put forth by the scientific community in the theoretical study of compressible multi-species, multi-phase fluid mixing is remarkable. Some of these include phenomenological mixing models, hybrid turbulent mixing models, multi-fluid interpenetration mixing models and buoyancy drag models [5]. Our approach for modeling compressible multi-species, multi-phase flow is based on the single-phase averaging of the microphysical fluid equations (Euler equations) over an infinite ensemble of flow realizations, as explained in detail by Glimm et al. in [3, 21]. The following exposition is based on the latest developments discussed in [3].

The ensemble-averaging process is applied to a microphysical description of distinct fluids separated by a sharp interface (the DNS description) and leads to undefined averages of nonlinear quantities in the primitive variables. These need to be modeled in order to close the system of equations. Assuming homogeneity and the absence of internal length scales within the mixing zone, a general closure is proposed in the form of integral identities based on exact interfacial terms. These closures satisfy conservation and boundary constraints for the continuity and momentum equations and also allow important scale-breaking phenomena in the equations of motion, such as mass diffusion and surface tension. Moreover, they are validated against experimental and numerical data. The model is valid for acceleration-driven mixing processes, including Rayleigh-Taylor and Richtmyer-Meshkov mixing. With the trajectories or velocities of the mixing zone edges as the phenomenological input (and without adjustable parameters for added mass, buoyancy and drag, which are



typically treated phenomenologically), it is capable of describing the coherent structures dominating the mixing zone (the bubbles and spikes in the outer layer).

### 1.2.1 Averaged Microphysical equations

For simplicity, we consider two-phase flow equations. Let the function  $X_k$  be the phase indicator for material  $k$  ( $k = 1, 2$ ). So  $X_k(t, \mathbf{x})$  equals 1 if position  $\mathbf{x}$  is in fluid  $k$  at time  $t$ , otherwise it is zero. Let us apply the averaging process to the microphysical equations. We average the advection law [11] for the indicator function  $X_k$  of the region occupied by the fluid  $k$ ,

$$\frac{\partial X_k}{\partial t} + v_{\text{int}} \cdot \nabla X_k = 0 . \quad (1.3)$$

Here  $v_{\text{int}}$  is the microphysical velocity evaluated at the interface (the velocity component normal to the boundary  $\partial X_k$  is continuous so that  $v_{\text{int}} \cdot \nabla X_k$  is well defined).

We also average the microscopic conservation equations (continuity, momentum and energy equations):

$$\frac{\partial \rho}{\partial t} + \nabla \cdot \rho \mathbf{v} = 0 , \quad (1.4)$$

$$\frac{\partial \rho \mathbf{v}}{\partial t} + \nabla \cdot \rho \mathbf{v} \mathbf{v} = -\nabla p + \rho g , \quad (1.5)$$

$$\frac{\partial \rho E}{\partial t} + \nabla \cdot \rho \mathbf{v} E = -\nabla \cdot p \mathbf{v} + \rho \mathbf{v} g . \quad (1.6)$$

As usual,  $\mathbf{v}$ ,  $\rho$ ,  $p$ , and  $E$  denote, respectively, the velocity, density, pressure, and total energy with  $E = e + \mathbf{v}^2/2$  where  $e$  is the internal energy.

To account for scale-breaking physics, such as mass diffusion or surface tension, new terms must be added on the right-hand side of these equations. See [3] for equations that account for surface tension and transport. For simplicity we assume no mass diffusion across an interface for mixing processes with immiscible fluids. Additionally, we can assume no surface tension for mixing with miscible fluids.

Applying the ensemble average to Eqs. (1.3)-(1.6), we typically consider averaged equations with one dependent space variable (say, in the  $z$ -direction for a planar case) so that the ensemble to be averaged is independent of the missing variables. The ensemble average then includes an averaging over the suppressed spacial variables. To allow for statistical ensembles possessing cylindrical or spherical geometry we introduce the geometry indicator  $s$ , where  $s = 0, 1, 2$  corresponds to planar, cylindrical and spherical forms of the conservation equations. When the equations are averaged in cylindrical or spherical coordinates, covariant centrifugal forces due to the curvilinearity of the coordinate systems are introduced into the averaged equations.

Multiphase equations for the phase  $k$  are obtained by multiplying Eqs. (1.3)-(1.6) by  $X_k$  and performing an ensemble average. We denote the ensemble average  $\langle \cdot \rangle$ . The average  $\langle X_k \rangle$  of the indicator function  $X_k$  is denoted  $\beta_k$ ;  $\beta_k(z, t)$  is then the expected fraction of the horizontal layer at height  $z$  that is occupied by fluid  $k$  at time  $t$ . The quantities  $\rho_k$  and  $p_k$  are, respectively, phase averages of the density  $\rho$  and pressure  $p$ :

$$\rho_k = \frac{\langle X_k \rho \rangle}{\langle X_k \rangle}, \quad p_k = \frac{\langle X_k p \rangle}{\langle X_k \rangle}. \quad (1.7)$$

The quantities  $v_k$  and  $E_k$  are phase mass-weighted averages of the fluid  $z$ -velocity  $v_z$  and total energy  $E$ :

$$v_k = \frac{\langle X_k \rho v_z \rangle}{\langle X_k \rho \rangle}, \quad E_k = \frac{\langle X_k \rho E \rangle}{\langle X_k \rho \rangle}. \quad (1.8)$$

Applying the ensemble average to Eqs. (1.3)-(1.6), we obtain the one-dimensional, two-pressure, two-phase flow averaged equations:

$$\frac{\partial \beta_k}{\partial t} + \langle \mathbf{v} \cdot \nabla X_k \rangle = 0, \quad (1.9)$$

$$\frac{\partial(\beta_k \rho_k)}{\partial t} + \frac{1}{z^s} \frac{\partial}{\partial z} (z^s \beta_k \rho_k v_k) = 0, \quad (1.10)$$

$$\frac{\partial(\beta_k \rho_k v_k)}{\partial t} + \frac{1}{z^s} \frac{\partial}{\partial z} (z^s \beta_k \rho_k v_k^2) + \frac{\partial(\beta_k p_k)}{\partial z} = \left\langle p \frac{\partial X_k}{\partial z} \right\rangle + \beta_k \rho_k g, \quad (1.11)$$

$$\frac{\partial(\beta_k \rho_k E_k)}{\partial t} + \frac{1}{z^s} \frac{\partial}{\partial z} [z^s \beta_k v_k (\rho_k E_k + p_k)] = \langle p \mathbf{v} \cdot \nabla X_k \rangle + \beta_k \rho_k v_k g, \quad (1.12)$$

for the volume fraction  $\beta_k$ , velocity  $v_k$ , density  $\rho_k$ , pressure  $p_k$ , and total energy  $E_k$  of phase  $k$ . Here  $k = 1 = b$  (bubble) and  $k = 2 = s$  (spike) denote the light and heavy fluids respectively,  $k' = 3 - k$  and  $g = g(t) > 0$  is the gravitational acceleration.

We add further terms to the right-hand side of these equations when considering surface tension and transport effects, as shown in [3].

## 1.2.2 Closures

Let  $v^*$ ,  $p_k^*$  and  $(p_kv)^*$  denote the averaged quantities at the interface. These interfacial terms are given by

$$v^* = \frac{\langle \mathbf{v} \cdot \nabla X_k \rangle}{\langle \mathbf{n}_3 \cdot \nabla X_k \rangle}, \quad p_k^* = \frac{\langle p_k \mathbf{n}_3 \cdot \nabla X_k \rangle}{\langle \mathbf{n}_3 \cdot \nabla X_k \rangle}, \quad (p_kv)^* = \frac{\langle p_k \mathbf{v} \cdot \nabla X_k \rangle}{\langle \mathbf{n}_3 \cdot \nabla X_k \rangle}, \quad (1.13)$$

where  $\mathbf{n}_3$  is the unit normal vector in the preferred direction. Although the equations (1.13) allow multiple fluids, they only allow a single interface type (*i.e.*, at most two fluid phases). A generalization [10] of this framework to multiple phases specifies an interface type for each pair of phases that are in contact, and leads to a generalization of the system (1.13).

The definitions (1.13) are fundamental to all that follows. They are mathematically exact consequences of the averages of Eqs. (1.4)-(1.6) and specify the quantities (the right hand side of (1.13)) that are to be approximated in a definition of closure to complete the averaged equations (1.9)-(1.12).

Note that  $\nabla X_k$  equals the unit normal to the boundary  $\partial X_k$  times a delta function concentrated on  $\partial X_k$ . The definitions assume that interface fluxes weighted by this vector measure are proportional to fluxes through the  $z$  direction only. Also for an interface quantity such as  $p^*$ , which may be discontinuous across the interface (due to surface tension), the notation  $p_k^*$  indicates evaluation from the interior  $X_k$  side of  $\partial X_k$ .

Here we explain the basic ideas of our proposed closures, and their relation to the closures of Saurel and coworkers [1, 34, 35]. There are three terms to

define in (1.13),  $v^*, p^*, (pv)^*$ , the interface averages of  $p, v, pv$ , which we denote generically as  $q^*$ ,  $q = v, p, pv$ . For the Saurel et al. closed equations, these same quantities are also required (and have different definitions). Their equations contain additional terms called relaxation terms.

We assume a closure which represents  $q^*$  as a convex sum of the primitive variables  $q_k$  for  $q = v, p$ ,

$$q^* = \mu_1^q q_2 + \mu_2^q q_1, \quad q = v, p \quad (1.14)$$

and a related bilinear expression

$$(pv)^* = p^*(\mu_1^{pv} v_2 + \mu_2^{pv} v_1) + v^*(\mu_1^{pv} p_2 + \mu_2^{pv} p_1) - (\mu_1^{pv} p_2 v_2 + \mu_2^{pv} p_1 v_1) \quad (1.15)$$

for  $(pv)^*$ .

Saurel et al. employ a related but different functional form for their closure. They also consider a convex sum

$$q'^{S*} = \mu_1^{Sq} q_2 + \mu_2^{Sq} q_1 \quad q = v, p, \quad (1.16)$$

and then define

$$v^{S*} = v'^{S*} + \operatorname{sgn} \left( \frac{\partial \beta_1}{\partial x} \right) \frac{p_2 - p_1}{\mathcal{Z}_1 + \mathcal{Z}_2}, \quad (1.17)$$

$$p^{S*} = p'^{S*} + \operatorname{sgn} \left( \frac{\partial \beta_1}{\partial z} \right) \left( \frac{\mathcal{Z}_1 \mathcal{Z}_2}{\mathcal{Z}_1 + \mathcal{Z}_2} \right) (v_2 - v_1). \quad (1.18)$$

Here  $\mathcal{Z}_k$  is the acoustic impedance of fluid  $k$ . Also

$$(pv)^{S*} = p^{S*} v^{S*} . \quad (1.19)$$

The Saurel closures also include relaxation, as an additional term in the RHS of the associated volume fraction, momentum and energy equations.

These terms (for  $k = 1$ ) have the form:

$$\mu^S(p_1 - p_2) \quad \text{volume fraction source term} \quad (1.20)$$

$$\lambda^S(v_2 - v_1) \quad \text{momentum source term} \quad (1.21)$$

$$\lambda^S v'^{S*}(v_2 - v_1) - \mu^S p'^{S*}(p_1 - p_2) \quad \text{energy source term} \quad (1.22)$$

Here

$$\mu^S = \frac{A_I}{2(\mathcal{Z}_1 + \mathcal{Z}_2)} , \quad \lambda^S = \mu \mathcal{Z}_1 \mathcal{Z}_2 , \quad (1.23)$$

where  $A_I$  is the interfacial area per unit volume.

The convex coefficients  $\mu_k^q$  and  $\mu_k^{Sq}$  have a fractional linear form, namely

$$\mu_k^q = \frac{\beta_k}{\beta_k + d_k^q \beta_{k'}} , \quad q = v, p, pv \quad (1.24)$$

$$\mu_k^{Sq} = \frac{1}{1 + d_k^{Sq}} , \quad q = v, p \quad (1.25)$$

The  $\mu_k^q$  and  $\mu_k^{Sq}$  thus depend on a single parameter  $d_k^q$  or  $d_k^{Sq}$ . The form of the  $\mu_k^q$  is suggested by rewriting the exact equations to derive an exact (unclosed) expression for  $q^*$  and  $\mu_k^q$ . See theorems in [3] for these results. The form (1.24) of  $\mu_k^q$  is motivated by these expressions as well and is, moreover,

required by theoretically required boundary conditions at the edges of the mixing zone,

$$q^* = q_k \quad \text{at} \quad z = Z_k . \quad (1.26)$$

Our closures satisfy (1.26). A preliminary choice of  $d_k^q$ , motivated by a homogenization of the exact expressions mentioned above, is given in [3]. In all but one case, the  $d_k^q$  are insensitive and are arbitrarily set to 1. See Table 1.1.

For the RT case, we assume  $(-1)^k V_k = (-1)^k \dot{Z}_k \geq 0$  so that the mixing zone is expanding. The growing mixing zone entrains pure phase fluid into the mixture, and thus creates mixed fluid volume for both phases. In the incompressible, non-diffusive RT case, this is seen clearly from the closed form solution

$$d_k^v(t) = \left( \frac{Z_{k'}}{Z_k} \right)^s \left| \frac{V_{k'}}{V_k} \right| . \quad (1.27)$$

The solution (1.27) is a consequence of the closed form expression obtained for the solution of the model equations and a simple calculation. See references of Glimm, Sharp and Saltz [17–19] for details of the derivation. In the planar case ( $s = 0$ ), the ratio in (1.27) is a function of the Atwood number  $A = (\rho_2 - \rho_1)/(\rho_2 + \rho_1)$ , and can be determined exactly on the basis of a theory [6, 7] which has been validated against experiments. For the data (Atwood number) considered here, (1.27) has the value 1.5. The final choice of the  $d_k^q$  to complete the model definition is specified in Table 1.1.

The hyperbolic character of the resulting model equations is easily derived, but this analysis reveals a missing internal boundary condition at each edge of the mixing zone. At the edges of the mixing zone, the hyperbolic

	RT	RM
$d_1^v$	(1.27)	1.0
$d_1^p$	1.0	1.0
$d_1^{pv}$	1.0	1.0

Table 1.1: Summary of  $d_k^q$  parameter choices for RT and RM mixing. All choices except that for  $d_k^v$  in the RT case are insensitive.

analysis detects a missing incoming characteristic from the single fluid side. We supply this missing condition by coupling the model at the mixing zone edges to the buoyancy drag equation [9],

$$\ddot{Z}_k = (-1)^k Ag - (-1)^k C_k \frac{\rho_{k'}}{\rho_1 + \rho_2} \frac{V_k^2}{Z_k}. \quad (1.28)$$

Here  $C_k$  is a drag coefficient. This analysis is not needed for the present paper, in which we are analyzing closure terms relative to simulation data, but it is needed as part of a direct solution of the model equations, as has been discussed by Glimm et al. [16].

We see that the simple choice (1.27) for  $d_k^v$  depends on the buoyancy-drag equations for the mixing zone edge position  $Z_k$ . This equation has a free drag parameter which can be set by appeal to a bubble merger model [8], and to a model to set the ratio of bubble to spike growth rates [7]. This range of issues have also been discussed for compressible mixing [22]. In fact, our study of highly compressible RT mixing [12] shows that the self similar scaling law for RT mixing (and thus the buoyancy drag equation, which allows a self similar solution) remain valid in the deeply compressible region. To achieve this



result it is necessary to use time dependent Atwood numbers, reflecting the differing densities in a stratified highly compressible atmosphere. We consistently predict a strong increase in the mixing rate  $\alpha$  with compressibility in this sense.

The Saurel et al. expressions,

$$d_k^{Sv} = \mathcal{Z}_k / \mathcal{Z}_{k'} \quad d_k^{Sp} = \mathcal{Z}_{k'} / \mathcal{Z}_k , \quad (1.29)$$

are derived from solutions of approximate (linearized) Riemann problems modeling multiphase flows at the sub-grid level; their closure does not satisfy (1.26). The Saurel et al. model supplies the missing internal boundary conditions at the edges of the mixing zone by imposition of equal pressures [34]  $p_1(z = Z_k) = p_2(z = Z_k)$ .

We have two interpretations of the Saurel et al. model. In the first, which we denote as Saurel-1,  $A_I$  is regarded as a fitting parameter. The second interpretation of their model is to take advantage of the fact that  $A_I$  is a computed quantity in our data, and to use this time dependent value in the definition of the model. We denote this model as Saurel-2.  $A_I$  is plotted as a function of time in Fig. 1.3, to complete the definition of the Saurel-2 closure. We note that  $A_I$  has the dimensions of an inverse length and takes on large values at early time as the mixing layer tends to its (small) initial amplitude.

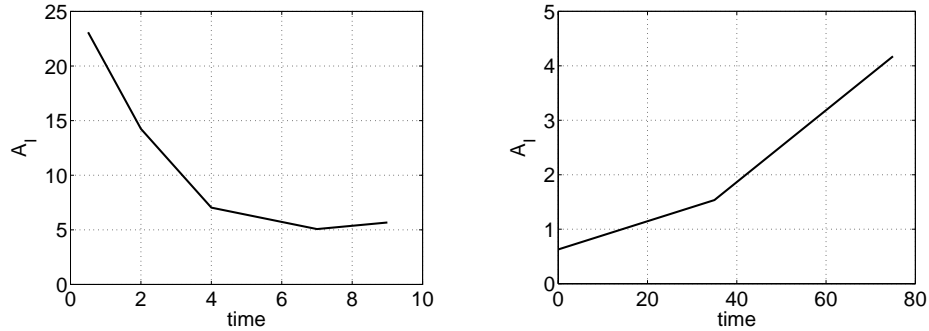


Figure 1.3: The interfacial area  $A_I$  per unit volume plotted vs. time. This plot serves to define the parameter  $A_I$  for the closure Saurel-2. Left: RT, Right: RM.

### 1.2.3 Validation and Comparison of Closures

The equations of this compressible, multi-species, multi-phase flow model, which account for surface tension and transport, were validated against multiple DNS data sets. For 3D RT mixing, two classes of simulations were used: an ideal simulation of multi-mode 3D RT mixing with no surface tension, no mass diffusion, no viscosity (except for numerical viscosity) and no thermal conductivity, and a simulation similar to the ideal one except for added surface tension, in the form of dimensionless values that spanned the experimental range of dimensionless surface tensions found for the immiscible fluids (with no surfactants) in the experiments of Reed [32] and Smeeton-Youngs [36]. For 2D RM mixing, the data sets obtained in our previous work on uncertainty quantification [39] were used. Another simulation modeled the Banershee-Andrews air-helium experiments with physical values of mass diffusion dimensionalized using an initial wave length scale inferred from observation [3].

In [3] we compare our closure, the two Saurel et al. closures and the RT or RM DNS simulation data. In comparison to simulation data, we use the definition

$$\text{relative error} = \frac{1}{3} \sum_{v^*, p^*, (pv)^*} \frac{\int \int |\text{DNS} - \text{model}| dz dt}{\int \int |\text{DNS}| dz dt} \quad (1.30)$$

for the sum of the relative model errors for  $v^*$ ,  $p^*$  and  $(pv)^*$ . The integration extends over the mixing zone. In the RT case, we exclude early time, before the bubbles have had much of a chance to interact, and to which the model is not supposed to apply, and integrate (*i.e.*, sum) over times from 4 to 10.

Our first main conclusion is the excellent (about 10%) agreement of our closures with the simulation data.

Our second main conclusion is the comparison of our closure to Saurel et al. We have previously introduced two distinct interpretations of the Saurel et al. model. In Fig. 1.4, we show the dependence of the total relative error on the value assumed for the area  $A_I$ . The error is minimized for  $A_I = 0$  for both the RT data and the RM data, defining two different Saurel-1 closures for these two data sets. With that choice, we compare the total relative errors in our model and the two Saurel models, see Table 1.2. In summary, our model has errors about one quarter to one half the size of those for the Saurel et al model. This conclusion addresses the validation of the closure models by computation of the residuals for the closure terms within the validated direct numerical simulations.

Our third main conclusion is the high degree of insensitivity of the  $q^*$  to

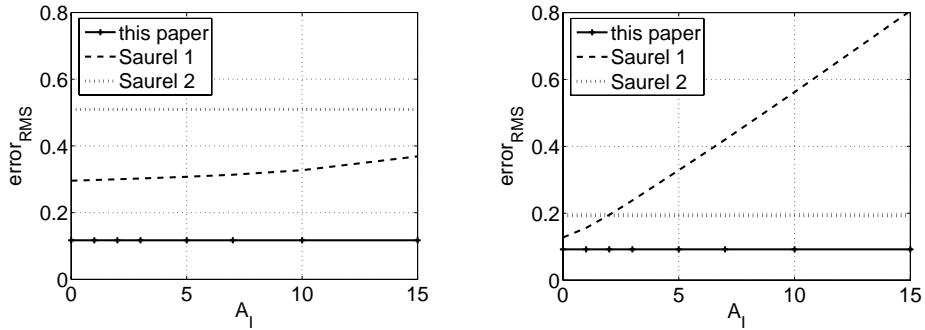


Figure 1.4: Comparison of the model error (1.30) for three closures. Of these, only Saurel-1 depends on the value of  $A_I$  as a fitting parameter; these plots serve to locate the best fit value of  $A_I$  ( $A_I = 0$ ) and thus to define the Saurel-1 closure. Left: RT, Right: RM.

Closure	$v^*$	$p^*$	$(pv)^*$	Average
Comparison to RT data				
This paper	18%	00%	18%	12%
Saurel-1	43%	02%	42%	30%
Saurel-2	56%	46%	51%	51%
Comparison to RM data				
This paper	07%	00%	20%	09%
Saurel-1	13%	04%	22%	13%
Saurel-2	12%	15%	31%	19%

Table 1.2: Model errors based on comparison to simulation data.

the defining quantities  $\mu_k^q$ , for many cases. We consider the condition

$$|\Delta q| \equiv |q_1 - q_2| \ll |\bar{q}| \equiv |\beta_1 q_1 + \beta_2 q_2| \quad q = v, p. \quad (1.31)$$

When (1.31) holds,  $q^*$  is effectively independent of the convex coefficients  $\mu_k^q$  and thus of the value of  $q_k$ , as can be shown. This is the case for all RM data,  $q^* = v^*, p^*$ , and for  $p^*$  in the RT data. Moreover,  $(pv)^*$  is insensitive to  $d_k^{pv}$  whenever (1.31) holds for  $q = p$ , which occurs for both RT and RM data, and in this case

$$(pv)^* \approx p^* v^*. \quad (1.32)$$

For these cases, the agreement of the two models and their agreement with the simulation data is understandable, but not a stringent test of the models. The insensitivity allows a simple choice of  $d_k^q$ , in cases where (1.31) holds. The only case where (1.31) is invalid is the  $v^*$  case for the RT instability. For the RT instability,  $v_1$  and  $v_2$  have generally opposite signs (in the frame stationary with the fluid container), so that  $|\bar{v}|$  is small relative to  $|\Delta v|$ .

Our fourth main conclusion concerns the cases which violate (1.31), and thus for which the data is a stringent test of the models. This occurs for the  $v^*$  closure for the RT data. We find that our  $\mu_k^v$  and those of Saurel et al. are significantly different.

The summary results of Table 1.3 can be understood as follows. The sensitive case for (1.31) occurs for the RT  $v^*$  closure only. In this case, the computational frame is that of the average interface position. The light fluid moves away from the direction of  $g$  and the heavy fluid moves in the direction

	$v^*$	$p^*$	$(pv)^*$
RT: Closure sensitive to $d_k^q$ ((1.31) or (1.32) invalid)	yes	no	no
RT: Closure sensitive to $v^*$	–	–	yes
RT: Relaxation important	no	late time	late time
RM: Closure sensitive ((1.31) or (1.32) invalid)	no	no	no
RM: Relaxation important	no	early time	early time

Table 1.3: Summary properties related to the closures  $q^*$ . It is remarkable that the closures depend sensitively on their defining parameter  $d_k$  only in the case of the RT data for the  $v^*$  closure.

of  $g$ . Thus in most parts of the mixing zone,  $v_1$  and  $v_2$  has opposite signs, so that  $\bar{v}$  is nearly zero relative to  $\Delta v$ , or in other words,  $\Delta v$  is large. All other cases are insensitive, so that the closure in these cases is basically independent of the  $d_k^q$ . In (1.20), the  $\Delta v$  contribution to the relaxation terms is larger than the  $\Delta p$  contribution, and as  $\Delta v$  occurs in the  $p^*$  relaxation, the  $p^*$  relaxation terms are generally significant while the  $v^*$  relaxation terms (proportional to  $\Delta p$ ) are not.

When  $\Delta p$  is small, which is the case for all simulations considered here, including those with surface tension,  $(pv)^* \approx p^*v^*$  is approximately independent of  $d_k^{pv}$ , which is thus insensitive to  $d^{pv}$ . It is sensitive to  $v^*$ .

Our fifth main conclusion is the apparent insensitivity of the closures and averaged flow quantities to variation of (secondary) physics effects (ideal vs. surface tension vs. mass diffusion). These secondary mechanisms have a substantial influence on the growth rates of the mixing zone, i.e.  $\alpha$  and the  $Z_k(t)$ . But once the influence of the edge motions has been scaled out of the data, the secondary physics appears to play only a small role in the simulation data, at least at length scales accessible at present levels of mesh refinement.

### 1.3 The Front-Tracking Approach

All the fluid mixing simulations we have referred to previously use the front-tracking software package *FronTier*. The objective of a front-tracking hydrodynamic program is to provide a numerical method that can represent interfaces explicitly as lower-dimensional meshes moving through a volume-filling grid in addition to keeping track of the initial interface (the surface, or set of surfaces that separate distinct fluids) throughout the simulation. Thus, its main characteristic is to follow whatever initial interface is input by the user in a topologically correct manner. *FronTier* is a front-tracking program that achieves this geometrical criterion in sophisticated ways, with an ability to handle interface bifurcations and restore untangled interfaces at each time step [15]. In addition to front-tracking algorithms, *FronTier* uses high-order numerical schemes to solve the partial differential equations that describe the flow, including where discontinuities are present in the solution of these fluid equations (*i.e.*, on wave fronts). Typically, these discontinuities are boundaries between fluids or shock waves and the program then solves hyperbolic conservation laws with robust Godunov-type schemes.

In general, there are two approaches to front-tracking. One is *grid-free* tracking and the other is *grid-based* tracking (Fig. 1.5). In *grid-free* tracking, the tracked front is the triangulated interface propagating freely through a rectangular volume-filling mesh. In *grid-based* tracking, the front is reconstructed at each time step using the intersection points of the interface with all grid cell edges. Grid-based tracking is very robust but inaccurate because of numerical surface tension, a form of surface smoothing. On the other hand,

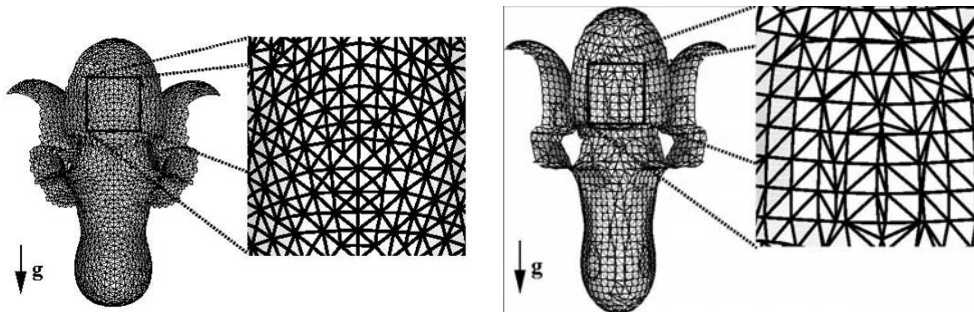


Figure 1.5: Interface reconstruction using grid-free tracking (left) and grid-based tracking (right). Note the bubble/spike formation typical in acceleration-driven mixing and the frequency of ill-conditioned triangles on the right figure. *Figure courtesy of Glimm et al. [15]*

grid-free tracking is more accurate but less robust in resolving interface bifurcations. *FronTier* takes a novel approach; instead of using either algorithm, it combines the two to preserve the advantages of each: robustness and accuracy. This hybrid solution is called *locally grid-based* tracking. The idea is simply to rely on the more accurate grid-free propagation unless there is a bifurcation. If a bifurcation occurs, the algorithm switches to a robust grid-based reconstruction inside a region around the bifurcation. The reconstructed interface inside this region is then joined to the grid-free interface outside using a construction resembling grid-based propagation [2].

Another important aspect of the *FronTier* code is its ability to support additional surface-based physics, namely surface tension and mass diffusion. These two phenomena are key in, respectively, the study of immiscible and miscible simulations. Surface tension forces a pressure jump at the interface that is proportional to the surface curvature. Thus, when solving for the mid



state pressure across the front at each dynamic time step - that is, solving a Riemman problem to connect two states on each side of the front - it suffices to modify the equation of pressure equilibration according to the pressure jump to account for the presence of surface tension. To account for physical mass diffusion, numerical mass diffusion has to be eliminated while a limited amount of mass diffusion is added back into the calculation on the basis of prescribed values for the physical mass diffusion constant. The elimination step is done very effectively by *FronTier*. [15]

## Chapter 2

# Uncertainty Quantification for a Chaotic Richtmyer-Meshkov Flow

In this section, we explain and summarize the previous work [39]. In order to quantify the uncertainty associated with a typical chaotic flow problem, namely the Richtmyer-Meshkov mixing of tin with lucite in a perturbed circular (2D) geometry, we propose stable statistics and convergence rates for the numerical solution and the solution error.

### 2.1 Introduction

When considering physical problems, uncertainty quantification (UQ) is commonly described as the study of the uncertainties, or errors, associated with a solution operator that maps input parameters into output parameters. These physical parameters are then modelled as probability distributions, and the uncertainty is thought to be inherent to the underspecification of the problem. In general, UQ seeks to understand the relative impact of input

uncertainty in the creation of errors within the output solution, and tries to predict or *quantify* the solution error given the magnitude of the input uncertainty.

For our problem of chaotic Richtmyer-Meshkov mixing, we view UQ as the problem of understanding and studying the solution errors that arise from the finite resolution discretizations in the numerical algorithms that are used to obtain solutions. Simplistically, our problem can then be viewed as the determination of *error bars* to be assigned to such algorithms.

Since many simulations, as used in practice, are under-resolved, asymptotic analysis of convergence fails for our purposes of studying solution errors. In addition, since Richtmyer-Meshkov mixing is a hyperbolically dominated flow with poor theoretical foundation, *a posteriori* methods, whose aim is to construct an upper-bound on the solution error, are generally inapplicable. As a result, we adopt a statistical point of view and examine ensembles of equivalent solutions of coarse and fine grid pairs, assuming that their differences represent the coarse grid solution errors.

This statistical approach to studying errors is simple and robust, but its direct application fails for the problem considered here. Chaotic flows, by definition, exhibit sensitive dependence on initial conditions. Generally they exhibit dependence not only on the physical parameters which define the flow, but also on the numerical parameters which define the solution algorithm.

Glimm et al. formulated in [27] a composition law for the errors in the numerical solution of 1D problems with composite shock interactions. Their approach consisted of linearly combining the error models of simpler elemen-

tary wave interactions to formulate a generalized error model for a problem with complex interactions. They showed that a simple and linear solution error model would suffice to study a highly non-linear problem.

However, once the shock physics problem is extended to Richtmyer-Meshkov mixing in a circular (2D) perturbed geometry - a problem that gives rise to a highly chaotic flow - a fundamental difficulty arises with the observed point-wise divergence of the physical quantities, such as the shock position, the single-phase densities and the volume fraction.

To resolve this, we frame the problem in terms of convergence rates and thus seek to find suitable averaging procedures that show a meaningful convergence of the flow quantities. With this use of statistical averages, we effectively produce a workable UQ theory for chaotic flows.

In assessing convergence properties and convergence orders, we combine the effects of the mean error,  $M$ , and the standard deviation of the error,  $STD$ . Following conventional ideas, we use the metric  $|M| + 2STD$  to determine convergence orders for all quantities. It is well known that the  $L_\infty$  norms of the position errors do not converge in shock discontinuities [39]. Therefore, we consider convergence in the  $L_1$  norm only.

In order to investigate the convergence properties of these averaged quantities, we use four different sizes of grid meshes in our simulations,  $100 \times 200$ ,  $200 \times 400$ ,  $400 \times 800$  and  $800 \times 1600$ . Assuming that the finest grid level solution corresponds to the exact solution, we can then record three levels of errors between successive grid sizes.

We call a quantity *reproducible* if it shows convergence under this mesh

refinement. After recognizing which quantities are reproducible, we seek to find suitable averaging procedures that effectively reduce meaningless statistical noise while remaining sufficiently rich to provide useful information about the flow.

## 2.2 Problem Formulation

The simulation setup can be seen in Fig. 1.2. The computational domain is  $x, y \in [0.25, 0.25] \times [-25, 25]$ , in units of cm. Time units are in microseconds and pressure units are in megabars. With  $r$  denoting radial distance, there is a constant-pressure boundary located at  $r = 24$  and an initial perturbed contact interface (already highly perturbed in the figure) located at  $r = 12.5$ . This is the material boundary between tin (outside the contact, with  $\rho_{tin} = 7.3$  at  $t = 0$ ) and lucite (inside the contact, with  $\rho_{lucite} = 1.2$  at  $t = 0$ ). Both tin and lucite are represented by a stiffened gamma law gas with parameters given approximately by  $\gamma = 3.72$  and  $p_{inf} = 0.15$  for tin, and  $\gamma = 1.85$  and  $p_{inf} = 0.03$  for lucite. These, in turn, define the stiffened gamma law pressure  $p + \gamma p_{inf} = (\gamma - 1)\rho e$ . The initial ambient pressure is  $p = 10^{-6}$  and the imposed pressure at the boundary is  $p = 0.687$ . The pressure discontinuity is imposed to give rise to an inward propagating Mach 2 shock at  $t = 0$ , resulting in Richtmyer-Meshkov mixing.

In the time-frame of the simulation ( $t$  goes to  $80 \mu s$ ), the in-going shock wave passes through the contact interface (at  $t \approx 20 \mu s$ ), hits the origin (at  $t \approx 40 \mu s$ ) and produces a reflected shock wave. This outgoing shock wave then re-shocks the highly perturbed interface ( $t \approx 45 \mu s$ ) and eventually reaches the

outer boundary.

Both the in-going and reflected waves give rise to highly chaotic flow. Fig. 2.1 shows the trajectories of the primary waves (in-going and outgoing shocks, mixing zone edges) detected by the wave filter algorithm described in [39], as well as the mean density contour plots.

The initial configuration of the contact interface perturbed by sine waves is given as follows:

$$r(\theta) = r_0 \left( 1 + \sum_n a_n \sin(n\theta) \right) \quad (2.1)$$

where  $\theta \in [-\pi/2, \pi/2]$ , and  $r_0 = 12.5$ . The sum over  $n$  ranges from  $n_{min} = 8$  to  $n_{max} = 16$ , so that the average number of observed modes in the initial perturbation is 12. The coefficients  $a_n$  are chosen as Gaussian random variables, with  $M = 0$  and  $STD = 0.2$ . The observed mean peak to peak amplitude, determined by this  $STD$ , is 0.25. The ensemble of initial conditions used in this study are due to successive calls to the C random number generator `erand48()` used to initiate the coefficients.

Finally, the position of the initial contact interface is either offset or not offset from the origin, with the center of the inner circle located at  $x = 0$ ,  $y = 5$  in the case of an offset.

### 2.3 Homogeneous Region Error Analysis

We use two types of averaging to obtain reproducible quantities. One is over sectors of the computational domain (spatial averaging) and the other

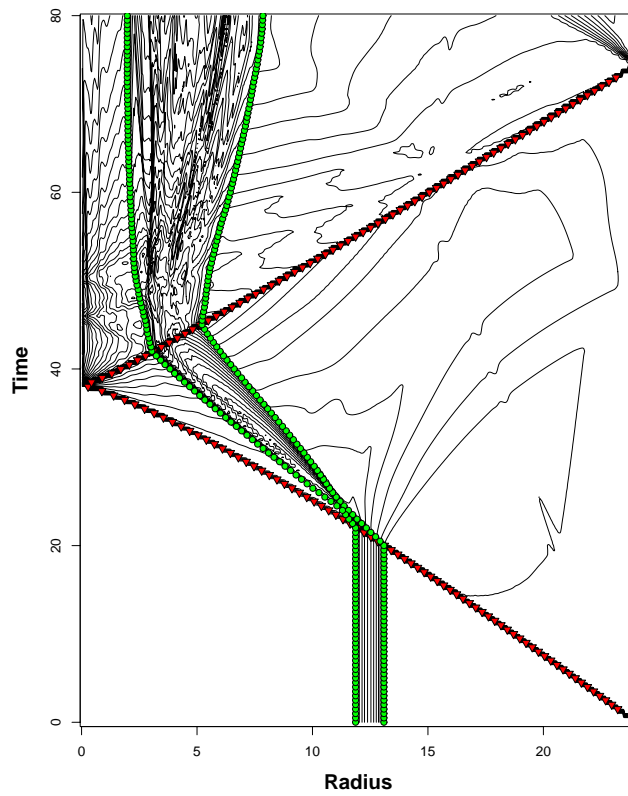


Figure 2.1: Primary waves and mean density contour plots averaged over a 45 degree circular arc at the equator of the flow region. The grid is  $800 \times 1600$  and the initial contact is offset relative to the origin. Mixing zone edges are shown in green; the shock position is shown in red.

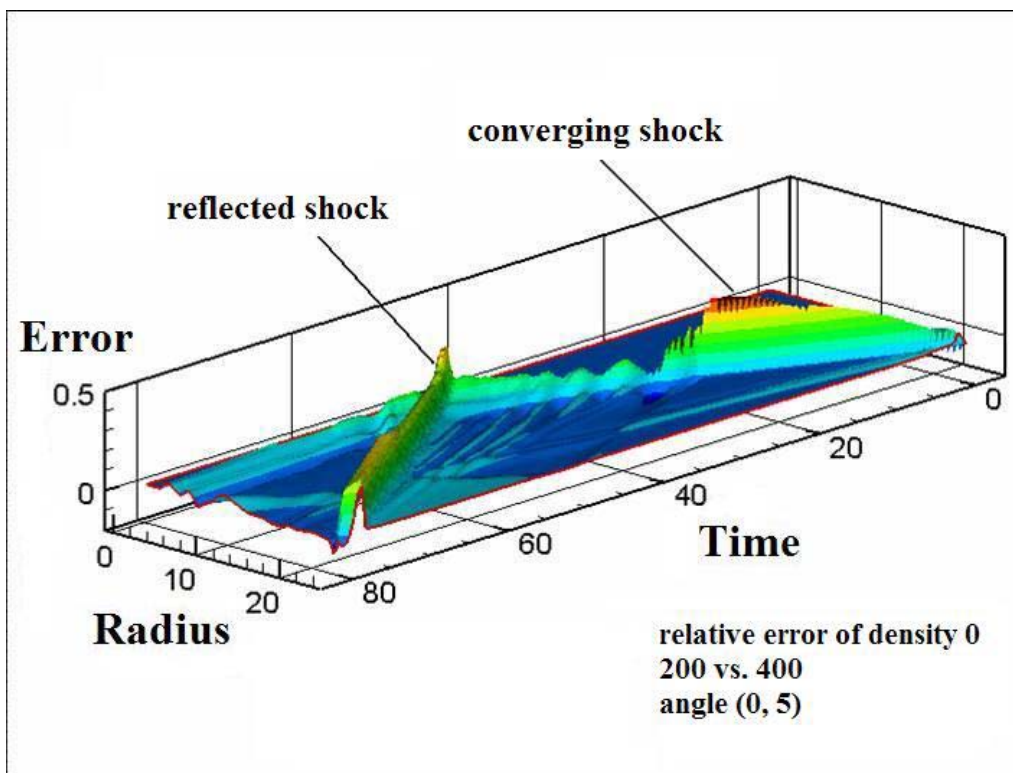


Figure 2.2: 3D contour of the relative mean heavy density error averaged over a 5 degree arc located at the equator of the flow region. The grid level is 200 and the circular contact discontinuity is not offset relative to the origin.



is over an ensemble of equivalent simulations. Sometimes a combination is necessary to obtain suitable statistics and observe convergence. For spacial averaging, we use a radial averaging tool that calculates the mean and variance of a given quantity in radial sectors of the computational domain. Another important tool that we use is the 2D wave filter, an automated pattern recognition algorithm which locates shock waves, rarefaction waves, and contact discontinuities in numerical solutions of Euler equations for compressible fluids. Both these tools are discussed extensively in [39]. The wave filter localizes the in-going and out-going shocks as well as the mixed phase zones (see Fig. 2.1). It also helps in recognizing distinct homogeneous space-time regions of the flow with a more or less common history: the singly-shocked region, the doubly-shocked region and the mixed phase zone. All these regions can be seen in the 3D contour of the relative mean heavy density error (with respect to the two coarsest grids) shown in Fig. 2.2. The wave filter is crucial once we recognize that the statistics of each homogeneous region are more adequately studied independently of each other.

The point values of each fluid type (heavy and light) are not convergent in the mixing zone because of the lack of interface convergence. The interface length is non-convergent in this type of chaotic problem as the interface is, in a fractal sense, nearly a volume rather than a surface. We find that single-phase densities are reproducible (*i.e.*, convergent and independent of modification of the ensemble) in homogeneous regions only after a modest amount of spatial averaging over angular regions (*e.g.*, 5 degree arcs).

One main conclusion regarding the spatial convergence of light and heavy

densities is that convergence is obtained after angular averaging, excluding regions within shock waves and at times of wave reflection at the origin. In this sense, these densities converge in  $r, t$ . Also, the light fluid errors are generally larger in absolute units (g/cc) than the heavy fluid errors. For more detail on the homogeneous region error analysis, refer to this same section in [39].

Most of the error statistics are spatially homogeneous (*i.e.*, translation invariant) within observed accuracy, but for regions enclosing the origin we find that the light fluid density error statistics have a non-uniform behavior at the origin at the time when the shock arrives at the origin ( $t \approx 40$ ). We found that this divergence could be fit to a power law in the form  $cr^{-0.25}$ .

## 2.4 Position Errors of Mixing Zone Edges

The mixing zone edges, with its associated position errors, are defined as the approximate extrema in the mixing zone, within each angular sector. For the purposes of locating the inner and outer edges of the mixing zone, we utilize the wave filter and follow previously accepted ideas (notably in the analysis of Rayleigh-Taylor mixing) to look for the 5% and 95% volume fraction contours within each 45 degree circular arc.

The location of these contours is, at times, quite a noisy diagnostic for the edges of the mixing zone. In Chap. 4 we show figures in which the mixing zone edges occasionally move abruptly as a function of time, even after a fair amount of averaging (both spatial and over ensembles of equivalent simulations). The complex structures of the error curves in time can be attributed

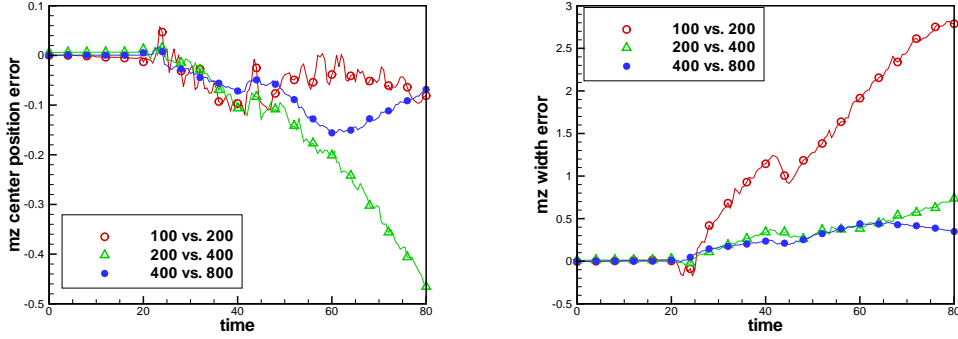


Figure 2.3: Mesh convergence of the mixing zone edges position errors, in units of length (cm). The mixing zone is defined relative to the  $45^\circ$  window at the equator, and averaged over an ensemble of  $N = 5$  realizations. Non-offset case. Left: Mixing zone center line. Right: Mixing zone width.

to the interaction of waves with the mixing zone. The interface is shocked at  $t \approx 20$  and then reshocked at  $t \approx 45$ . We give the statistics of convergence averaged over time using an ensemble of  $N = 5$  realizations in Fig. 2.3.

We use two measures to study the mixing zone position. The first is the center position, or mid-point of the mixing zone, computed as the average of the two edge positions (*i.e.*,  $(\max - \min)/2$ ). The second is the width of the mixing zone, computed as the difference in absolute terms of the two mixing zone edges (*i.e.*,  $\max - \min$ ). The errors in both of these measures are presented in Fig. 2.3.

With regards to the position errors of the mixing zone, we conclude that a fair amount of averaging is needed and that, contrary to the single phase densities, spatial averaging alone does not suffice to show convergence. The ensemble size of 5 is found to be the minimum value which shows a slow

Grid	$\Delta x$	Centerline Error						Width Error					
		Singly Shocked			Doubly Shocked			Singly Shocked			Doubly Shocked		
		M	STD	O	M	STD	O	M	STD	O	M	STD	O
100	1/4	-0.02	0.07	-	-0.05	0.11	-	0.26	0.43	-	1.92	0.94	-
200	1/8	-0.01	0.06	0.2	-0.23	0.16	-1.0	0.08	0.17	1.5	0.45	0.72	1.0
400	1/16	-0.01	0.02	1.1	-0.10	0.19	0.2	0.07	0.09	0.8	0.35	0.35	0.9
800*	1/32	-0.01	0.01	0.9	-0.07	0.04	1.8	0.01	0.03	2.0	0.34	0.26	0.3

Table 2.1: Convergence statistics for the errors in the mixing zone edges, averaged over time values and over an ensemble of size  $N = 5$  (\*  $N = 1$ ), in units of cm. Edge position defined relative to an angular window  $\theta \in [-45^\circ, 0^\circ]$ . Non-offset case.

convergence in both measures used, namely the centerline and the width. In general, the centerline of the mixing zone is less convergent than the width, and for the doubly-shocked region it requires a highly refined mesh for convergence. Analogous data from the other quarters (north pole, south pole and the other equator region) show similar statistics as those seen in Table 2.1. Finally, the errors are clearly non-monotone as a function of the mesh spacing, indicating that for these quantities the mesh refinement is not within a region of asymptotic convergence.

## 2.5 Conclusions

An important conclusion of this work is that only a modest amount of averaging can lead to reproducible quantities, with the notable exception of the volume fraction (not discussed here), a highly noisy quantity. For most quantities, averaging over a 45 degree arc (sometimes 40 in the offset cases) was sufficient in showing convergence within 10% of the fine grid solution value, or between  $\Delta x$  and  $2\Delta x$  for position errors, when using the  $|M| + 2STD$  metric.

1st Order or Near 1st Order	Marginal or $\approx 1/2$ Order	Non Convergent
$\rho_h(r, t, \xi)$	$\rho_h(r, t, \xi)$ doubly shocked and mixed phase regions	$\rho_h(r, t, \xi)$ mixed phase region
$\rho_h(r, t)$ singly and doubly shocked regions	$\rho_h(r, t)$ mixed phase region	
$\rho_l(r, t, \xi)$ singly shocked and mixed phase regions	$\rho_l(r, t, \xi)$ mixed phase and doubly shocked regions	
$\rho_l(r, t)$ singly shocked	$\rho_l(r, t)$ doubly shocked and mixed phase regions	
	$\beta(r, t, \xi), \beta(r, t)$	$\beta(r, t, \xi)$ doubly shocked region
$s(t, \xi), s(t)$		
$mz(t, \xi), mz(t)$ width		
	$mz(t, \xi), mz(t)$ centerline	

Table 2.2: Summary of convergence properties and orders, for the heavy and light densities  $\rho_h$  and  $\rho_l$ , volume fraction  $\beta$ , shock position  $s$  and mixing zone edges  $mz$ . All quantities are averaged over an angular variable, and also over all variables not explicitly present in the table. The variable  $\xi$  is an ensemble realization variable. The same quantities located in distinct columns indicate possible qualitatively different convergence behavior for distinct realizations, or for different angular regions, or as a distinction between offset and non-offset behavior.

Nevertheless, convergence is slow, often  $1/2$  order or less, and depends on the flow history. Also, convergence is not asymptotic in  $\Delta x$ , or even monotone.  $\beta(r, t, \varepsilon)$ , the volume fraction in the doubly shocked region, is an example of a quantity that is divergent in this metric (without averaging over an ensemble of equivalent simulations). The arc lengths of  $40^\circ$  and

For a complete picture of the convergence rates and statistics we found for all these quantities, see Table 2.2 and [39].

## Chapter 3

# Grid-Based Geometrical Computations for Conservative Data Collection

### 3.1 Introduction

The validation of the closures in the compressible flow models discussed in [3] was performed through the analysis of averaged quantities obtained from the DNS simulation data of 3D large-scale Rayleigh-Taylor simulations. This data was in turn collected and processed in a conservative manner. What this means is that at each data collection time step a tracked interface was reconstructed as a grid-based interface for the sole purposes of data collection. For each grid cell traversed by the interface (*i.e.*, mixed cell), we then computed the volumes for each phase and the surface area of the interface separating these phases. Normalizing the volumes, we devised an algorithm that uses these fractional volumes in mixed cells to compute the phase cell averages for state variables associated with each phase. In particular, these phase cell averages are determined from the in-phase densities, or micro-densities, for mass,

momentum, and energy, multiplied by the fractional volume fractions to obtain total phase mass, momentum, and energy. Other variables were constructed similarly as spatial volume-weighted averages. Here we present in detail the ideas behind the geometrical formulation for the simplified reconstructed interface and the computation of volume fractions and surface areas in mixed cells [24]. Our geometrical computations are based on the grid crossings of the interface with the cell edges and the 2-coloring of the cell corners, where each color is associated with a distinct phase.

Consider a 3D grid cell divided into two sub-domains. We compute the volume fraction of each of these domains and the surface area of the interface which separates them. This problem, as so formulated, is arbitrarily complex, but we assume a simple form of the two volumes and the surface area. This simple form is based on an interface reconstruction, which is determined by the crossings of the interface with the grid cell edges and the 2-coloring of the corners, where each color represents one of the two domain components. We derive from geometrical principles the fourteen non-trivial cases that, based on our assumptions, give topologically distinct configurations for edge crossings. For each distinct case, we reconstruct the contact interface and discuss our procedure for computing volumes and surface areas. The construction is not unique; all possible constructions are obtained.

Finally, we document for the volume fraction and surface area formulas implemented in the hydrodynamic front tracking code *FronTier* .

Given a 3D grid cell divided by an interface, our aim is to determine:

1. The volume fractions of the two domains separated by the interface,

respectively denoted by  $\beta_1$  and  $\beta_2$ . Since  $\beta_1 + \beta_2 = 1$ , we only compute the volume fraction  $\beta_1$ .

2. The surface area  $A$  of the contact interface.

We now state our objective and our assumptions for framing this problem geometrically.

### 3.1.1 Objective

Our objective is to implement an accurate statistical routine for the collection of flow quantities in the *FronTier* package based on the volume and surface area formulas developed here. Conservative data collection using these formulas will aid in the data analysis for simulations of turbulent fluid mixing [3]. For the purpose of computing  $\beta_1$  and  $A$  we reconstruct a simplified interface [15] within each cell, following the major steps given below:

1. Compute the crossings of the interface with the cell edges.
2. Determine component values at the cell corners and eliminate inconsistent crossings.
3. Reconstruct a new interface using consistent crossings.

To determine component values at the cell corners and identify inconsistent crossings for step 2, the algorithm relies on the crossings computed in step 1. At the end of step 2, topological inconsistencies due to interface self intersections have been removed and multiple interface crossings (more than



one per edge) have been eliminated. We begin with an analysis of step 3, thus assuming that the interface has already been untangled.

The volumes and surface areas are based on a reconstructed interface that is determined by the set of crossing points and the domain components of the cell corners. It does not coincide with the original interface.

### 3.1.2 Assumptions

A 2-color scheme distinguishes the components of the cell corners. The corner 2-coloring is then used to locate edges which have crossings with the interface, namely those linking corners with different colors. Two objects, the *interface perimeter* and the *interface surface*, play a major part in the reconstruction step.

Consider a cell with  $n$  edge crossing points, each one belonging to a distinct edge.

**Definition 3.1** An *interface perimeter* is a non self-intersecting curve on the cell surface that is linear on each face, and that crosses the cell edges exactly at the  $n$  given edge crossing points.

**Definition 3.2** An *interface surface* is a non self-intersecting mesh of triangular surface elements that has as lattice points the  $n$  edge crossing points within the cell, with none of the triangular elements (including their interior boundaries) lying on the cell surface.

The boundary of an interface surface is an interface perimeter.

In Section 2 we derive the fourteen non-trivial topologically distinct corner 2-colorings described in [15] for 3D cells. These cases, the starting point of our study, are the complete isomorphism invariants relative to the group of all isometries (distance-preserving transformations) and color inversions of the 2-colorings of the cell corners. In Section 3 we construct all possible interface perimeters consistent with a given set of edge crossings, and derive the complete set of triangulations for connected perimeters that may be realized as boundaries of interface surfaces in the cell. In Section 4 we discuss the procedure for averaging over the non-unique choices of perimeters and surfaces. In Section 5 we discuss the implementation of the volume fraction and surface area formulas in the front tracking code *FronTier* .

## 3.2 Corner Two-Colorings

Here we derive the fourteen non-trivial isomorphism classes for corner 2-colorings in 3D cells.

**Proposition 3.1** *14 non-trivial, non-isomorphic cases give the complete list of topologically distinct configurations for edge crossings in 3D cells.*

**Proof** The isomorphism group  $G$  in question is generated by isometries of the cell and by color inversion. The proof is in two steps. First we enumerate 14 isomorphism classes of non-trivial corner 2-colorings. Then we determine the total number of non-equivalent and non-trivial corner 2-colorings according to Polyá's enumeration formula, following [15, 31, 38], to conclude that the enumerated list of 14 is complete.

Let  $C$  be the set of  $2^d$  possible corner 2-colorings within a cell, where  $d$  is the number of cell corners. For a 3D cell,  $d = 8$ , so there is a total of  $2^8 = 256$  possible corner 2-colorings. Two corner 2-colorings are *isomorphic* if there exists a  $g \in G$  that maps one corner 2-coloring onto the other. Then  $G$  induces a partition of  $C$  into isomorphism classes, the disjoint subsets of  $C$  which group together all 2-colorings that are isomorphic to one another.

We enumerate the following 14 isomorphism classes for corner 2-colorings according to the number of black corners in the cell (where the case with zero black corners is discarded as trivial):

1. One black corner.

Two black corners such that:

2. they are connected by an edge.
3. they share a common face but are not connected by an edge.
4. they do not share a common face.

Three black corners such that:

5. they share a common face (*i.e.*, they are pairwise connected by two edges).
6. two are connected by an edge and the other does not share a common face with that edge.
7. none of the three are connected by an edge.

Four black corners such that:

8. they share a common face.
9. they are pairwise connected by three edges and form a broken line whose successive increments define a right-handed coordinate system.
10. they are pairwise connected by three edges and form a broken line whose successive increments define a left-handed coordinate system.
11. they are pairwise connected by three edges but do not share a common face of the cube nor form a broken line.
12. three are pairwise connected by two edges and the other is not connected to either of those edges.
13. two pairs are each connected by an edge, but they do not share a common face.
14. none of the four are connected by an edge.

From their description, each of these classes is invariant under  $G$ .

In Fig. 3.1 we show the 14 non-isomorphic and non-trivial corner 2-colorings which follow the list of isomorphism classes given above. We also give  $f$ , the number of faces with opposite black corners and opposite white corners (*i.e.*, with four edge crossing points), in the 2-colorings for which  $f > 0$ . This number plays a crucial role in the construction of interface perimeters, the topic of the next section.

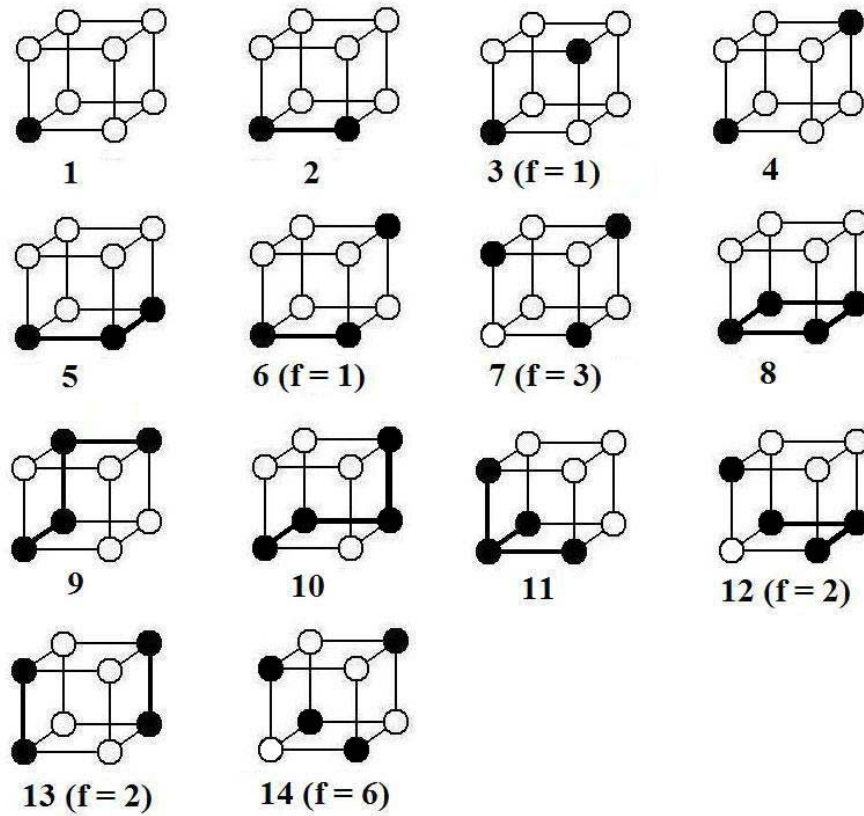


Figure 3.1: 14 topologically distinct, or non-isomorphic, corner 2-colorings in 3D cells. The numbering follows the enumeration of isomorphism classes. For later use we give  $f$ , the number of faces with opposite black corners, in the corner 2-colorings for which  $f > 0$ .

To complete the proof, we show by abstract methods that the number of isomorphism classes is 14, so that each case identified above must be a single isomorphism class, and the list of 14 is a complete list of isomorphism classes. We follow the derivation in [38] (Example 4, Section 9.4) that applies Polya's enumeration formula [31] to the non-equivalent corner 2-colorings of a cube.

First we show that a floating cube has 24 distinct *symmetries* involving revolutions about axes passing through the centers of opposite faces, the midpoints of diagonally opposite edges on opposite faces, and diagonally opposite corners on opposite faces. These symmetries are the complete set of isometries  $I$  that map a fixed cube onto itself. We have, for each of the three distinct pairs of opposite faces in the cube, either  $90^\circ$ ,  $180^\circ$ , or  $270^\circ$  revolutions that yield symmetries. With the trivial identity symmetry (the  $0^\circ$  revolution), that makes a total number of 10 symmetries. For the six distinct pairs of diagonally opposite edges on opposite faces, only the  $180^\circ$  revolution yields a symmetry. Thus, the total number of symmetries is increased to 16. Finally, for the four distinct pairs of diagonally opposite corners on opposite faces, the  $120^\circ$  and  $240^\circ$  revolutions yield symmetries. This brings the total number of symmetries to  $16 + 8 = 24$ .

Next we determine the *pattern inventory* for the corner 2-colorings of a floating cube. The pattern inventory, denoted by  $P_I(c_1, c_2, \dots, c_n)$ , is a generating function that gives the total number of colorings of an unoriented figure using different possible collection of colors  $c_1, c_2, \dots, c_n$ . As an instance, the pattern inventory for the 2-coloring of a cell face using a black and white color scheme is given by  $P_I(b, w) = 1b^4 + 1b^3w + 2b^2w^2 + 1bw^3 + 1w^4$ , where the

term  $1b^3w$ , for example, gives the number of non-equivalent colorings of the face with three black corners and one white corner. The pattern inventory is determined by summing the *cycle structure representations* of all the symmetries written in terms of the colors  $c_1, c_2, \dots, c_n$  and dividing this sum by the number of total symmetries. Thus, we first seek to find the cycle structure representation of the 24 symmetries we have identified. A symmetry is naturally characterized by a given permutation  $\pi_i$  of the eight corners of the cube. This permutation can be, in turn, represented as a product of disjoint cyclic permutations, or *cycles*. For example, the symmetry that involves a  $180^\circ$  revolution in the case of a cell face with cycling corners  $a, b, c, d$  is characterized by the permutation  $\pi = (ac)(bd)$  which permutes corners  $a$  and  $c$  to corners  $b$  and  $d$ . The cycle structure representation of this symmetry is then given by  $x_2x_2 = x_2^2$ , where  $x_2$  is the length of each 2-cycle. In general the cycle structure representation of a symmetry characterized by the permutation  $\pi_i$  is the product of the lengths  $x_i$  of the disjoint  $i$ -cycles that represent the permutation. Looking at the permutations of the corners resulting from the revolutions that yield symmetries in our case of a floating cube, we obtain the cycle structure representation for each of the 24 symmetries. The identity symmetry leaves all corners unchanged and, thus, has cycle structure representation  $x_1x_1x_1x_1x_1x_1x_1x_1 = x_1^8$ . For opposite faces, a  $90^\circ$  or a  $270^\circ$  revolution permutes all corners belonging to each opposite face so that the cycle structure representation of these symmetries is  $x_4x_4 = x_4^2$ . The  $180^\circ$  revolution permutes only opposite corners on each opposite face and so the cycle structure representation is  $x_2x_2x_2x_2 = x_2^4$ . Since there are three distinct pairs

of opposite faces in a cube, the total contribution of opposite-face revolutions is  $6x_4^2 + 3x_2^4$ . Now for diagonally opposite edges on opposite faces, the  $180^\circ$  revolution permutes pairs of distinct corners so that the cycle structure representation is  $x_2x_2x_2x_2 = x_2^4$ . Since there are six pairs of distinct opposite edges in a cube, the total contribution of opposite-edge revolutions is  $6x_2^4$ . Finally, for opposite corners the  $120^\circ$  and  $240^\circ$  revolutions leave both opposite corners fixed while cyclically permuting the three corners adjacent to them. The cycle structure representation for these symmetries is then  $x_1x_3x_3x_1 = x_1^2x_3^2$ , and the total contribution of opposite-corner revolutions is  $8x_2^4$  since there are four pairs of distinct opposite corners in a cube.

Collecting terms we obtain the generating function that gives the pattern inventory for the corner 2-colorings of a floating cube. Namely,

$$P_I(x_1, x_2, x_3, x_4) = \frac{1}{24} (x_1^8 + 6x_4^2 + 9x_2^4 + 8x_1^2x_3^2) . \quad (3.1)$$

For corner 2-colorings of the cube using a black and white scheme we use the algebraic identity  $x_i = (b^i + w^i)$  given in [38]. This then gives the pattern inventory

$$P_I(b, w) = \frac{1}{24} ((b + w)^8 + 6(b^4 + w^4)^2 + 9(b^2 + w^2)^4 + 8(b + w)^2(b^3 + w^3)^2) . \quad (3.2)$$

Expanding Eq. 3.2 we get



$$P_I(b, w) = (b^8 + b^7w + 3b^6w^2 + 3b^5w^3 + 7b^4w^4 + 3b^3w^5 + 3b^2w^6 + bw^7 + w^8) . \quad (3.3)$$

In Eq. 3.3 we drop terms that are redundant. Thus, corner 2-colorings with more than five black corners ( $b^i$  terms with  $i > 5$ ) are dropped since these can be mapped to colorings with less than five corners after a color interchange (white to black, black to white). In addition, the terms  $w^8$  and  $b^8$  are dropped since 3D cells cut by an interface have, by definition, at least two corners with different domain components (*i.e.*, different colors). This ultimately yields the number of non-trivial 2-colorings of a floating cube, namely

$$P_I(1, 1) = 1 + 3 + 3 + 7 = 14 . \quad (3.4)$$

From this result we conclude that the 14 corner 2-colorings shown in Fig. 3.1 constitute a complete list of non-trivial isomorphism classes for corner 2-colorings in 3D cells.  $\square$

### 3.3 Interface Perimeters

#### 3.3.1 Perimeter Construction

Here we construct all the possible perimeter curves that can be formed on the surface of the 3D cell, following Definition 3.1, for each isomorphism class of corner 2-colorings. Our approach is to start from a single cell face and then proceed to the union of the cell faces.

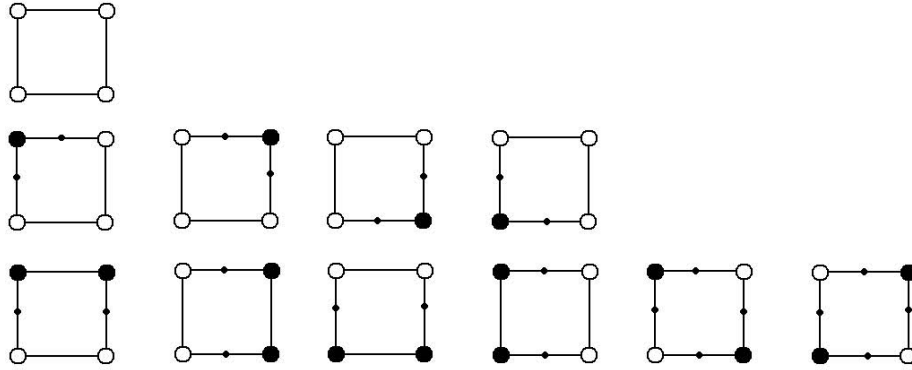


Figure 3.2: Non-isomorphic corner 2-colorings for single cell faces. From top to bottom row, the corner 2-colorings have zero, one, or two black corners. Edge crossings are shown as small black dots.

**Proposition 3.2** *There are either zero, two, or four edge crossings on any cell face.*

**Proof** A cell face is a square with four edges and four corners. A complete circuit around the square observes an even number of crossings, since the starting and ending colors are identical. In the case that all corners are of a single color, there are no crossings. Moreover, there is at most one crossing per edge, so the maximum number of crossings is 4. We show all possible cases in Fig. 3.2.  $\square$

**Proposition 3.3** *The interface perimeter on a given cell face is uniquely determined by the edge crossings for the cases of zero or two edge crossings. It is two-fold non-unique in the case of four edge crossings.*

**Proof** Faces with two edge crossings have a unique interface perimeter,



Figure 3.3: Interface perimeters on single cell faces. They are uniquely determined by the edge crossings for cell faces with two edge crossings (left) and they are two-fold non-unique for cell faces with four edge crossings (right). Edge crossings are shown as small black dots.

namely the linear segment connecting the crossings (see Fig. 3.3, left). For cell faces with four edge crossings, the interface perimeter is, by definition, the union of two linear segments connecting distinct pairs of edge crossings. Since these segments are not allowed to intersect, they must join crossings on adjacent edges. There are exactly two ways to do this (see Fig. 3.3, right).  $\square$

To construct interface perimeters on the union of the cell faces, we proceed by locating all edge crossings in each corner 2-coloring of Fig. 3.1 and then forming the perimeters on each face. Since the interface perimeter crosses the cell edges exactly at the edge crossing points, it is formed by selecting one of the possible perimeters for each single cell face. In general, the interface perimeter is not connected but is the union of multiple disjoint connected components.

**Proposition 3.4** *There are 92 distinct interface perimeters that can be formed from the fourteen non-isomorphic, non-trivial, configurations of edge crossings in 3D cells.*

**Proof** This is the extension in 3D of Proposition 3.3. Non-uniqueness on a single cell face results in non-uniqueness for the interface perimeter. According to Proposition 3.3, this only occurs in cases where a cell face has four edge crossings (*i.e.*, opposite black corners and opposite white corners). For a given corner 2-coloring, the number  $P$  of possible interface perimeters is given by  $P = 2^f$ , where  $f$  is the number of faces with four edge crossings. For  $f = 0$ ,  $P = 1$  in cases 1, 2, 4, 5, 8, 9, 10, and 11. The remaining corner 2-colorings have  $f = 1$  (cases 3 and 6),  $f = 2$  (cases 12 and 13),  $f = 3$  (case 7), and  $f = 6$  (case 14) faces with four edge crossings resulting in, respectively,  $P = 2^1 = 2$ ,  $P = 2^2 = 4$ ,  $P = 2^3 = 8$ , and  $P = 2^6 = 64$  possible distinct perimeter constructions. Summing these possibilities, we have  $8(2^0) + 2(2^1) + 2(2^2) + 2^3 + 2^6 = 92$  possible interface perimeters in 3D cells.  $\square$

In general, interface perimeters are disconnected and consist of several connected components. We present in Figs. 3.4, 3.5, and 3.6 the 92 interface perimeters, organized according to their number of connected components. Fig. 3.4 shows all the connected perimeters, while Figs. 3.5 and 3.6 show the disconnected ones. For the non-isomorphic case 14, with  $f = 6$ , there is a total of  $P = 2^6 = 64$  distinct interface perimeters, including the 48 disconnected perimeters shown in Fig. 3.6. By counting the distinct interface perimeters seen in all three figures, we have a total number of  $32 + 12 + 48 = 92$  possible perimeter constructions. From Proposition 3.4, we conclude that Figs. 3.4, 3.5, and 3.6 show all the distinct interface perimeters that can be formed on the surface of a 3D cell. A disconnected perimeter has at most four connected components; the “maximal case” occurs when there is an edge crossing on each





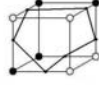
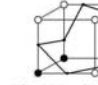

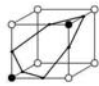


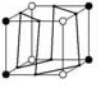


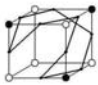



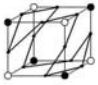






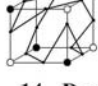





<b>f = 0</b>	 <b>1 - Corner</b>  <b>2 - Edge</b>  <b>5 - Glider</b>  <b>8 - Plane</b>  <b>9 - Twister-I</b>  <b>10 - Twister-II</b>  <b>11 - Hexagon</b>
<b>f = 1</b>	 <b>3 - Hexagonoid</b>  <b>6 - Twisteroid</b>
<b>f = 2</b>	 <b>12 - Octagonoid-I</b>  <b>13 - Octagonoid-II</b>
<b>f = 3</b>	 <b>7 - Enneagonoid</b>  
<b>f = 6</b>	 <b>14 - Duodecagonoid-I</b>                <b>14 - Duodecagonoid-II</b>

Figure 3.4: 32 distinct connected interface perimeters that can be formed on the surface of a 3D cell. We group the perimeters according to  $f$ , the number of faces with four edge crossings, and the isomorphism classes of perimeters in each non-isomorphic case. Note that we have labeled these perimeter classes and that, in most cases, labels follow the names of polyhedra given by the number of edge crossings on the perimeter. The numbering of the non-isomorphic cases follows the enumeration of isomorphism classes for corner 2-colorings.

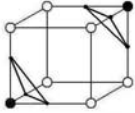
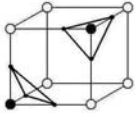
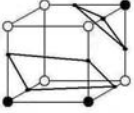
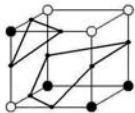
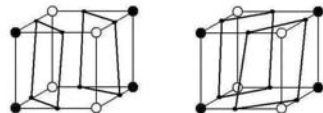


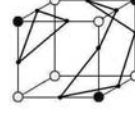
<b>f = 0</b>	 <b>4 - Two Corners</b>			
<b>f = 1</b>	 <b>3 - Two Corners</b>		 <b>6 - Edge + Corner</b>	
<b>f = 2</b>	 <b>12 - Glider + Corner</b>		 <b>13 - Two Edges</b>	
<b>f = 3</b>	 <b>7 - Three Corners</b>		 <b>7 - Hexagon + Corner</b>	
	 <b>7 - Hexagonoid + Corner</b>			

Figure 3.5: 12 distinct disconnected interface perimeters that can be formed on a 3D cell surface, for  $f = 0, 1, 2, 3$ . The numbering of the non-isomorphic cases follows the enumeration of isomorphism classes for corner 2-colorings.

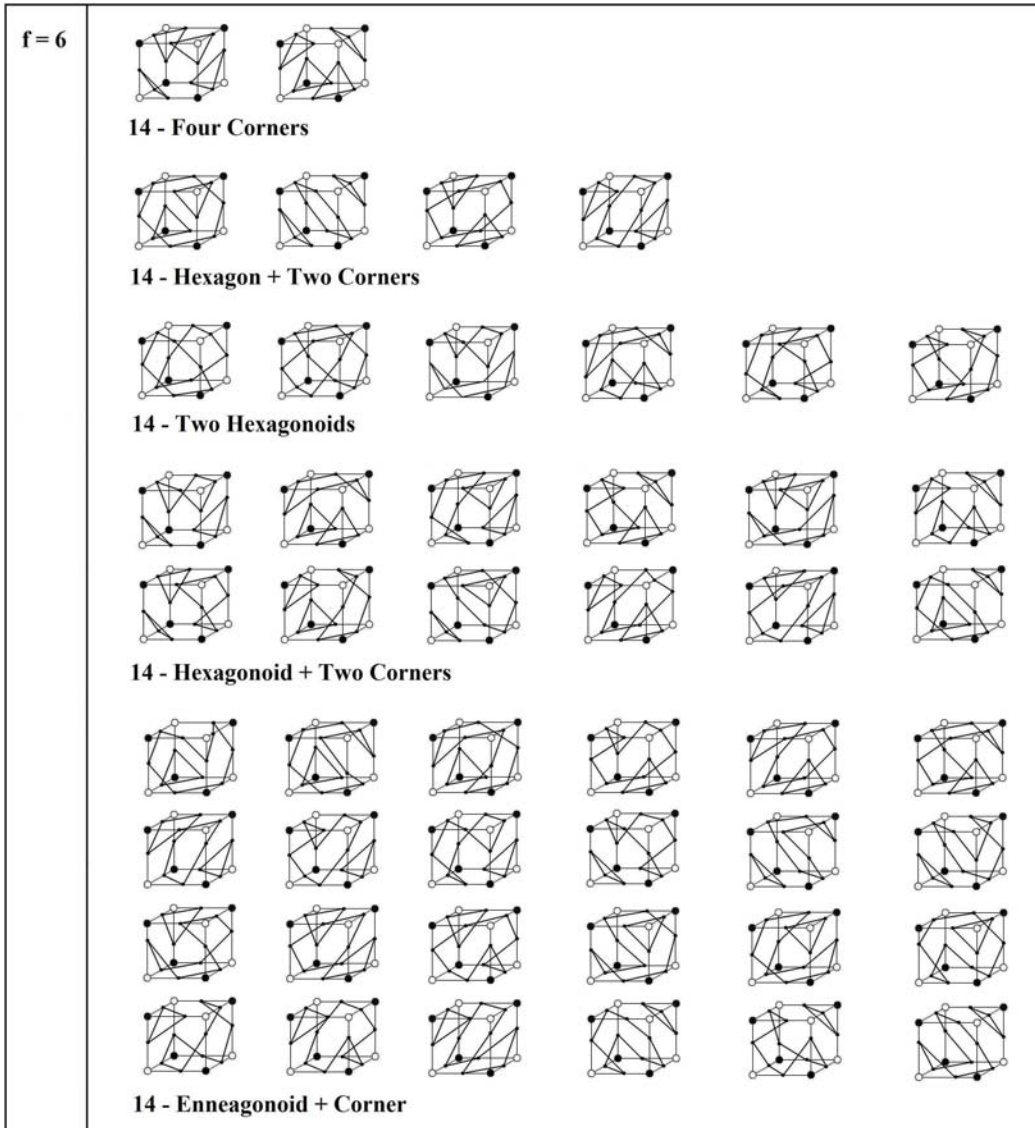


Figure 3.6: 48 distinct disconnected interface perimeters that can be formed on a 3D cell surface in the non-isomorphic case with  $f = 6$  (case 14).

cell edge. As before, we consider isomorphism classes for connected perimeters relative to the group of isometries and color inversion.

**Proposition 3.5** *The 32 connected perimeters displayed in Fig. 3.4 are grouped (by their common labels) into 14 isomorphism classes.*

**Proof** We show that each of the fourteen classes of connected perimeters depicted in Fig. 3.4 form an isomorphism class. For cases with  $f = 0, 1$ , the isomorphism classes of perimeters consist of exactly one element distinguished by an isomorphism class of the corner 2-colorings. In the two cases with  $f = 2$  (12 and 13), the isomorphism is a  $180^\circ$  rotation about the line passing through the midpoints of the front-left and back-right vertical edges (diagonally opposed in the cell), followed by a color inversion, for the octagonoid-I perimeter class, and the same “up-down” rotation about the opposite edges with black corners for the octagonoid-II perimeter class. For the enneagonoid perimeter class of case 7, with  $f = 3$ , the three symmetries are the  $0^\circ$ ,  $120^\circ$ , and  $240^\circ$  rotations about the line passing through the top-right front and the bottom-left back corners (diagonally opposed corners in the cell). For the duodecagonoid-I perimeter class of case 14 with  $f = 6$ , the four symmetries consist of  $0^\circ$  and  $180^\circ$  rotations about the line passing through the center points of the top and bottom cell faces, and of  $90^\circ$  and  $270^\circ$  rotations about the same axis followed by a color inversion. In the same case, the duodecagonoid-II perimeter class has twelve symmetries given by the same rotations as in the duodecagonoid-II and the enneagonoid perimeter classes, namely  $0^\circ$  and  $180^\circ$  rotations about the line passing through the center points of the top and bottom cell faces,



90° and 270° rotations about the same axis followed by a color inversion, and 0°, 120°, and 240° rotations about the line passing through the top-right front and the bottom-left back corners (diagonally opposed corners in the cell). For each rotation about the axis passing through the diagonally opposed corners, there are four symmetries generated by the rotations about the vertical axis passing through the top and bottom faces. This brings the total number of symmetries to  $4 \times 3 = 12$ . The two isomorphism classes of perimeters in case 14 have topologically distinct perimeters distinguished by an invariant cyclic ordering around the perimeter of the edges lying on opposite faces of the cell. We return to this topological invariant in the next section, where we discuss the triangulation of connected perimeters, and complete the proof.  $\square$

### 3.3.2 Valid Triangulations of Connected Perimeters

We now turn to valid triangulations of connected perimeters, as these determine the interface surface. We first recall some results on the triangulation of polygons and then define validity for triangulations of interface perimeters.

#### Preliminaries on the Triangulation of Polygons

We begin by recalling some elementary definitions [30].

**Definition 3.3** *A **graph isomorphism**  $f$  is a bijection, or one-to-one mapping, between the vertices of two graphs  $G$  and  $H$  ( $f : V(G) \rightarrow V(H)$ ) with the property that any two vertices  $u$  and  $v$  from  $G$  are adjacent if and only if  $f(u)$  and  $f(v)$  are adjacent in  $H$ . If there exists such a mapping between*

two graphs, then they are said to be isomorphic.

Connected perimeters are then clearly graph isomorphic to polygons.

**Definition 3.4** Any polygon  $P$  can be **triangulated** by connecting pairs of non-adjacent vertices with straight lines called diagonals, so that every vertex is the endpoint of at least one diagonal.

This leads to the following result.

**Theorem 3.1** If  $P$  is a polygon with  $n$  sides, then there is a total of  $n - 3$  diagonals which will decompose  $P$  into  $n - 2$  triangles.

**Proof** We use a straightforward induction proof taken from O'Rourke [30]. We start with  $n = 3$  (the trivial case of a triangle). For  $n \geq 4$ , we partition the polygon  $P$  into two sub-polygons  $P_1$  and  $P_2$  so that  $P_1 \cup P_2 = P$  and the diagonal  $d$  is adjacent to both  $P_1$  and  $P_2$ . These polygons have, respectively,  $n_1$  and  $n_2$  vertices. Clearly, we have a vertex count of  $n_1 + n_2 = n + 2$  since the endpoints of  $d$  are counted twice: first in the vertices of  $P_1$ , then in the vertices of  $P_2$ . Applying the induction hypothesis to both sub-polygons and using the identity  $n_1 + n_2 - 2 = n$ , we get a diagonal count for  $P$  of  $(n_1 - 3) + (n_2 - 3) + 1$ , where the  $+1$  represents the diagonal  $d$  and  $n_1 - 3$  and  $n_2 - 3$  represent, respectively, the diagonals of  $P_1$  and  $P_2$ . We thus have a total of  $(n_1 - 3) + (n_2 - 3) + 1 = (n_1 + n_2) - 5 = n + 2 - 5 = n - 3$  diagonals in  $P$  and  $(n_1 - 2) + (n_2 - 2) = n + 2 - 4 = n - 2$  triangles. This completes the proof.  $\square$

A natural question that arises from Theorem 3.1 is how to identify the

number of ways that an  $n$ -gon can be divided into  $n - 2$  triangles if different placements of the  $n - 3$  diagonals are counted separately. This is Euler's famous *polygon division problem*. It is well-known in combinatorics that the answer to this question is given by a sequence of natural numbers, denoted by  $\{C_n\}$ , called the *Catalan numbers*, named after the Belgian mathematician Eugène Charles Catalan.

**Theorem 3.2** *The answer to Euler's polygon division problem is the Catalan number  $C_{n-2}$ , where the  $n$ th term of the sequence  $\{C_n\}$  is given by*

$$C_n = \frac{1}{n+1} \binom{2n}{n} = \frac{(2n)!}{(n+1)!n!} . \quad (3.5)$$

**Proof** We do not prove this result, as it is beyond the scope of our discussion, but we refer the reader to an elegant and succinct geometrical proof by Lamé [25].  $\square$

The first few Catalan numbers are

$$\{C_n\} = \{1, 1, 2, 5, 14, 42, 132, \dots\} , \quad (3.6)$$

for  $n = 0, 1, 2, 3, \dots$

The formula in Eq. 3.5 is derived according to [20] using the recurrence relation

$$C_0 = 1, C_{n+1} = \sum_{i=0}^n C_i C_{n-i} , \quad (3.7)$$

for  $n \geq 0$ , that is satisfied by the sequence  $\{C_n\}$ . Then, defining a generating function of the form

$$c(x) = \sum_{n=0}^{\infty} C_n x^n, \quad (3.8)$$

and using Eq. 3.7 we have  $c(x) = 1 + xc(x)^2$  and, hence,  $c(x) = \frac{1 - \sqrt{1 - 4x}}{2x}$ .

Expanding the square root term as a power series using the identity

$$\sqrt{1 + y} = 1 - 2 \sum_{n=1}^{\infty} \binom{2n - 2}{n - 1} \left(\frac{-1}{4}\right)^n \frac{y^n}{n}, \quad (3.9)$$

and substituting the result for  $c(x)$  gives

$$c(x) = \sum_{n=0}^{\infty} \binom{2n}{n} \frac{x^n}{n + 1}. \quad (3.10)$$

Finally, equating coefficients yields Eq. 3.5.

From Eq. 3.7 we can immediately infer the number of distinct triangulations for any polygon, including those that are graph isomorphic to connected perimeters (the boundaries of interface surfaces in 3D cells).

We are now in a position to complete the proof of proposition 3.4. We seek to define a topological invariant that distinguishes perimeters in the duodecagonoid-I isomorphism class from elements in the duodecagonoid-II isomorphism class. In Fig. 3.7 we have labeled edge crossings belonging to a common face according to the orientation of that face in the three spacial

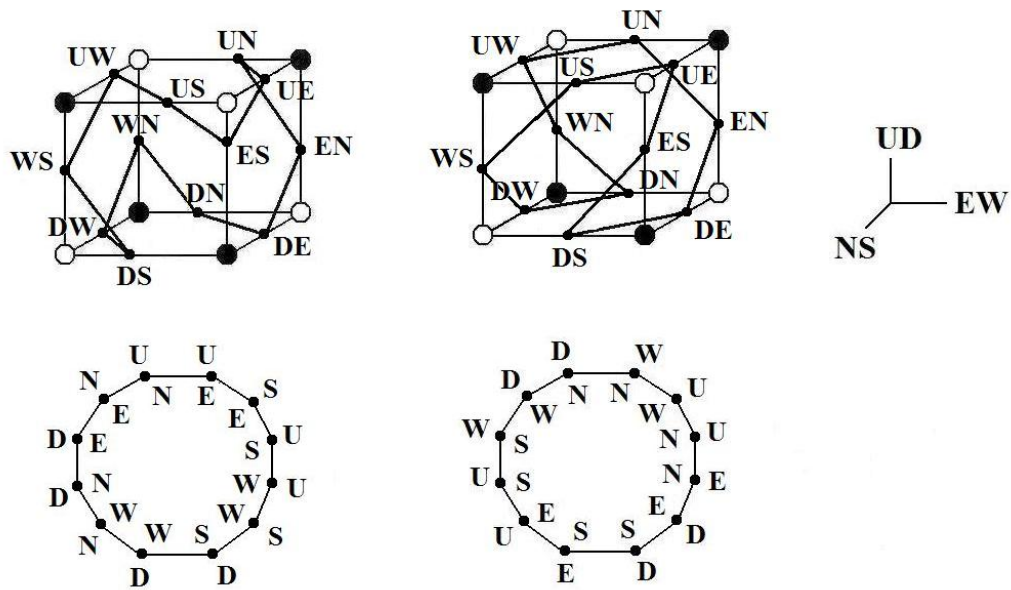


Figure 3.7: Examples of perimeters in the duodecagonoid-I (left) and duodecagonoid-II (right) isomorphism classes of connected perimeters of case 14, with  $f = 6$ .

directions (NS, EW, or UD). We see from the two duodecagons in Fig. 3.7 that the relative location of the edges belonging to the three sets of opposite faces in the cell (*e.g.*, N-S) around the perimeter constitutes a topological invariant. Furthermore, this invariant is distinct for the two perimeter classes. For elements in the duodecagonoid-I case, edges on opposite faces are also opposite in the polygon. So for edge crossings on opposite faces, denoted by  $f_1$  and  $f_2$ , where  $f_1 = U, E, N$  and  $f_2 = D, W, S$  (according to which face they belong to in the cell), the cyclic representation of their position around the duodecagon is given by  $\pi_I = (f_1, f_1, a, f_1, f_1, b, f_2, f_2, c, f_2, f_2, d)$ , where  $a, b, c, d$  denote other edge crossings. For elements in the duodecagonoid-II case, the corresponding cyclic representation is given by  $\pi_{II} = (f_1, f_1, a, f_2, f_2, b, f_1, f_1, c, f_2, f_2, d)$  for one of the three sets of edges on opposite faces, and by  $\pi_I$  for the other two sets of edges on opposite faces. The invariant for the duodecagonoid-I isomorphism class, which is distinguished by the cyclic representation  $\pi_I$ , has then four symmetries, while the invariant for the duodecagonoid-II isomorphism class, which is distinguished by the cyclic representation  $\pi_I$  for one set of edges on opposite faces and by the cyclic representation  $\pi_{II}$  for the other two sets of edges on opposite faces, then has  $3 \times 4 = 12$  symmetries. Elements in both isomorphic classes are shown in Fig. 3.4.

## Validity

Many of the connected perimeters that we have constructed previously cannot be realized as the boundary of a (valid) interface surface according to our assumptions. The restriction from Definition 3.2, that no diagonal from

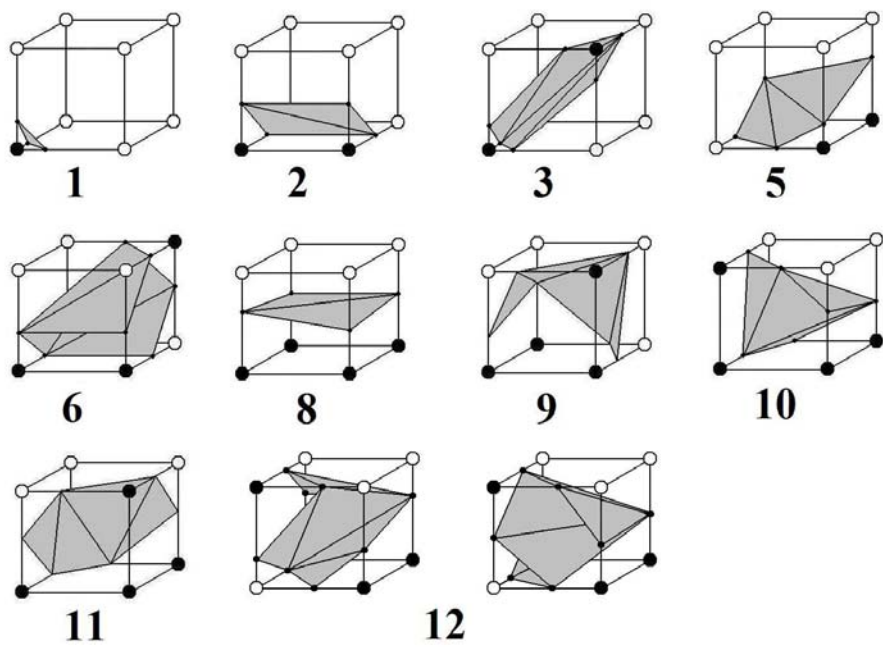


Figure 3.8: Examples of interface surfaces bounded by valid perimeters belonging to isomorphism classes of connected perimeters with  $T > 0$ . They are, from left to right, starting at the top, the corner (case 1), the edge (case 2), the hexagonoid (case 3), the glider (case 5), the twisteroid (case 6), the plane (case 8), the twister-I (case 9), the twister-II (case 10), the hexagon (case 11), and the octagonoid-I (case 12). Note that the perimeter class of case 12 has two distinct elements. All triangulations are picked arbitrarily.

a triangulation lie on the cell surface, is in fact a constraint for any case in which at least one cell face has four edge crossings (*i.e.*,  $f > 0$ ). For all cases with  $f = 0$ , a connected perimeter  $P$  with  $n$  edge crossings is, according to Theorem 3.2, the boundary of  $C_{n-2}$  distinct interface surfaces, each one determined by a distinct triangulation of the  $n$ -gon. As  $f$  increases, the number of prohibited diagonals increases, and in some cases no such triangulation is possible. Consider, for example, the connected perimeter shown in case 13 of Fig. 3.4, with  $f = 2$ . The octagonoid surface bounded by this perimeter cannot lie totally in the cell interior. This is an example of an *invalid* interface surface, according to Definition 3.2. The connected perimeter  $P$  with  $n$  edge crossings is called *valid* if there is at least one interface surface  $S$  having  $P$  as its boundary. The definition will be satisfied if there is a triangulation of the  $n$ -gon for which no diagonals lie on a face (such a triangulation is also called *valid*). General (disconnected) perimeters are valid if each of their connected components are valid.

Let  $T$  be the number of valid triangulations for the elements in a given isomorphism class of connected perimeters. Fig. 3.8 shows examples of interface surfaces bounded by valid connected perimeters belonging to perimeter classes with  $T > 0$ .

**Proposition 3.6** *The values of  $T$  in Fig. 3.9 are correct.*

**Proof** The proof of this proposition is exposed in Chap. 5.  $\square$






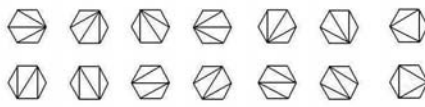

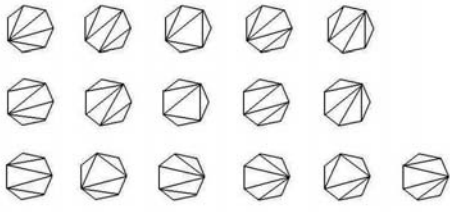
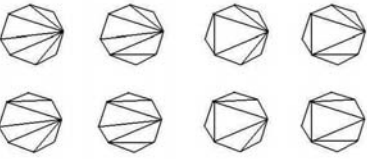
Perimeter Class	$f$	$n$	$C_{n-2}$	$T$	Valid Triangulations
Corner	0	3	1	1	
Edge / Plane	0	4	2	2	
Glider	0	5	5	5	
Hexagon / Twister-I / Twister-II	0	6	14	14	
Hexagonoid	1	6	14	4	
Twisteroid	1	7	42	16	
Octagonoid-I	2	8	132	8	
Octagonoid-II	2	8	132	0	
Enneagonoid	3	9	429	0	
Duodecagonoid-I	6	12	16796	0	
Duodecagonoid-II	6	12	16796	294	Not shown

Figure 3.9: Valid triangulations for elements in the isomorphism classes of connected perimeters. In the table, we give for each class  $f$ , the number of faces with four edge crossings on a common face;  $n$ , the number of edge crossings on the perimeter;  $C_{n-2}$ , the Catalan number; and  $T$ , the number of valid triangulations. Only triangulations for perimeter classes with  $f = 0$  were used in our implementation. In these cases, the identity  $T = C_{n-2}$  holds; otherwise,  $T < C_{n-2}$ .

### 3.4 Computational Procedure

Our computation of volumes and surface areas is based on the configuration of all interface surfaces that may be realized inside the cell. Thus, for connected perimeter classes with  $f > 0$  we only consider valid triangulations.

A reconstructed interface is determined first by the interface perimeter  $P$ , and then by the interface surface  $S$  it bounds according to a given triangulation of  $P = \partial S$ . For each non-isomorphic case, we wish to compute a volume fraction and a surface area that takes into account all the valid triangulations for all the perimeters that can be constructed in that case.

Our procedure is then an averaging over a set of geometrical possibilities. For cases with a unique interface perimeter (with  $f = 0$ ) this procedure only involves an averaging over the distinct interface surfaces and volumes given by the triangulations of the perimeter. For the remaining cases, an averaging over distinct interface perimeters is also required.

The surfaces bounded by elements in the hexagonoid, twisteroid, octagonoid-I, and duodecagonoid-I perimeter classes are not used in the construction of the areas and volumes. Geometrical constructions (not shown here) seem to show that the duodecagonoid surfaces are typically or always self-intersecting inside the 3D cell, effectively violating Definition 3.2. For this reason, and due to the complexity of these surfaces (which intuitively do not appear to be physically realistic), such terms have been omitted from the formulas for areas and volumes presented below. In the hexagonoid, twisteroid, and octagonoid-I cases, constructions seem to show that the self-intersection of surfaces does not occur. However, this topological property is not formally proved here. We

also omit these terms due to their complexity.

If the computational grid spacings in the  $x$ ,  $y$  and  $z$  directions are, respectively,  $\Delta x$ ,  $\Delta y$ , and  $\Delta z$ , then we divide the fractional cell volume by the unit cell volume  $V_0 = \Delta x \Delta y \Delta z$  to map  $V_1$ , the volume of domain 1 inside the grid cell, into a volume fraction  $\beta_1 = \frac{V_1}{V_0}$ , so that  $0 \leq \beta_1 \leq 1$ . We do not normalize  $A$ , as there is no convenient method to do so.

### 3.4.1 Volume Fractions

For any of the fourteen non-isomorphic cases there is either a unique interface perimeter or many distinct interface perimeters. Let  $P$  denote the number of interface perimeters that can be formed for a given case and that are implemented in *FrontTier* (*i.e.*, that exclude hexagonoid, twisteroid and octagonoid-I components). Moreover, any given interface perimeter consists of at most four connected components. Let  $S \in \{1, 2, 3, 4\}$  denote the number of connected components of a given interface perimeter. As before, let  $T$  denote the number of valid triangulations for a given connected perimeter. Then  $T = C_{n_j-2}$  for all connected components considered in our computational procedure. Finally, let  $\beta_{1,i,j}^k$ , where  $i = 1, \dots, C_{n_j-2}$ ,  $j = 1, \dots, S$ , and  $k = 1, \dots, P$ , denote the volume fraction of domain 1 given a fixed triangulation  $i$  of a connected component  $j$ , with  $n_j$  edge crossings, of an interface perimeter  $k$ . We arbitrarily pick domain 1 to be the domain with black corner components.

For a fixed triangulation  $i$  of the connected perimeter component  $j$  belonging to the interface perimeter  $k$ , we must compute  $\beta_{1,i,j}^k$ , the volume fraction occupied by domain 1. To do so we recall two basic results from analytic

geometry.

1. The volume of a *parallelepiped* spanned by the three vectors  $\mathbf{a} = (a_1, a_2, a_3)$ ,  $\mathbf{b} = (b_1, b_2, b_3)$ , and  $\mathbf{c} = (c_1, c_2, c_3)$  is given by:

$$V = |\det(\mathbf{a}, \mathbf{b}, \mathbf{c})| = \left| \det \begin{pmatrix} a_1 & b_1 & c_1 \\ a_2 & b_2 & c_2 \\ a_3 & b_3 & c_3 \end{pmatrix} \right| \quad (3.11)$$

2. The volume of a *tetrahedron* (i.e. a triangular pyramid) with vertices  $\mathbf{a}$ ,  $\mathbf{b}$ ,  $\mathbf{c}$ , and  $\mathbf{d}$  is given by:

$$V = \frac{1}{6} |\det(\mathbf{a} - \mathbf{b}, \mathbf{b} - \mathbf{c}, \mathbf{c} - \mathbf{d})| \quad (3.12)$$

For each valid triangulation of the interface perimeter there is a set of tetrahedra that decompose the space occupied by domain 1 inside the cell. Thus, given the set of crossings and the black corners in the corner 2-coloring, we can compute  $\beta_{1,i,j}^k$  using Eq. 3.12. For the hexagon case, we use Eq. 3.11 in addition to Eq. 3.12. To do so, the crossings and the corners are treated as vectors in 3D Cartesian space.

Fig. 3.10 illustrates, for a given triangulation of the glider perimeter in case 5, how the space occupied by domain 1 is defined by the interface surface and can be decomposed into five tetrahedra. We arbitrarily pick this particular triangulation to demonstrate our procedure.

To compute  $V_1$ , the total volume of the space occupied by domain 1 in Fig. 3.10, we compute the sum of five tetrahedron volumes. These five

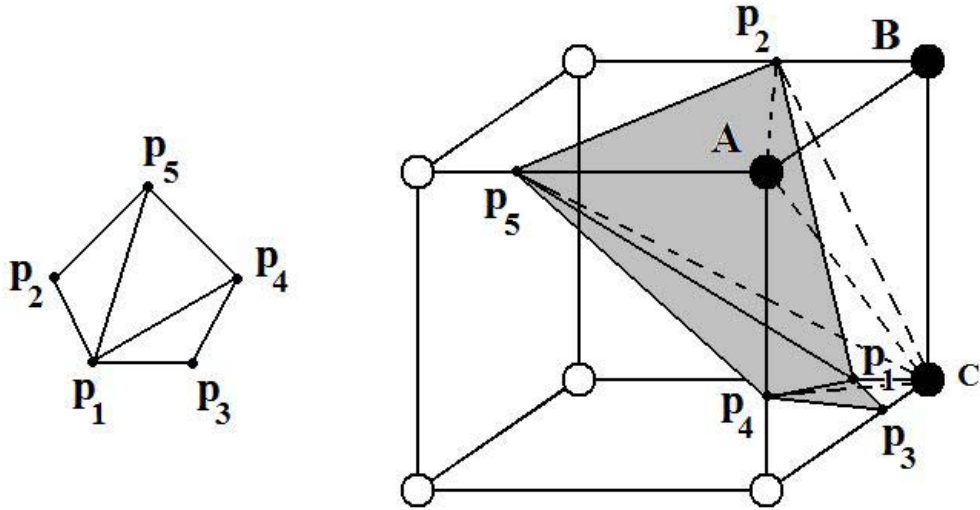


Figure 3.10: Decomposition of the space occupied by domain 1 into five tetrahedra in one of five possible triangulations in the glider case (case 5). The crossings are the vertices  $\mathbf{p}_i$ , where  $i = 1, \dots, 5$ . The black corners are labeled  $A$ ,  $B$  and  $C$ .

tetrahedra have vertices selected from the five edge crossings on the interface perimeter, labeled  $\mathbf{p}_i$ , where  $i = 1, \dots, 5$ , and the three black corners in the corner 2-coloring of the cell labeled  $A$ ,  $B$  and  $C$ . They all share the corner vertex  $C$ .

The vertices of the five tetrahedra  $T_5$ ,  $i = 1, \dots, 5$ , are given below.

1.  $\mathbf{p}_1, \mathbf{p}_3, \mathbf{p}_4$ , and  $C$  for  $T_1$ .
2.  $\mathbf{p}_1, \mathbf{p}_4, \mathbf{p}_5$ , and  $C$  for  $T_2$ .
3.  $\mathbf{p}_1, \mathbf{p}_2, \mathbf{p}_5$ , and  $C$  for  $T_3$ .
4.  $\mathbf{p}_2, A, B$ , and  $C$  for  $T_4$ .
5.  $\mathbf{p}_2, \mathbf{p}_5, A$ , and  $C$  for  $T_5$ .

We use Eq. 3.12 to calculate the five tetrahedron volumes  $V_{1,i}$ ,  $i = 1, \dots, 5$ , so that  $V_1 = \sum_{i=1}^5 V_{1,i}$ .

In the hexagon case, the space occupied by domain 1 in the cell is composed of tetrahedra and half a parallelepiped. In this instance we also use Eq. 3.11 to compute the volume of the half parallelepiped.

### 3.4.2 Surface Areas

As with the volume fraction  $\beta_1$ , we now define the interface surface area  $A$  using similar notation.

Let  $A_{i,j}^k$ , where again  $i = 1, \dots, C_{n_j-2}$ ,  $j = 1, \dots, S$ , and  $k = 1, \dots, P$ , denote the surface area of the interface surface bounded by a connected component  $j$ ,

with  $n_j$  edge crossings, of an interface perimeter  $k$ , given a fixed triangulation  $i$ . To compute  $A_{i,j}^k$ , we use the 3D coordinates of the edge crossings in a Cartesian space and apply the following result.

The area of a *triangle* with vertices  $\mathbf{a}$ ,  $\mathbf{b}$ , and  $\mathbf{c}$  embedded in 3D space is given by:

$$A = \frac{1}{2} \|(\mathbf{b} - \mathbf{a}) \times (\mathbf{c} - \mathbf{a})\| \quad (3.13)$$

The glider interface surface consists of three triangular elements, as a result of Theorem 3.1. In Fig. 3.10, we follow the triangulation that was arbitrarily chosen (where vertex  $\mathbf{p}_1$  has degree equal to four) and use the coordinates of the  $\mathbf{p}_i$  crossings,  $i = 1, \dots, 5$ , to calculate the surface area  $A_{i,j}^k$  of the interface surface. This is given as the sum of three triangular areas:

$$A = \frac{1}{2} \|(\mathbf{p}_2 - \mathbf{p}_1) \times (\mathbf{p}_5 - \mathbf{p}_1)\| + \frac{1}{2} \|(\mathbf{p}_5 - \mathbf{p}_1) \times (\mathbf{p}_4 - \mathbf{p}_1)\| + \frac{1}{2} \|(\mathbf{p}_4 - \mathbf{p}_1) \times (\mathbf{p}_3 - \mathbf{p}_1)\| \quad (3.14)$$

### 3.4.3 Formulas

Given a corner 2-coloring and an interface perimeter, let  $n$  denote the total number of edge crossings. Then  $n = \sum_{j=1}^S n_j$ . We use  $A_{[\text{comp}]}$  to denote the area  $A_{i,j}^k$  of the surface bounded by the given connected perimeter component with fixed triangulation  $i$  (*e.g.*,  $A_{\text{plane}}$ ,  $A_{\text{hexagon}}$ ). Similarly we use  $\beta_{[\text{comp}]}$  to denote the volume fraction of domain 1  $\beta_{1,i,j}^k$  for the given triangulation of the

perimeter component. These quantities are computed using Eq. 3.12, Eq. 3.11 and Eq. 3.13. We assume that the volumes of domain 1 have been normalized.

From Figs. 3.4, 3.5, and 3.6 we arrive at Table 3.1, which gives the number of triangulations ( $T_i$ ,  $i = 1, \dots, S$ ) for the connected perimeter components  $j$ , where  $j = 1, \dots, S$ , with  $n_i$ ,  $i = 1, \dots, S$ , edge crossings in all the valid interface perimeters in 3D cells.

We use Table 3.1, to give formulas for the surface area  $A$  and volume fraction  $\beta_1$  of domain 1 in each of the fourteen non-isomorphic cases. Note that Table 3.1 lists all theoretically valid interface perimeters, and that in our computational procedure we exclude all terms with hexagonoid, twisteroid, octagonoid-I or duodecagonoid-I surfaces.

For the seven non-isomorphic cases 1, 2, 5, 8, 9, 10, and 11, where  $P = S = 1$ , the formulas are simply given by:

$$A = \frac{1}{C_{n_{[\text{comp}]}-2}} \sum_{i=1}^{C_{n_{[\text{comp}]}-2}} A_{[\text{comp}],i} , \quad (3.15)$$

and

$$\beta = \frac{1}{C_{n_{[\text{comp}]}-2}} \sum_{i=1}^{C_{n_{[\text{comp}]}-2}} \beta_{[\text{comp}],i} , \quad (3.16)$$

where the connected perimeter component corresponds to either a corner, an edge, a glider, a plane, a hexagon, a twister-I, or a twister-II, and  $C_{n_{[\text{comp}]}-2}$  is the number of triangulations of that connected component. Note that  $T = C_{n_{[\text{comp}]}-2}$  in all these cases.



Case	$n$	$S$	$n_1$	$T_1$	$n_2$	$T_2$	$n_3$	$T_3$	$n_4$	$T_4$
Corner	3	1	3	1						
Edge/Plane	4	1	4	2						
Glider	5	1	5	5						
Hexagon/Twister-I Twister-II/	6	1	6	14						
<b>Hexagonoid</b>	6	1	6	4						
<b>Twisteroid</b>	7	1	7	22						
Two Corners-I/Two Corners-II	6	2	3	1	3	1				
Three Corners	9	3	3	1	3	1	3	1		
Four Corners (i)-(ii)	12	4	3	1	3	1	3	1	3	1
Hexagon + Corner	9	2	6	14	3	1				
Hexagon + Two Corners (i)-(iv)	12	3	6	14	3	1	3	1		
<b>Hexagonoid + Corner (i)-(iii)</b>	9	2	6	4	3	1				
<b>Hexagonoid + Two Corners (i)-(xii)</b>	12	3	6	4	3	1	3	1		
Glider + Corner (i)-(ii)	8	2	5	5	3	1				
Two Edges (i)-(ii)	8	2	4	2	4	2				
Edge + Corner	7	2	4	2	3	1				
<b>Two Hexagonoids (i)-(vi)</b>	12	2	6	4	6	4				
<b>Octagonoid-I (i)-(ii)</b>	8	1	8	6						

Table 3.1: Properties of all the valid interface perimeters in 3D cells. Lower roman letters indicate the number of distinct interface perimeters with similar connected components. Note that there are two distinct interface perimeters with two corners, one corresponding to the non-isomorphic case 3, and the other corresponding to the non-isomorphic case 4. Also note that all perimeters with hexagonoid, twisteroid and octagonoid-I components (in bold) were excluded in our implementation.

For the seven remaining cases 3, 4, 6, 7, 12, 13, and 14, the formulas are presented below.

1. *Case 4* Two Corners-I

$$A = \sum_{j=1}^2 A_{\text{corner},j} , \quad (3.17)$$

$$\beta = \sum_{j=1}^2 \beta_{\text{corner},j} . \quad (3.18)$$

2. *Case 13* Two Edges (i)-(ii)

$$A = \frac{1}{2} \sum_{k=1}^2 \sum_{j=1}^2 \left( \frac{1}{2} \sum_{i=1}^2 A_{\text{edge},i,j}^k \right) , \quad (3.19)$$

$$\beta = \frac{1}{2} \left( 1 + \sum_{j=1}^2 \frac{1}{2} \sum_{i=1}^2 (\beta_{\text{edge},i,j}^1 - \beta_{\text{edge},i,j}^2) \right) . \quad (3.20)$$

3. *Case 6* Edge and Corner

$$A = \frac{1}{2} \sum_{i=1}^2 A_{\text{edge},i} + A_{\text{corner}} , \quad (3.21)$$

$$\beta = \frac{1}{2} \sum_{i=1}^2 \beta_{\text{edge},i} + \beta_{\text{corner}} . \quad (3.22)$$

4. *Case 12* Glider and Corner (i)-(ii)

$$A = \frac{1}{2} \sum_{k=1}^2 \left( \frac{1}{5} \sum_{i=1}^5 A_{\text{glider},i}^k + A_{\text{corner}}^k \right) , \quad (3.23)$$

$$\beta = \frac{1}{2} \left( 1 + \frac{1}{5} \sum_{i=1}^5 (\beta_{\text{glider},i}^1 - \beta_{\text{glider},i}^2) + \beta_{\text{corner}}^1 - \beta_{\text{corner}}^2 \right) . \quad (3.24)$$

5. *Case 3* Two Corners-II

$$A = \sum_{j=1}^2 A_{\text{corner},j} , \quad (3.25)$$

$$\beta = \sum_{j=1}^2 \beta_{\text{corner},j} . \quad (3.26)$$

6. *Case 7* Three Corners + Hexagon and Corner

$$A = \frac{1}{2} \left( \sum_{j=1}^3 A_{\text{corner},j}^1 + \frac{1}{14} \sum_{i=1}^{14} A_{\text{hexagon},i}^2 + A_{\text{corner}}^2 \right) \quad (3.27)$$

$$\beta = \frac{1}{2} \left( \sum_{j=1}^3 \beta_{\text{corner},j}^1 + \frac{1}{14} \sum_{i=1}^{14} \beta_{\text{hexagon},i}^2 - \beta_{\text{corner}}^2 \right) \quad (3.28)$$

7. *Case 14* Four Corners (i)-(ii) + Hexagon and Two Corners (i)-(iv)

$$A = \frac{1}{6} \left( \sum_{k=1}^2 \sum_{j=1}^4 A_{\text{corner},j}^k + \sum_{k=3}^6 \left( \frac{1}{14} \sum_{i=1}^{14} A_{\text{hexagon},i}^k + \sum_{j=1}^2 A_{\text{corner},j}^k \right) \right) , \quad (3.29)$$

$$\begin{aligned}
\beta &= \frac{1}{6} \left( 1 + \sum_{j=1}^4 (\beta_{\text{corner},j}^1 - \beta_{\text{corner},j}^2) \right) \\
&+ \frac{1}{6} \sum_{k=3}^5 \left( 1 - \frac{1}{14} \sum_{i=1}^{14} (\beta_{\text{hexagon},i}^k + \beta_{\text{corner},1}^k - \beta_{\text{corner},2}^k) \right) \\
&+ \frac{1}{6} \left( \frac{1}{14} \sum_{i=1}^{14} \beta_{\text{hexagon},i}^6 - \beta_{\text{corner},1}^6 + \beta_{\text{corner},2}^6 \right). \quad (3.30)
\end{aligned}$$

Note that for those cases where we average over more than one interface perimeter, our formulas are consistent with the domain components so that no such case where a black domain component is added to a white domain component can occur.

### 3.5 Implementation in *FronTier*

In grid-based front-tracking, the contact interface is reconstructed for each cell cut by a fluid interface. In the front tracking package *FronTier*, there is a two-component block file that identifies from the components of the cell corners (the corner 2-coloring) which of the fourteen non-isomorphic cases occurs in each cell. This file can be found in the location: *FronTier/src/intfc/iblk2.c*. For each case, there is a corresponding local void function called *blk\_case\_k\_comp2\_bis()*, where  $k = 1, \dots, 14$ , which computes the surface area of the reconstructed interface and the volume fraction of domain 1, arbitrarily picked as the one with black corner components.

Inside each case we use volume and area functions designed to

compute these quantities for each of the connected interface perimeters (*e.g.*, *area\_glider()*, *volume\_hexagon()*). The arguments to these functions are the interface crossings with the cell edges and the black corners in the corner 2-coloring of the cell. Below we present the standard model used in writing these functions and explain how to use them.

### 3.5.1 Standard Model

The standard model of Fig. 3.11 provides, for each non-isomorphic case, a fixed and standard configuration of the interface with respect to both the 2-coloring of the cell corners and the ordering of the crossings relative to the cell corners. This model, which is set up in the code *FronTier* by specific rotation functions, eliminates ambiguities associated with looking at the same case from different frames of reference (through rotations and distinct crossing positions). We follow it consistently to design volume and area functions in each case.

In order to fix the relative position of the crossings with respect to the cell corners, we adopt the lexicographic corner ordering shown in Fig. 3.12. At the start of each of the main functions *blk\_case\_k\_comp2\_bis()*, where  $k = 1, \dots, 14$ , we define the cell corners according to this prescribed ordering. This specification completes the reference frame needed to write the volume and area functions. In effect, the three degrees of freedom provided by the 2-coloring of cell corners, the orientation of the  $i$ ,  $j$ , and  $k$  axes and the ordering of the crossings relative to the black corners are now all fixed.

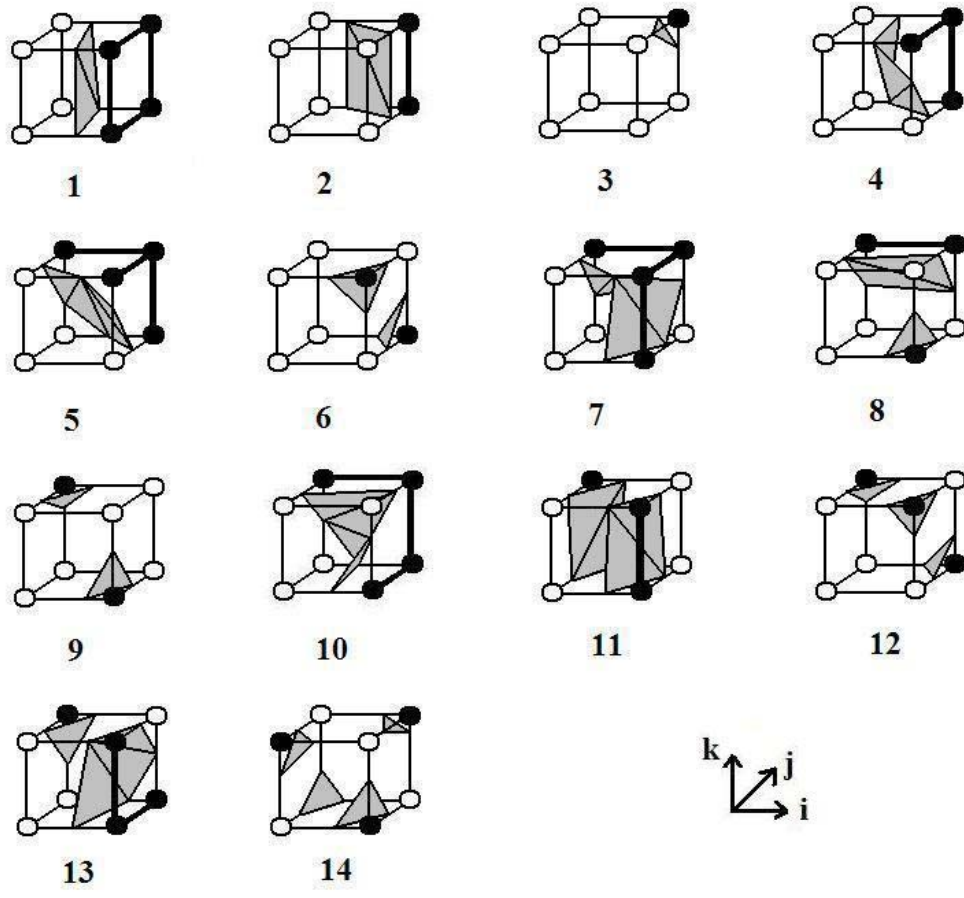


Figure 3.11: Standard model for the fourteen cases implemented in *FronTier*: 1) Plane, 2) Edge, 3) Corner, 4) Glider, 5) Hexagon, 6) Two corners-I, 7) Twister-I, 8) Edge and corner, 9) Two corners-II, 10) Twister-II, 11) Two edges, 12) Three corners, 13) Glider and corner, 14) Four corners.

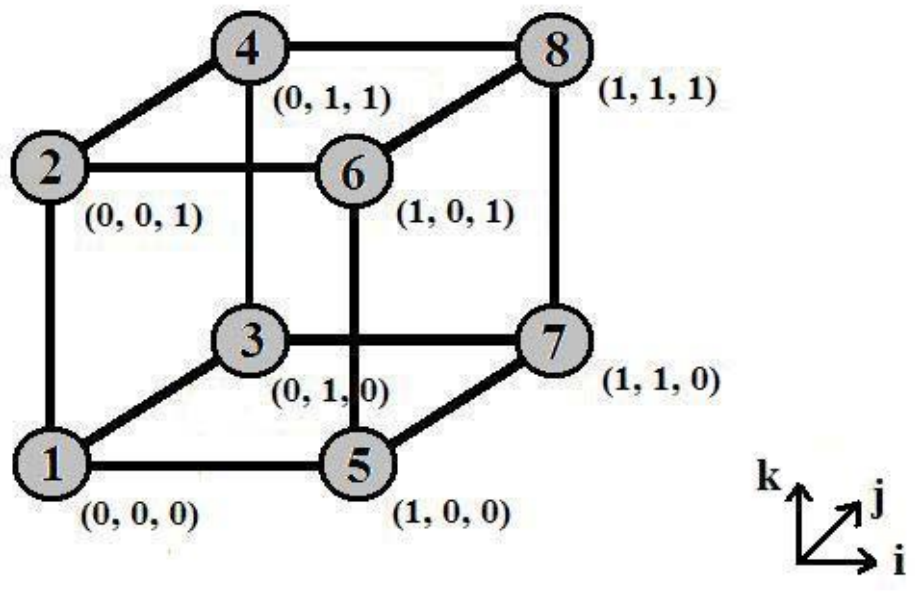


Figure 3.12: Location of the cell corners used in the standard model.

### 3.5.2 Area and Volume Functions

The area and volume functions are all local *float* functions that return, respectively, interface surface areas and light volume fractions for each case. Seven sets of functions describe each of the connected perimeter components, including the two topologically distinct twister perimeters. The labeling of these functions is straightforward. For instance, *area\_edge()* is the area function that returns the interface surface area for an edge element and *volume\_twister1()* is the volume function that returns the volume fraction for the twister-I element, as depicted in Fig. 3.11.

The arguments for the area functions are the crossings in the  $i$ ,  $j$ ,  $k$  directions. Since a 3D cell has twelve edges, with three sets of four edges parallel to each of the axes, we need to specify for each crossing the edge on which it is found. To do so we associate a boolean ordered pair to each crossing that conforms to the standard model and gives the location of the edge with respect to the other two directions. Thus, the location of the  $i$ ,  $j$  and  $k$  crossings are provided by the ordered boolean pairs  $(ij, ik)$ ,  $(ji, jk)$  and  $(ki, kj)$ . Each element of the pair has a value of 0 or 1 which, in accordance to the standard model, give the location of the edge with respect to the two other directions. For instance, if  $(ij, ik) = (0, 1)$  is given as the pair associated with an  $i$  crossing, then this crossing must occur on the upper front edge, where  $j = 0$  and  $k = 1$ . Similarly, if  $(ki, kj) = (0, 1)$  is a  $k$  crossing, then it must occur on the left-back edge, where  $i = 0$  and  $j = 1$ .

For cases with multiple crossings in the same direction, we add numbers at the end of the pairs. In the edge case, for instance, we have two  $j$  crossings



which are identified by the pairs  $(ji1, jk1)$  and  $(ji2, jk2)$ .

Below we present the input arguments needed for each area function.

1. *float* area\_corner(BLK\_CRX\*, *ij, ik, ji, jk, ki, kj*);
  - boolean[2](*ij, ik*): crossing in the *i* direction.
  - boolean[2](*ji, jk*): crossing in the *j* direction.
  - boolean[2](*ki, kj*): crossing in the *k* direction.
2. *float* area\_edge(BLK\_CRX\*, *ij1, ik1, ij2, ik2, ji1, jk1, ji2, jk2*);
  - boolean[2](*ij1, ik1*): first crossing in the *i* direction.
  - boolean[2](*ij2, ik2*): second crossing in the *i* direction.
  - boolean[2](*ji1, jk1*): first crossing in the *j* direction.
  - boolean[2](*ji2, jk2*): second crossing in the *j* direction.
3. *float* area\_plane(BLK\_CRX\*, *ij1, ik1, ij2, ik2, ij3, ik3, ij4, ik4*);
  - boolean[2](*ij1, ik1*): first crossing in the *i* direction.
  - boolean[2](*ij2, ik2*): second crossing in the *i* direction.
  - boolean[2](*ij3, ik3*): third crossing in the *i* direction.
  - boolean[2](*ij4, ik4*): fourth crossing in the *i* direction.
4. *float* area\_glider(BLK\_CRX\*, *ij1, ik1, ij2, ik2, ij3, ik3, ji, jk, ki, kj*);
  - boolean[2](*ij1, ik1*): first crossing in the *i* direction.
  - boolean[2](*ij2, ik2*): second crossing in the *i* direction.

- $\text{boolean}[2](ji3, jk3)$ : third crossing in the i direction.
  - $\text{boolean}[2](ji, jk)$ : crossing in the j direction.
  - $\text{boolean}[2](ki, kj)$ : crossing in the k direction.
5. *float*  $\text{area\_hexagon}(\text{BLK\_CRX}^*, ij1, ik1, ij2, ik2, ji1, jk1, ji2, jk2, ki1, kj1, ki2, kj2)$ ;
- $\text{boolean}[2](ij1, ik1)$ : first crossing in the i direction.
  - $\text{boolean}[2](ij2, ik2)$ : second crossing in the i direction.
  - $\text{boolean}[2](ji1, jk1)$ : first crossing in the j direction.
  - $\text{boolean}[2](ji2, jk2)$ : second crossing in the j direction.
  - $\text{boolean}[2](ki1, kj1)$ : first crossing in the k direction.
  - $\text{boolean}[2](ki2, kj2)$ : second crossing in the k direction.
6. *float*  $\text{area\_twister1}(\text{BLK\_CRX}^*, ij1, ik1, ij2, ik2, ji1, jk1, ji2, jk2, ki1, kj1, ki2, kj2)$ ;
- $\text{boolean}[2](ij1, ik1)$ : first crossing in the i direction.
  - $\text{boolean}[2](ij2, ik2)$ : second crossing in the i direction.
  - $\text{boolean}[2](ji1, jk1)$ : first crossing in the j direction.
  - $\text{boolean}[2](ji2, jk2)$ : second crossing in the j direction.
  - $\text{boolean}[2](ki1, kj1)$ : first crossing in the k direction.
  - $\text{boolean}[2](ki2, kj2)$ : second crossing in the k direction.

7. *float* area\_twister2(BLK\_CRX\*, *ij1, ik1, ij2, ik2, ji1, jk1, ji2, jk2, ki1, kj1, ki2, kj2*);

- boolean[2](*ij1, ik1*): first crossing in the *i* direction.
- boolean[2](*ij2, ik2*): second crossing in the *i* direction.
- boolean[2](*ji1, jk1*): first crossing in the *j* direction.
- boolean[2](*ji2, jk2*): second crossing in the *j* direction.
- boolean[2](*ki1, kj1*): first crossing in the *k* direction.
- boolean[2](*ki2, kj2*): second crossing in the *k* direction.

BLK\_CRX\* is a structure that contains information about the crossings.

The arguments for the volume functions are the same as those of the area functions (*i.e.*, crossings in the *i, j, k* directions), with the addition of the black corners in the corner 2-colorings. We specify below the black corner input for these functions in accordance with Fig. 3.12.

1. *float* volume\_corner(BLK\_CRX\*, ... , crn8);
2. *float* volume\_edge(BLK\_CRX\*, ... , crn8, crn7);
3. *float* volume\_plane(BLK\_CRX\*, ... , crn7, crn8, crn5, crn6);
4. *float* volume\_glider(BLK\_CRX\*, ... , crn6, crn8, crn7);
5. *float* volume\_hexagon(BLK\_CRX\*, ... , crn6, crn7, crn4, crn8);
6. *float* volume\_twister1(BLK\_CRX\*, ... , crn5, crn6, crn8, crn4);
7. *float* volume\_twister2(BLK\_CRX\*, ... , crn5, crn7, crn8, crn4);

## Chapter 4

### Appendix I - Figures and Tables for Mixing Zone Edge Errors

The following are figures and tables showing convergence orders and statistics for the position errors of the mixing zone edges. These are analogous to Fig. 2.3 and Table 2.1 shown in Chap. 2. We consider  $45^\circ$  angular windows at the north and south pole regions for the non-offset cases, and  $40^\circ$  angular windows at the north pole, south pole and equator regions for the offset cases. We average over an ensemble of  $N = 5$  realizations.

Grid	$\Delta x$	Centerline Error						Width Error					
		Singly Shocked			Doubly Shocked			Singly Shocked			Doubly Shocked		
		M	STD	O	M	STD	O	M	STD	O	M	STD	O
100	1/4	-0.01	0.05	-	0.04	0.26	-	0.22	0.42	-	1.85	0.77	-
200	1/8	-0.01	0.06	-0.1	-0.18	0.12	0.4	0.06	0.16	1.5	0.29	0.46	1.5
400	1/16	-0.01	0.02	1.1	-0.04	0.18	0.1	0.06	0.08	0.7	0.28	0.24	0.7

Table 4.1: Convergence statistics for the errors in the mixing zone edges, averaged over time values and over an ensemble of size  $N = 5$ , in units of cm. Edge position defined relative to the angular window  $\theta \in [45^\circ, 90^\circ]$  at the north pole. Non-offset case.

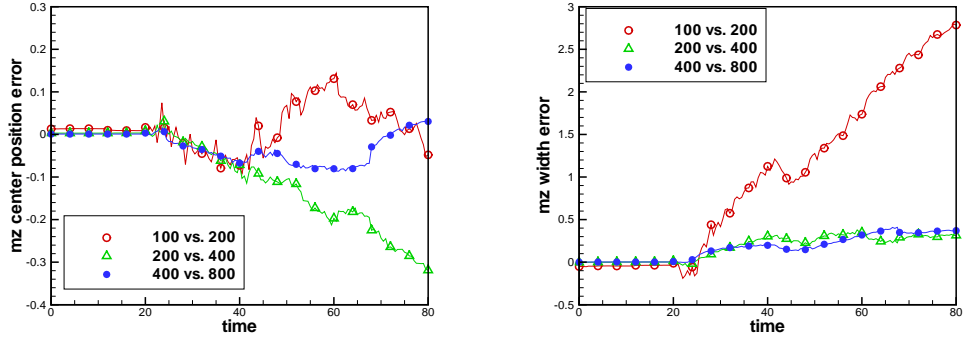


Figure 4.1: Mesh convergence of the mixing zone edges position errors, in units of length (cm). The mixing zone is defined relative to the  $45^\circ$  window  $\theta \in [45^\circ, 90^\circ]$  at the north pole, and averaged over an ensemble of  $N = 5$  realizations. Non-offset case. Left: Mixing zone center line. Right: Mixing zone width.

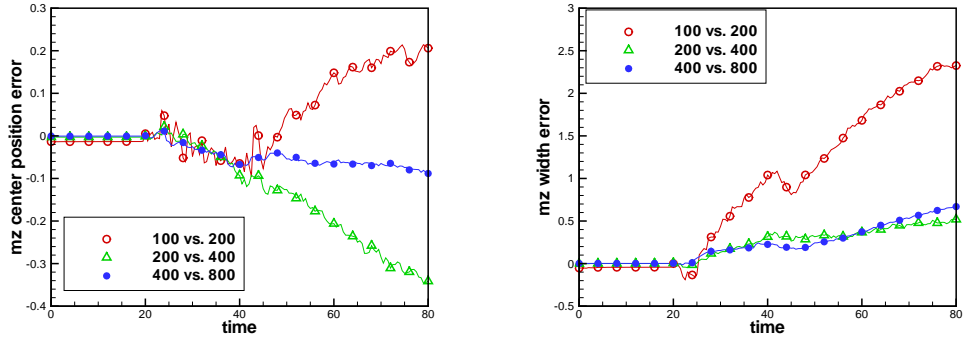


Figure 4.2: Mesh convergence of the mixing zone edges position errors, in units of length (cm). The mixing zone is defined relative to the  $45^\circ$  window  $\theta \in [-90^\circ, -45^\circ]$  at the south pole, and averaged over an ensemble of  $N = 5$  realizations. Non-offset case. Left: Mixing zone center line. Right: Mixing zone width.

Grid	$\Delta x$	Centerline Error						Width Error					
		Singly Shocked			Doubly Shocked			Singly Shocked			Doubly Shocked		
		M	STD	O	M	STD	O	M	STD	O	M	STD	O
100	1/4	-0.02	0.06	-	0.11	0.18	-	0.19	0.39	-	1.66	0.83	-
200	1/8	-0.01	0.06	0.2	-0.21	0.15	-0.2	0.06	0.15	1.4	0.39	0.55	1.2
400	1/16	-0.01	0.02	1.1	-0.06	0.18	0.3	0.06	0.08	0.6	0.39	0.37	0.4

Table 4.2: Convergence statistics for the errors in the mixing zone edges, averaged over time values and over an ensemble of size  $N = 5$ , in units of cm. Edge position defined relative to the angular window  $\theta \in [-90^\circ, -45^\circ]$  at the south pole. Non-offset case.

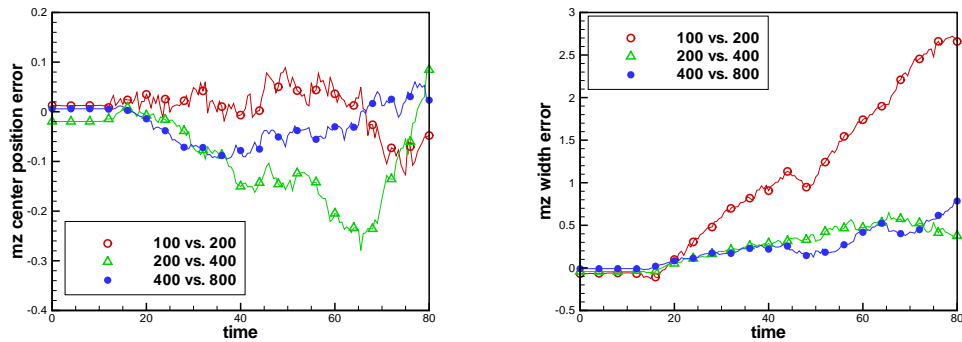


Figure 4.3: Mesh convergence of the mixing zone edges position errors, in units of length (cm). The mixing zone is defined relative to the  $40^\circ$  window  $\theta \in [50^\circ, 90^\circ]$  at the north pole, and averaged over an ensemble of  $N = 5$  realizations. Offset case. Left: Mixing zone center line. Right: Mixing zone width.

Grid	$\Delta x$	Centerline Error						Width Error					
		Singly Shocked			Doubly Shocked			Singly Shocked			Doubly Shocked		
		M	STD	O	M	STD	O	M	STD	O	M	STD	O
100	1/4	0.02	0.06	-	0.00	0.16	-	0.27	0.43	-	1.78	1.04	-
200	1/8	-0.04	0.07	-0.2	-0.14	0.18	-0.6	0.07	0.26	0.9	0.44	0.94	0.7
400	1/16	-0.03	0.04	0.6	-0.02	0.09	1.2	0.09	0.10	1.1	0.37	0.24	1.5

Table 4.3: Convergence statistics for the errors in the mixing zone edges, averaged over time values and over an ensemble of size  $N = 5$ , in units of cm. Edge position defined relative to the angular window  $\theta \in [50^\circ, 90^\circ]$  at the north pole. Offset case.

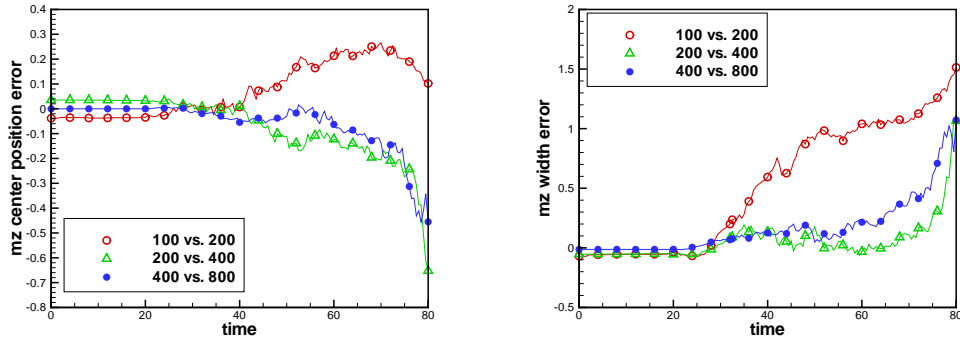


Figure 4.4: Mesh convergence of the mixing zone edges position errors, in units of length (cm). The mixing zone is defined relative to the  $40^\circ$  window  $\theta \in [-20^\circ, 20^\circ]$  at the equator, and averaged over an ensemble of  $N = 5$  realizations. Offset case. Left: Mixing zone center line. Right: Mixing zone width.

Grid	$\Delta x$	Centerline Error						Width Error					
		Singly Shocked			Doubly Shocked			Singly Shocked			Doubly Shocked		
		M	STD	O	M	STD	O	M	STD	O	M	STD	O
100	1/4	-0.02	0.06	-	0.17	0.22	-	0.06	0.22	-	1.01	0.36	-
200	1/8	0.02	0.06	0.0	-0.16	0.34	-0.4	-0.01	0.13	0.9	0.12	0.49	0.7
400	1/16	-0.01	0.02	2.0	-0.11	0.19	0.8	0.02	0.05	1.2	0.30	0.35	0.1

Table 4.4: Convergence statistics for the errors in the mixing zone edges, averaged over time values and over an ensemble of size  $N = 5$ , in units of cm. Edge position defined relative to the angular window  $\theta \in [-20^\circ, 20^\circ]$  at the equator. Offset case.

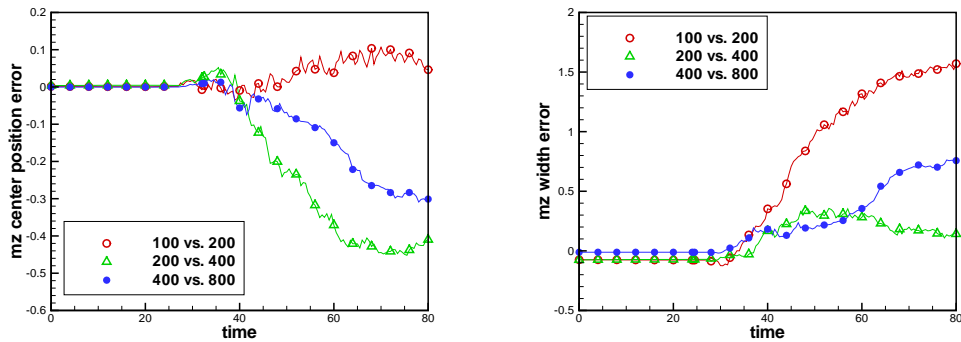


Figure 4.5: Mesh convergence of the mixing zone edges position errors, in units of length (cm). The mixing zone is defined relative to the  $40^\circ$  window  $\theta \in [-90^\circ, -50^\circ]$  at the south pole, and averaged over an ensemble of  $N = 5$  realizations. Offset case. Left: Mixing zone center line. Right: Mixing zone width.



Grid	$\Delta x$	Centerline Error						Width Error					
		Singly Shocked			Doubly Shocked			Singly Shocked			Doubly Shocked		
		M	STD	O	M	STD	O	M	STD	O	M	STD	O
100	1/4	0.00	0.03	-	0.05	0.10	-	-0.03	0.14	-	1.19	0.44	-
200	1/8	0.01	0.02	0.1	-0.32	0.17	-1.4	-0.06	0.14	-0.1	0.23	0.29	1.3
400	1/16	0.00	0.01	1.1	-0.16	0.20	0.2	0.01	0.06	1.4	0.42	0.32	-0.4

Table 4.5: Convergence statistics for the errors in the mixing zone edges, averaged over time values and over an ensemble of size  $N = 5$ , in units of cm. Edge position defined relative to the angular window  $\theta \in [-90^\circ, -50^\circ]$  at the south pole. Offset case.

## Chapter 5

### Appendix II - Proof of Proposition 3.6

Here we prove Proposition 3.6 of Chap. 3, which states that the values of  $T$  in Fig. 3.9 are correct. We do so by deriving the number of valid triangulations for all isomorphism classes of connected interface perimeters.

The unique elements in the seven classes with  $f = 0$  only admit valid triangulations since they are distinguished by isomorphism classes of corner 2-colorings that have no faces with four edge crossings. As a result, the elements in these classes can never fail to satisfy the validity condition and, from Theorem 3.2, must satisfy the identity  $T = C_{n-2}$ . For perimeter classes with  $f > 0$ , we proceed by proving some important results (Propositions 5.1 through 5.7) about the valid triangulations of polygons that are isomorphic to elements in each connected perimeter class. From these propositions we infer the values of  $T$  in each class (Corollaries 5.1 through 5.7). In the course of these derivations, we give intermediary results in the form of Lemmas 5.1 through 5.5.

When  $f > 0$  there is a constraint on each face with four edge crossings

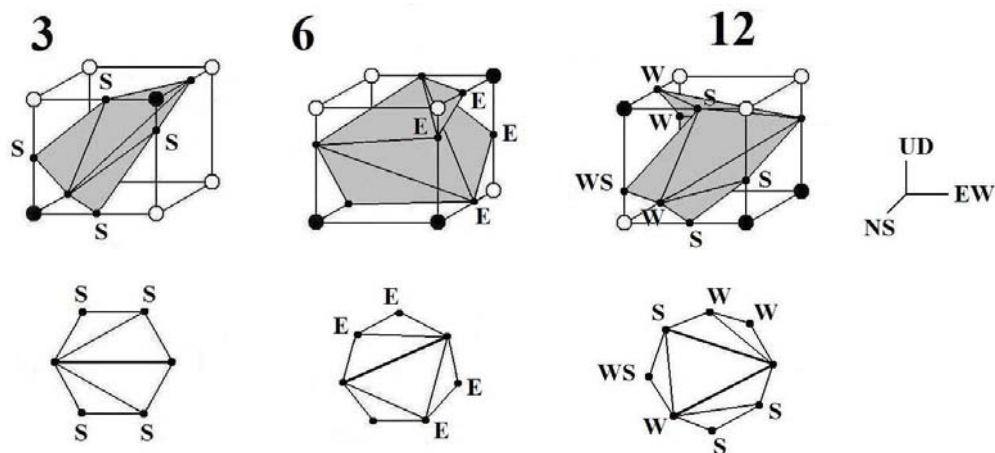


Figure 5.1: Examples of valid triangulations for elements in the hexagonoid (left), twisteroid (middle) and octagonoid-I (right) isomorphism classes of connected perimeters (cases 3, 6, and 12). For the left and middle figures,  $f = 1$ , and for the right figure,  $f = 2$ . Edge crossings belonging to a common face are labeled according to the orientation of that face, namely U, D, E, W, N, and S. Validity is then guaranteed if no edges on a common face are linked by diagonals. This is the case in all three figures: in the left, there are no  $\overline{SS}$  diagonals; in the middle, there are no  $\overline{EE}$  diagonals; in the right, there are neither  $\overline{WW}$  nor  $\overline{SS}$  diagonals.

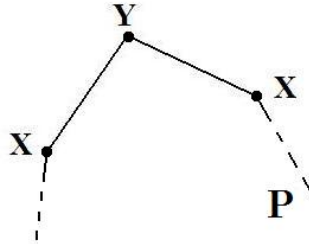


Figure 5.2: Illustration of Lemma 5.1.  $P$  is a polygon with the property that two of its adjacent edges give the sequence of vertices  $(X, Y, X)$ .

that restricts the number of valid triangulations. For these cases, we necessarily have the inequality  $T < C_{n-2}$ . Turning to the perimeter classes in cases 3, 6 and 12, with  $f = 1, 2$ , we first observe from Fig. 5.1 that at least one hexagonoid (left), twisteroid (middle), and octagonoid-I (right) triangulation is valid (*i.e.*, it does not include a diagonal linking edges on a common face) and, hence, that  $T > 0$ . The valid triangulations in Fig. 5.1 are picked arbitrarily. We label the edge crossings belonging to a common face according to the orientation of that face, namely U, D, E, W, N, and S (Up-Down, East-West, and North-South). In Corollaries 5.1, 5.2, and 5.3, we determine the value of  $T$  in these three cases, which obey the strict inequality  $0 < T < C_{n-2}$ .

From Definition 3.2, we allow no diagonal from a triangulation to lie on the cell surface (such a diagonal, which connects vertices on a common face of the cell, is called *invalid*). Moreover, this restriction also gives the following fundamental result.

**Lemma 5.1** *Consider a polygon  $P$ , such as the one shown in Fig. 5.2, which has two adjacent edges  $\overline{XY}$  sharing the vertex  $Y$ , where  $X, Y \in \{N, S, E, W, U, D\}$ . Then a valid triangulation of  $P$  must include a diagonal starting at the vertex  $Y$ .*

**Proof** Consider a triangulation of  $P$  that does not include a diagonal starting at the vertex  $Y$  (*i.e.*, with  $Y$  as an endpoint). Then, this triangulation must include the diagonal  $\overline{XX}$  connecting the two  $X$  vertices adjacent to  $Y$ , or fail to be complete. Since this diagonal is invalid, we conclude that a valid triangulation of  $P$  must include a diagonal starting at the vertex  $Y$ .  $\square$

Our approach in constructing a valid triangulation for a given  $n$ -gon  $P$  is incremental: at each stage of the construction we insert a new diagonal. From Theorem 3.1, we then have that such a construction consists of  $n - 3$  distinct stages. Our initial strategy is to identify any two adjacent edges of  $P$  which give a sequence of vertices  $(X, Y, X)$ , where  $X, Y \in \{N, S, E, W, U, D\}$ , and apply Lemma 5.1 to force the choice of the first diagonal (assuming there is at least one such sequence). In general, we look at all the valid choices for the first diagonal starting at the vertex  $Y$ . For each choice, we then move to the insertion of diagonal 2. Once again, we identify another arbitrary sequence of vertices  $(X, Y, X)$ , if any, where  $X, Y \in \{N, S, E, W, U, D\}$ , in the  $(n - 1)$ -gon resulting from the insertion of diagonal 1, and look at all possible valid choices for diagonal 2. To complete the valid triangulation of  $P$ , we proceed in this manner with the remaining diagonals. If no sequence of vertices  $(X, Y, X)$  is found at some stage in the construction, we resort to a broader strategy and

partition all possible choices of valid diagonals into isomorphism classes, where the isomorphism invariant is given by the cyclic ordering of vertices around the polygon that results from the diagonal insertion. This invariant does not differentiate between the two possible directions of the cycle (clockwise or counter-clockwise) and allows the inversion of vertices so that, for instance, the pentagons  $XYXYY$  and  $XXYXY$  are identical invariants. To identify these isomorphism classes of diagonals, we inspect all possible choices of valid diagonals through a systematic procedure, which involves placing diagonals linking vertices separated by one vertex, then placing diagonals linking vertices separated by two vertices, and so on until all choices of valid diagonals are exhausted. Note that, in some cases, there is a symmetry axis in the polygon that reduces the number of valid choices.

**Proposition 5.1** *A valid triangulation of the hexagon  $YXXZXX$ , where  $X, Y, Z \in \{N, S, E, W, U, D\}$ , must include the diagonal  $\overline{YZ}$ .*

**Proof** In Fig. 5.3 we show that no valid triangulation of the hexagon  $YXXZXX$ , where  $X, Y, Z \in \{N, S, E, W, U, D\}$ , which excludes the diagonal  $\overline{YZ}$ , can be constructed, as this is equivalent to proving the proposition. We arbitrarily start the triangulation at vertex  $Y$ , which is adjacent to two  $X$  vertices, and proceed by adding only valid diagonals. Then, according to Lemma 5.1, we can force the first diagonal to start at vertex  $Y$ . We see that there are two isomorphic choices for the first diagonal, namely any of the two possible diagonals  $\overline{XY}$  shown on the left of Fig. 5.3. These two diagonals follow the symmetry about the axis passing through  $Y$  and  $Z$ . We pick one

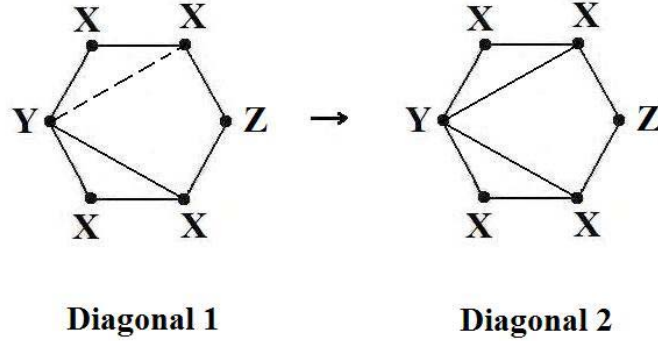


Figure 5.3: Illustration of Proposition 5.1 showing that no valid triangulation of the hexagon  $YXXZXX$ , which excludes the diagonal  $\overline{YZ}$ , can be constructed. We show the two valid isomorphic choices for the first diagonal (left) and the only valid choice for diagonal 2 (right) resulting from applying Lemma 5.1 at vertex  $Y$ . The solid line on the left is our arbitrary choice for diagonal 1, and the dotted line is the other isomorphic choice. These two diagonals follow the symmetry about the axis passing through  $Y$  and  $Z$ .

of these diagonals (the solid line) and move to the insertion of diagonal 2. Once again, we apply Lemma 5.1 at the vertex  $Y$ , since it is still adjacent to two  $X$  vertices. Then, the only choice for diagonal 2 is the other diagonal  $\overline{XY}$ . At this stage, only one diagonal needs to be inserted to complete the triangulation of the hexagon  $YXXZXX$ . Since the diagonal  $\overline{YZ}$  is excluded by hypothesis, we are left with only one choice for diagonal 3, namely the invalid diagonal  $\overline{XX}$  joining the two  $X$  vertices adjacent to  $Z$ . Therefore, we conclude that no valid triangulation of  $YXXZXX$  can be constructed if we exclude the diagonal  $\overline{YZ}$ .  $\square$

**Corollary 5.1**  $T = 4$  in the hexagonoid isomorphism class of connected perimeters.

**Proof** Perimeters in the hexagonoid class are hexagons since they have  $n = 6$  edge crossings. Looking at the left hexagon in Fig. 5.1, we see that it is in the form  $YXXZXX$  of the hexagon in Proposition 5.1, with  $X = S$ . This implies that a valid triangulation for a perimeter in the hexagonoid class (case 3 with  $f = 1$ ), such as the one depicted on the left of Fig. 5.1, includes the diagonal joining the two vertices that do not belong to a common cell face (the heavy line in the left hexagon of Fig. 5.1). There are exactly  $2^2 = 4$  distinct triangulations resulting from the inclusion of diagonal  $\overline{YZ}$  as a first diagonal, namely the two possible ones for each of the two quadrilaterals on either side of  $\overline{YZ}$ . As a result, the number of valid triangulations in the hexagonoid perimeter class is  $T = 4$ .  $\square$

We follow a similar argument to derive the value of  $T$  in the twisteroid case.

**Proposition 5.2** *A valid triangulation of the heptagon  $VXXYZXX$ , where  $X, Y, Z, V \in \{N, S, E, W, U, D\}$ , must include either the diagonal  $\overline{VY}$  or the diagonal  $\overline{VZ}$ .*

**Proof** In Fig. 5.4, we show that no valid triangulation of the heptagon  $VXXYZXX$ , where  $X, Y, Z \in \{N, S, E, W, U, D\}$ , which excludes the two diagonals  $\overline{VY}$  and  $\overline{VZ}$ , can be constructed, as this is equivalent to proving the proposition. We arbitrarily start the triangulation at vertex  $V$ , which is adjacent to two  $X$  vertices, and proceed by adding only valid diagonals. Then, according to Lemma 5.1, we can force the first diagonal to start at vertex  $V$ . We see that there are two isomorphic choices for the first diagonal, namely



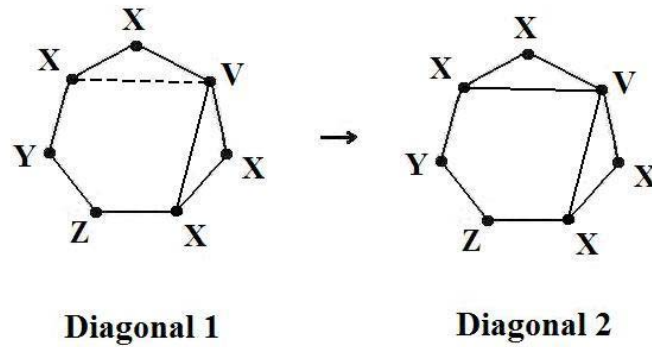


Figure 5.4: Illustration of Proposition 5.2 showing that no valid triangulation of the heptagon  $VXXYZXX$ , which excludes the two diagonals  $\overline{VY}$  and  $\overline{VZ}$ , can be constructed. We show the two valid isomorphic choices for the first diagonal (left) and the only valid choice for diagonal 2 (right) resulting from applying Lemma 5.1 at vertex  $V$ . The solid line on the left is our arbitrary choice for diagonal 1, and the dotted line is the other isomorphic choice. These two diagonals follow the symmetry about the line passing through  $V$  and the mid-point of edge  $\overline{EZ}$ .

any of the two possible diagonals  $\overline{VX}$  shown on the left of Fig. 5.4. These two diagonals follow the symmetry about the axis passing through  $V$  and the midpoint of edge  $\overline{EZ}$ , which separates two identical triplets of vertices  $(A, X, X)$ , where  $A \in \{Y, Z\}$ , according to the vertex inversion  $Y \leftrightarrow Z$ . We pick one of these diagonals (the solid line) and move to the insertion of diagonal 2. Once again, we apply Lemma 5.1 at vertex  $V$ , since it is still adjacent to two  $X$  vertices. Then, the only choice for diagonal 2 is the other diagonal  $\overline{VX}$ . At this stage, two more diagonals need to be inserted to complete the triangulation of the heptagon  $VXXYZXX$ . Since the two diagonals  $\overline{VY}$  and  $\overline{VZ}$  are excluded by hypothesis, we are left with only one choice for diagonal 3, namely the invalid diagonal  $\overline{XX}$  joining the two  $X$  vertices adjacent to the  $Y$  and  $Z$  vertices. Therefore, we conclude that no valid triangulation of  $VXXYZXX$  can be constructed if we exclude the two diagonals  $\overline{VY}$  and  $\overline{VZ}$ .  $\square$

**Corollary 5.2**  $T = 16$  in the twisteroid isomorphism class of connected perimeters.

**Proof** Perimeters in the twisteroid class are heptagons since they have  $n = 7$  edge crossings. Looking at the middle heptagon in Fig. 5.1, we see that it is in the form  $VXXYZXX$  of the heptagon in Proposition 5.2, with  $X = E$ . This implies that a valid triangulation for a perimeter in the twisteroid class (case 6 with  $f = 1$ ), such as the one depicted in the middle of Fig. 5.1, includes one of the two diagonals joining non-adjacent vertices that do not belong to a common cell face (*e.g.*, the heavy line in the middle heptagon of Fig. 5.1).

There are exactly 16 (not counting repetitions) distinct triangulations resulting from the inclusion of either  $\overline{VY}$  or  $\overline{VZ}$  as a first diagonal. In effect, for each diagonal there are 10 possible triangulations, namely those resulting from the two possibilities for the quadrilateral on one side of the diagonal and the five possibilities for the pentagon on the other side of the diagonal. Since there are two diagonals, the total number of triangulations is then 20. However, discarding repetitions reduces the number of distinct possibilities to 16. As a result, the number of valid triangulations in the twisteroid perimeter class is  $T = 16$ .  $\square$

**Proposition 5.3** *A valid triangulation of the octagon  $XXZYXX(XY)Y$ , where  $X, Y, Z \in \{N, S, E, W, U, D\}$ , must include the two diagonals  $\overline{ZY}$  and  $\overline{ZX}$ , whose endpoints  $X$  and  $Y$  are adjacent to the vertex  $(XY)$ .*

**Proof** In Fig. 5.5 we construct valid triangulations of the octagon  $XXZYXX(XY)Y$ , where  $X, Y, Z \in \{N, S, E, W, U, D\}$ , and show that any of these must include the two diagonals  $\overline{ZY}$  and  $\overline{ZX}$ , whose endpoints  $X$  and  $Y$  are adjacent to the vertex  $(XY)$ . We proceed by inserting only valid diagonals at each stage in the construction. At all stages in the construction, we discard trivial cases which already include both of these diagonals. We arbitrarily start the triangulation at the vertex  $X$  (the top vertex in Fig. 5.5), which is adjacent to two  $Y$  vertices. Then, according to Lemma 5.1, we can force the first diagonal to start at this vertex  $X$ . We see that there are three non-isomorphic choices for the first diagonal, all shown as cases a, b, and c in Fig. 5.5. In case c, the insertion of the diagonal  $\overline{XZ}$  leads to the hexagon  $XXYXXZ$  on the

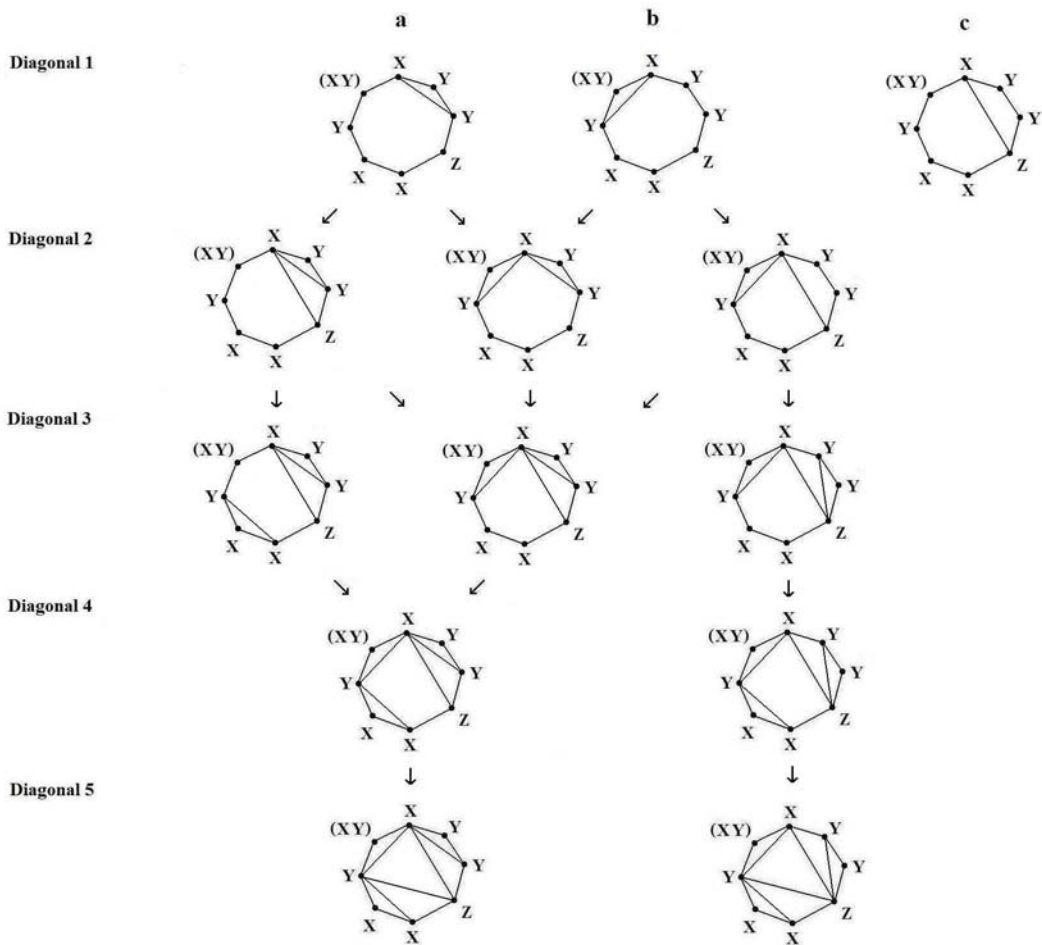


Figure 5.5: Illustration of Proposition 5.3 showing that any valid triangulation of the octagon  $XXZY YX(XY)Y$  must include the two diagonals  $\overline{ZY}$  and  $\overline{ZX}$ , whose endpoints  $X$  and  $Y$  are adjacent to the vertex  $(XY)$ . Cases a, b, and c depict the three valid non-isomorphic choices for the first diagonal.

left, so that, according to Proposition 5.1, the only choice for diagonal 2 (*i.e.*, the first diagonal in the triangulation of the hexagon) is the diagonal  $\overline{YZ}$ . Thus, the two diagonals in the Proposition must be included. For cases b and c, the choices for the remaining diagonals 2, 3, 4, and 5 are shown in Fig. 5.5. These result from applying Lemma 5.1 at either the top vertex  $X$  again, or at the vertex  $Y$  adjacent to vertex  $(XY)$ . Note that in one of the two subcases of b, our choices for diagonal 3 results from the two possible triangulations of the quadrilateral  $XYYZ$  on the right. In all of these cases, we eventually arrive at a valid triangulation that includes the two diagonals  $\overline{ZY}$  and  $\overline{ZX}$ , whose endpoints  $X$  and  $Y$  are adjacent to the vertex  $(XY)$ . This proves the proposition.  $\square$

**Corollary 5.3**  *$T = 8$  in the octagonoid-I isomorphism class of connected perimeters.*

**Proof** Perimeters in the octagonoid-I perimeter class are hexagons since they have  $n = 8$  edge crossings. By inspection, we see that the hexagon on the right of Fig. 5.1 is in the form of the hexagon in Proposition 5.3, with  $X = S$  and  $Y = W$ . Let  $f_1$  and  $f_2$  denote the two faces of the cell that have 4 edge crossings. This implies that a valid triangulation for a perimeter in the hexagonoid-I class (case 12 with  $f = 2$ ), such as the one depicted in the right of Fig. 5.1, includes the two diagonals joining the unique vertex that does not belong to  $f_1$  or  $f_2$  with the two vertices adjacent to the unique vertex that belongs to both  $f_1$  and  $f_2$  (the two heavy lines in the right octagon of Fig. 5.1). There are exactly  $2^3 = 8$  distinct triangulations resulting from the inclusion of

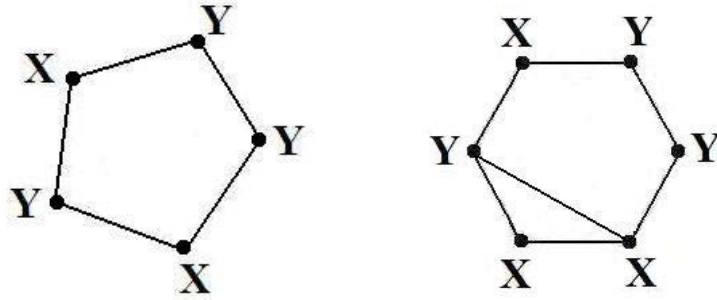


Figure 5.6: Illustration of Lemmas 5.2 (left) and 5.3 (right). For the hexagon of Lemma 5.3 (right), we show the only valid choice for the first diagonal, which results from applying Lemma 5.1 at the  $Y$  vertex adjacent to the two  $X$  vertices. This leads to the pentagon of Lemma 5.2 (left).

both  $\overline{ZY}$  and  $\overline{ZX}$  (where  $X$  and  $Y$  are adjacent to  $(XY)$ ) as first and second diagonals, namely those resulting from the two possible triangulations in each of the three distinct quadrilaterals on either side of the diagonals. As a result, the number of valid triangulations in the octagonoid-I perimeter class is  $T = 8$ .  
 $\square$

We now show some intermediary results (Lemmas 5.2 through 5.5) which are used in the subsequent derivations of  $T$  values. For three of the next four perimeter classes in cases 13, 7, and 14, with  $f = 2, 3, 6$ , we find that  $T = 0$ . Any triangulation for these cases necessarily violates the validity condition of Definition 3.2 due to the high number of constraints.

**Lemma 5.2** *The pentagon  $XY YXY$ , where  $X, Y \in \{N, S, E, W, U, D\}$ , has no valid triangulations.*

**Proof** The pentagon  $XY YXY$  is depicted on the left of Fig. 5.6. From Lemma 5.1, we have that a valid triangulation of  $XY YXY$  must include a diagonal starting at the  $Y$  vertex adjacent to both  $X$  vertices. Since there are no such diagonals which are valid (both possible choices are the two diagonals  $\overline{YY}$ ), we conclude that the pentagon  $XY YXY$  has no valid triangulations.  $\square$

**Lemma 5.3** *The hexagon  $XXYYXY$ , where  $X, Y \in \{N, S, E, W, U, D\}$ , has no valid triangulations.*

**Proof** The hexagon  $XXYYXY$  is depicted on the right of Fig. 5.6. Starting at the  $Y$  vertex adjacent to the two  $X$  vertices (the left vertex  $Y$  in Fig. 5.6), we are forced, as a result of lemma 5.1, to insert the diagonal  $\overline{XY}$  shown in Fig. 5.6 as the first valid diagonal. At this stage we are left with the pentagon  $XYXY Y$ . From Lemma 5.2, we conclude that the hexagon  $XXYYXY$  has no valid triangulations.  $\square$

**Lemma 5.4** *The heptagon  $XXYYZ(XY)Z$ , where  $X, Y, Z \in \{N, S, E, W, U, D\}$ , has no valid triangulations.*

**Proof** The heptagon  $XXYYZ(XY)Z$  is depicted on the left of Fig. 5.7. From Lemma 5.1, we have that a valid triangulation of  $XXYYZ(XY)$  must include a diagonal starting at the  $(XY)$  vertex, which is adjacent to two  $Z$  vertices. Since there are no such diagonals which are valid (the four possible choices are diagonals  $\overline{AA}$ , where  $A \in \{X, Y\}$ ), we conclude that the heptagon  $XXYYZ(XY)Z$  has no valid triangulations.  $\square$

**Lemma 5.5** *The octagon  $XXYYZZ(XY)Z$ , where*

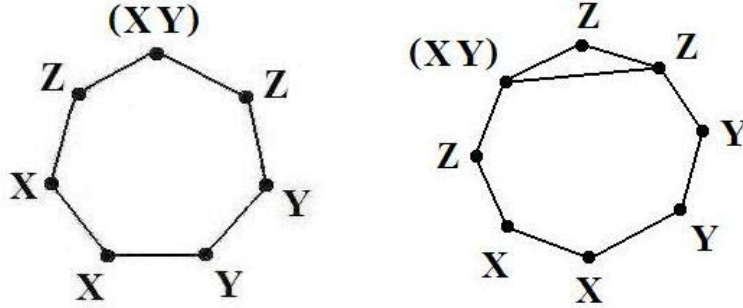


Figure 5.7: Illustration of Lemmas 5.4 (left) and 5.5 (right). For the octagon of Lemma 5.5 (right), we show the only valid choice for the first diagonal, which results from applying Lemma 5.1 at the  $(XY)$  vertex. This leads to the heptagon of Lemma 5.4 (left).

$X, Y, Z \in \{N, S, E, W, U, D\}$ , has no valid triangulations.

**Proof** The octagon  $XXYYZZ(XY)Z$  is depicted on the right of Fig. 5.7. From Lemma 5.1, we have that a valid triangulation of  $XXYYZZ(XY)Z$  must include a diagonal starting at the  $(XY)$  vertex, which is adjacent to two  $Z$  vertices. There is only one valid choice for this diagonal, namely the diagonal  $(XY)Z$  depicted in Fig. 5.7. The insertion of this diagonal results in the heptagon  $XXYYZ(XY)Z$  and so, according to Lemma 5.4, we conclude that the octagon  $XXYYZZ(XY)Z$  has no valid triangulations.  $\square$

**Proposition 5.4** *The octagon  $XXYYXXYY$ , where  $X, Y \in \{N, S, E, W, U, D\}$ , has no valid triangulations.*

**Proof** In Fig. 5.8 we show that no valid triangulation of the octagon  $XXYYXXYY$  can be constructed. We depict all the possible valid choices



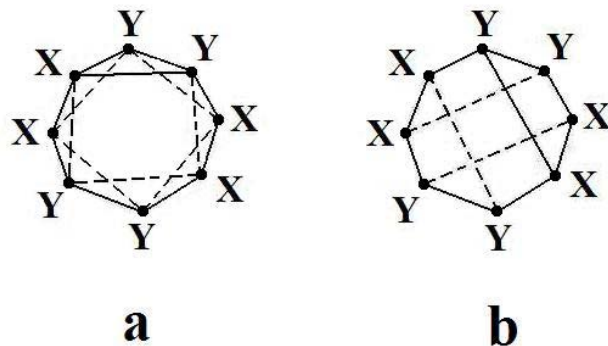


Figure 5.8: Illustration of Proposition 5.4 showing that no valid triangulation of the octagon  $XXYYXXYY$  can be constructed. We show all the possible valid choices for the first diagonal, which are partitioned into two diagonal classes (a, b). Dotted lines show isomorphic choices of diagonals. Note from the many isomorphic choices of diagonals, in both classes, the high number of symmetry axes in this case.

for the first diagonal, which belong to one of two isomorphism classes of diagonals. Any pick from the eight isomorphic choices of diagonals in the first diagonal class (case a in Fig. 5.8) leads to the heptagon  $AABBAAB$ , where  $A, B \in \{X, Y\}$ . From Proposition 5.2, we conclude that the only choice for the second diagonal is an invalid one (either  $\overline{XX}$  or  $\overline{YY}$ ) so that no valid triangulation can be constructed from this class. Any pick from the four isomorphic choices in the second diagonal class (case b in Fig. 5.8) leads to the hexagon  $XXYYXY$ . From Lemma 5.3, we conclude that no valid triangulation can be constructed from this class. Therefore, the octagon  $XXYYXXYY$  has no valid triangulations.  $\square$

**Corollary 5.4**  $T = 0$  in the octagonoid-II isomorphism class of connected perimeters.

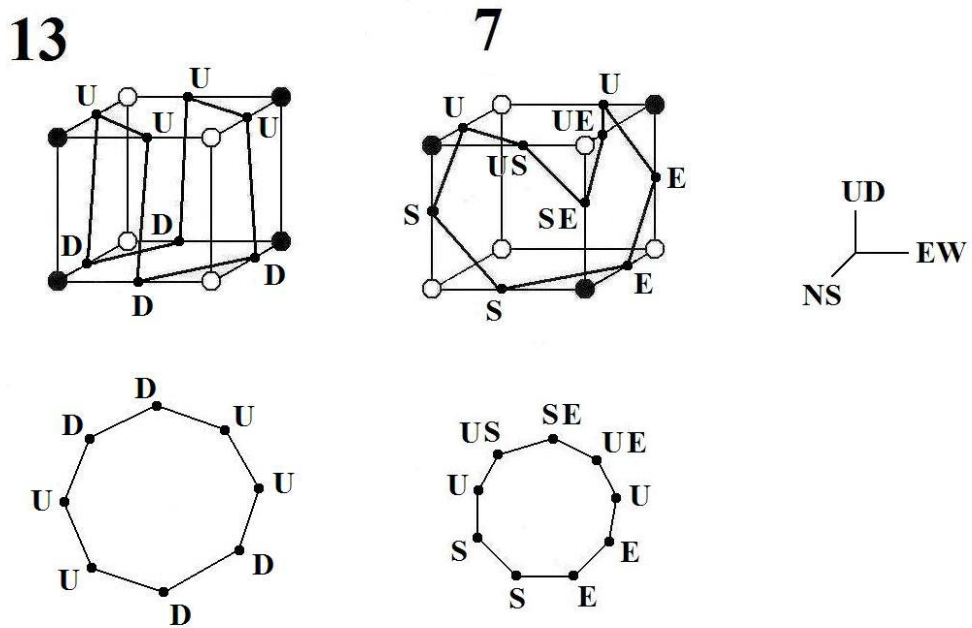


Figure 5.9: Examples of perimeters in the octagonoid-II (left) and enneagonoid (right) isomorphism classes of connected perimeters of cases 13 ( $f = 2$ ) and 7 ( $f = 3$ ). All elements in these two perimeter classes are invalid.

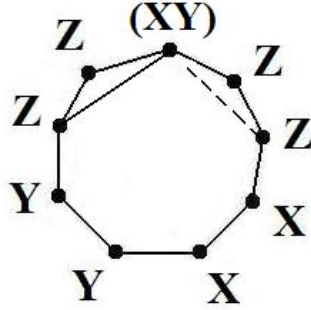


Figure 5.10: Illustration of Proposition 5.5 showing that the enneagon  $XXYYZZ(XY)ZZ$  has no valid triangulations. We depict the two valid isomorphic choices for the first diagonal resulting from applying Lemma 5.1 at the  $(XY)$  vertex.

**Proof** Perimeters in the octagonoid-II perimeter class are octagons since they have  $n = 8$  edge crossings. By inspection, we see that the octagon on the left of Fig. 5.9 is in the form  $XXYYXXYY$  of the octagon in Proposition 5.4, with  $X = D$  and  $Y = U$ . This implies that a perimeter in the octagonoid-II class (case 13 with  $f = 2$ ), such as the one depicted on the left of Fig. 5.9, has no valid triangulations and is necessarily invalid. As a result,  $T = 0$  in the octagonoid-II perimeter class.  $\square$

**Proposition 5.5** *The enneagon  $XXYYZZ(XY)ZZ$ , where  $X, Y, Z \in \{N, S, E, W, U, D\}$ , has no valid triangulations.*

**Proof** The enneagon  $XXYYZZ(XY)ZZ$  is depicted in Fig. 5.10. We can apply Lemma 5.1 at the  $(XY)$  vertex since it is adjacent to two  $Z$  vertices. We then have two isomorphic valid choices for the first diagonal, namely any of the two possible  $\overline{(XY)Z}$  diagonals shown in Fig. 5.10. Any of these choices

leads to the octagon  $(YYXXZZ(XY)Z)$ . From Lemma 5.5, we conclude that the enneagon  $XXYYZZ(XY)ZZ$  has no valid triangulations.  $\square$

**Corollary 5.5**  *$T = 0$  in the enneagonoid isomorphism class of connected perimeters.*

**Proof** Perimeters in the enneagonoid perimeter class are enneagons since they have  $n = 9$  edge crossings. By inspection, we see that the enneagon on the right of Fig. 5.9 is in the form  $XXYYZZ(XY)ZZ$  of the enneagon in Proposition 5.5, with  $X = S$ ,  $Y = E$ , and  $Z = U$ . This implies that a perimeter in the enneagonoid class (case 7 with  $f = 3$ ), such as the one depicted on the right of Fig. 5.9, has no valid triangulations and is necessarily invalid. As a result,  $T = 0$  in the enneagonoid perimeter class.  $\square$

**Proposition 5.6** *The duodecagon  $(XP)PY(YP)(PR)(YR)(YQ)(QR)(XR)(XQ)QX$ , where  $X, Y, P, Q, R \in \{N, S, E, W, U, D\}$ , has no valid triangulations.*

**Proof** The duodecagon  $(XP)PY(YP)(PR)(YR)(YQ)(QR)(XR)(XQ)QX$  is depicted in Fig. 5.11. We apply Lemma 5.1 to vertex  $(YQ)$ , since it is adjacent to two  $R$  vertices, and follow the symmetry about the axis passing through vertices  $(YQ)$  and  $(XP)$ , which separates quintuplets of vertices according to the vertex inversions  $X \leftrightarrow P$  and  $Q \leftrightarrow Y$ . This reduces the number of valid non-isomorphic choices for the first diagonal to 3 (cases a, b, and c in Fig. 5.11). Case a has two isomorphic diagonals. We arbitrarily pick the diagonal  $\overline{(YQ)P}$ , which leads to the hexagon  $YYPPYP$  on the right. From Lemma 5.3, we conclude that no triangulation from this class can be valid.

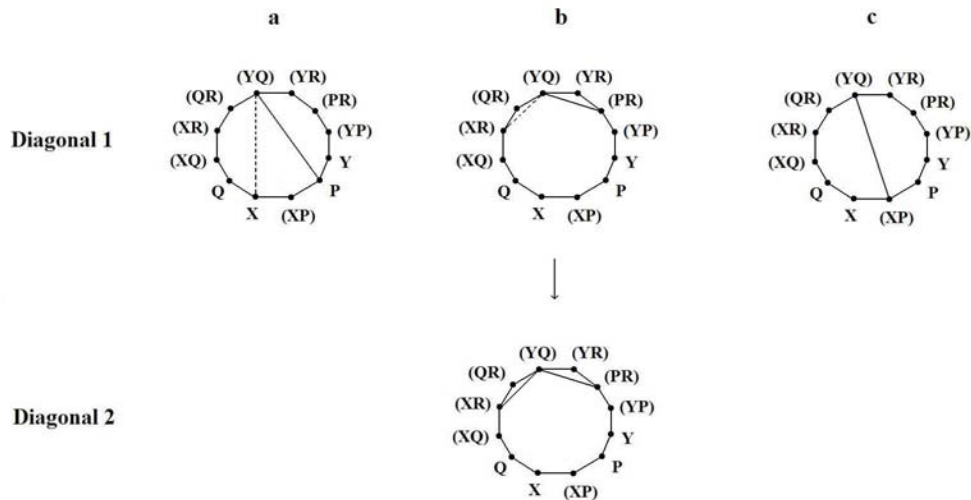


Figure 5.11: Illustration of Proposition 5.6 showing that the duodecagon  $(XP)-PY(YP)(PR)(YR)(YQ)(QR)(XR)(XQ)QX$  has no valid triangulations. Cases a, b, and c depict the three non-isomorphic valid choices for the first diagonal. We also show the only valid possibility for diagonal 2 in case b. Solid lines depict the arbitrary choices of diagonals, while dotted lines depict other isomorphic choices. Note that isomorphic diagonals follow the symmetry about the axis passing through vertices  $(YQ)$  and  $(XP)$ , which separates quintuplets of vertices according to the vertex inversions  $X \leftrightarrow P$  and  $Q \leftrightarrow Y$ .

The only valid choice in case c leads to the heptagon  $YYPPYPP$  on the right. From Proposition 5.2, we infer that the next choice of diagonal must be an invalid one, namely a diagonal  $\overline{YY}$ . We therefore conclude that any triangulation from this class is invalid. Case b has two isomorphic diagonals. We arbitrarily pick the diagonal  $\overline{(YQ)(PR)}$ , which forces the choice of diagonal 2  $\overline{((YQ)(XR))}$  in Fig. 5.11). At this stage we see that any choice for diagonal 3 is an invalid one. We therefore conclude that any triangulation from this class is necessarily invalid. As a result, we conclude that the duodecagon  $(XP)PY(YP)(PR)(YR)(YQ)(QR)(XR)(XQ)QX$  has no valid triangulations.  $\square$

**Corollary 5.6**  *$T = 0$  in the duodecagonoid-I isomorphism class of connected perimeters.*

**Proof** Perimeters in the duodecagonoid-I perimeter class are duodecagons since they have  $n = 12$  edge crossings. By inspection, we see that the duodecagon  $(SD)SU(SU)(SE)(UE)(UN)(NE)(DE)(DN)ND$  on the left of Fig. 3.7 is in the form  $(XP)PY(YP)(PR)(YR)(YQ)(QR)(XR)(XQ)QX$  of the duodecagon in Proposition 5.6, with  $X = D$ ,  $Y = U$ ,  $P = S$ ,  $Q = N$ , and  $R = E$ . This implies that a perimeter in the duodecagonoid-I class (case 14 with  $f = 6$ ), such as the one depicted on the left of Fig. 3.7, has no valid triangulations and is necessarily invalid. As a result,  $T = 0$  in the duodecagonoid-I perimeter class.  $\square$

**Proposition 5.7** *A valid triangulation of the duodecagon  $(XP)(XR)(QR)(YQ)(YZ)(ZQ)(XQ)(XZ)(ZP)(YP)(YR)(PR)$ , where*

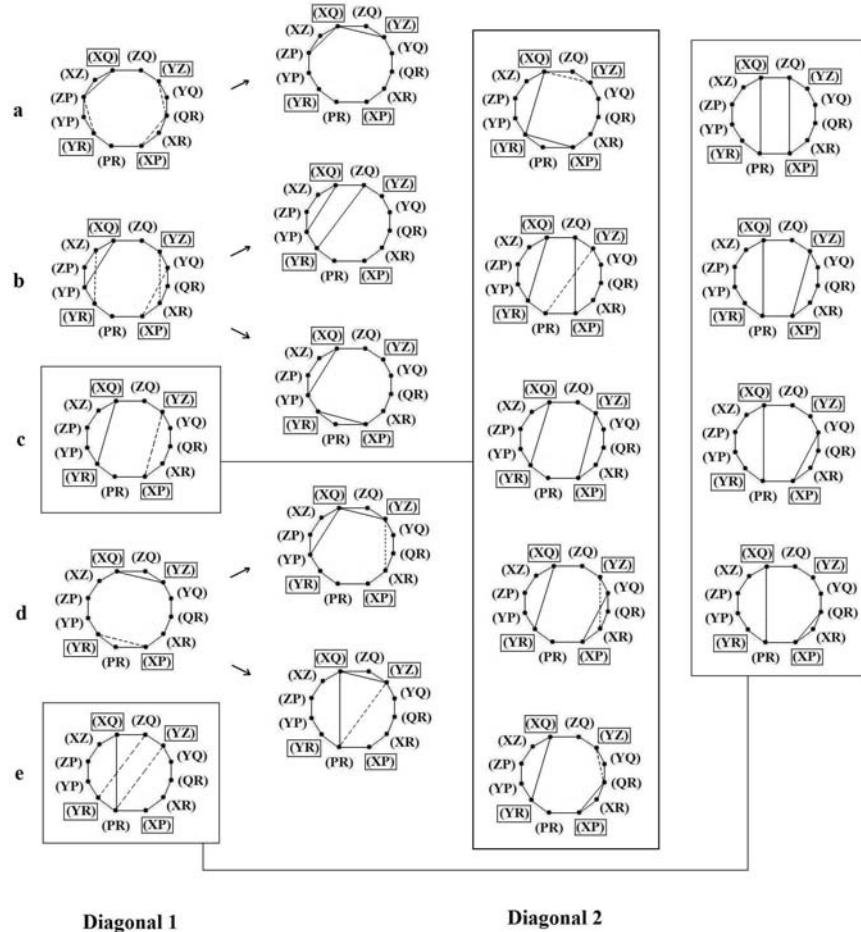


Figure 5.12: Illustration of Proposition 5.7 showing that no valid triangulation of the duodecagon  $(XP)(XR)(QR)(YQ)(YZ)(ZQ)(XQ)(XZ)(ZP)(YP)(YR)(PR)$  can be constructed if the diagonal  $(PR)(ZQ)$ , the triangle  $(YR)(XP)(ZQ)$ , and the triangle  $(YZ)(XQ)(PR)$  are all excluded. The four vertices in boxes have adjacent vertices on a common cell face. We show the five valid isomorphism classes (cases a through e) for the first diagonal, and the valid isomorphism classes for the second diagonal, all resulting from applying Lemma 5.1 at boxed vertices. Dotted lines depict isomorphic choices of diagonals with respect to the two symmetries about the axis passing through vertices  $(ZQ)$  and  $(PR)$  separating two quintuplets of vertices according to the vertex inversions  $X \leftrightarrow Y$ ,  $P \leftrightarrow R$ , and  $Z \leftrightarrow Q$ , and about the axis passing through vertices  $(ZP)$  and  $(QR)$  separating quintuplets of vertices according to the vertex inversions  $X \leftrightarrow Y$ ,  $Z \leftrightarrow P$ , and  $Q \leftrightarrow R$ .

$X, Y, Z, P, Q, R \in \{N, S, E, W, U, D\}$ , must include either the diagonal  $\overline{(PR)(ZQ)}$ , the triangle  $(YR)(XP)(ZQ)$ , or the triangle  $(YZ)(XQ)(PR)$ .

**Proof** In Fig. 5.12 we show that no valid triangulation of the duodecagon  $(XP)(XR)(QR)(YQ)(YZ)(ZQ)(XQ)(XZ)(ZP)(YP)(YR)(PR)$ , where  $X, Y, Z, P, Q, R \in \{N, S, E, W, U, D\}$ , can be constructed if the diagonal  $\overline{(PR)(ZQ)}$ , the triangle  $(YR)(XP)(ZQ)$ , and the triangle  $(YZ)(XQ)(PR)$  are all excluded, as this is equivalent to proving the proposition. As usual, we proceed by inserting only valid diagonals. First, note that there are two symmetries for the duodecagon (before the insertion of diagonal 1) given by, first, the axis passing through the vertices  $(ZQ)$  and  $(PR)$  separating two quintuplets of vertices according to the vertex inversions  $X \leftrightarrow Y$ ,  $P \leftrightarrow R$ , and  $Z \leftrightarrow Q$ , and, second, the axis passing through the vertices  $(ZP)$  and  $(QR)$  separating quintuplets of vertices according to the vertex inversions  $X \leftrightarrow Y$ ,  $Z \leftrightarrow P$ , and  $Q \leftrightarrow R$ . We use these two symmetries to discard isomorphic cases and to show in Fig. 5.12 isomorphic choices of diagonals (dotted lines). Only cases c and d preserve one of the two symmetries after the insertion of diagonal 1. We depict in boxes the four vertices which have adjacent vertices on a common cell face. From Lemma 5.1, we can then force the first diagonal to start at any of these vertices. We arbitrarily pick the vertex  $(XQ)$  for diagonal 1. The resulting valid choices are shown in cases a through e in Fig. 5.12. We also show the isomorphism classes for diagonal 2 only if they are distinct and non-isomorphic to previous cases. Again, we apply Lemma 5.1. at either one of the four boxed vertices to obtain these diagonal classes. We see that in case a, there is only one choice for diagonal 2, while for cases b and d there



are two choices for diagonal 2. Cases c and e have, respectively, five and four choices for diagonal 2. these are all depicted in Fig. 5.12. At this stage in the construction, it is not difficult to see after careful study in each case that no triangulation can be constructed if we exclude either the diagonal  $\overline{(PR)(ZQ)}$ , the triangle  $(YR)(XP)(ZQ)$ , or the triangle  $(YZ)(XQ)(PR)$ .  $\square$

**Corollary 5.7**  *$T = 294$  in the duodecagonoid-II isomorphism class of connected perimeters.*

**Proof** Perimeters in the duodecagonoid-II perimeter class are duodecagons since they have  $n = 12$  edge crossings. By inspection, we see that the duodecagon  $(SD)(ED)(NE)(NU)(WU)(WN)(DN)(DW)(SW)(SU)(UE)(SE)$  on the right of Fig. 3.7 is in the form  $(XP)(XR)(QR)(YQ)(YZ)(ZQ)(XQ)(XZ)(ZP)(YP)(YR)(PR)$  of the duodecagon in Proposition 5.7, with  $X = D$ ,  $Y = U$ ,  $Z = W$ ,  $P = S$ ,  $Q = N$ , and  $R = E$ . This implies that a valid triangulation for a perimeter in the duodecagonoid-II class (case 14 with  $f = 6$ ) follows Proposition 5.7. In Fig. 5.13 we illustrate the three cases resulting from the inclusion of either  $\overline{(PR)(ZQ)}$  as the first diagonal (a), or triangles  $(YR)(XP)(ZQ)$  (b) and  $(YZ)(XQ)(PR)$  (c) as the first three diagonals. In all three cases, we force the first diagonal to start at the vertex  $(YR)$  and only depict the possible triangulations on the left side of the diagonal or triangle that is included, since there is a symmetry about the axis passing through vertices  $(PR)$  and  $(ZQ)$  separating two quintuplets of vertices according to the vertex inversions  $X \leftrightarrow Y$ ,  $P \leftrightarrow R$ , and  $Z \leftrightarrow Q$ . We use boxes to show the four vertices from which a diagonal must start, according to Lemma 5.1, and

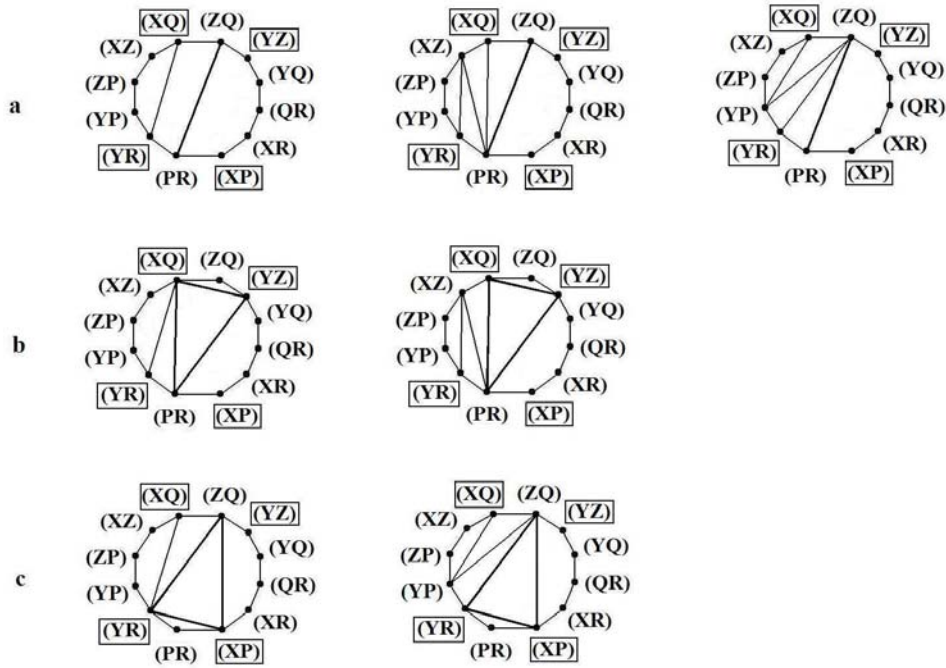


Figure 5.13: Illustration of Corollary 5.7. We show that there are  $T = 294$  valid triangulations for duodecagons in the duodecagonoid-II perimeter class resulting from the inclusion of either the diagonal  $\overline{(PR)(ZQ)}$  (a), the triangle  $(YR)(XP)(ZQ)$  (b), or the triangle  $(YZ)(XQ)(PR)$  (c). We depict in boxes the four vertices from which a diagonal must start, according to Lemma 5.1, and with heavy lines the diagonal or triangle that has been included. We only show the possible triangulations on the left side of the diagonal or triangle that is included, since there is a symmetry about the axis passing through vertices  $(PR)$  and  $(ZQ)$  separating two quintuplets of vertices according to the vertex inversions  $X \leftrightarrow Y$ ,  $P \leftrightarrow R$ , and  $Z \leftrightarrow Q$ . In all three cases, we force the first diagonal on the left to start at the vertex  $(YR)$ .

heavy lines to show the diagonal or triangle that has been included.

When the diagonal  $\overline{(PR)(ZQ)}$  is included (case a in Fig. 5.13, there are three cases: the first case, which includes the diagonal  $\overline{(YR)(XQ)}$ , results in  $5 \times 2$  triangulations corresponding to both the pentagon and the quadrilateral on the left and right of  $\overline{(YR)(XQ)}$ ; the second case, which includes the diagonal  $\overline{(YR)(XZ)}$ , results in 2 triangulations from the quadrilateral on the left of  $\overline{(YR)(XZ)}$  since  $\overline{(PR)(XZ)}$  and  $\overline{(PR)(XQ)}$  have to be included as well; the third case, which includes the diagonal  $\overline{(YR)(ZQ)}$ , results in 2 triangulations from the quadrilateral on the left of  $\overline{(YR)(ZQ)}$  since  $\overline{(ZQ)(YP)}$  and  $\overline{(YP)(XQ)}$  have to be also included. Note that the cases which include the diagonals  $\overline{(YR)(ZP)}$  and  $\overline{(XQ)(ZP)}$  lead to cases b and c and are, thus, not treated separately. From the inclusion of  $\overline{(PR)(ZQ)}$  as the first diagonal, we thus have a total number of  $((5 \times 2) + 2 + 2)^2 = 14^2 = 196$  valid triangulations. The squaring operation accounts for the triangulations on the right of  $\overline{(PR)(ZQ)}$  and is a result of the symmetry we have identified above.

When the triangle  $(YR)(XP)(ZQ)$  is included (case b in Fig. 5.13), there are two cases: the first includes the diagonal  $\overline{(YR)(XQ)}$  and results in 5 triangulations from the pentagon on the left of  $\overline{(YR)(XQ)}$ , while the second includes the diagonal  $\overline{(YR)(XZ)}$  and results in 2 triangulations from the quadrilateral on the left of  $\overline{(YR)(XZ)}$  since diagonal  $\overline{(XZ)(PR)}$  must also be included. Therefore, the inclusion of triangle  $(YR)(XP)(ZQ)$  as the first three diagonals results in a total number of  $(5 + 2)^2 = 7^2 = 49$  valid triangulations.

When the triangle  $(YZ)(XQ)(PR)$  is included (case c in Fig. 5.13), there are also a total number of  $(5 + 2)^2 = 7^2 = 49$  valid triangulations. In effect,

cases b and c are isomorphic and follow a second symmetry about the axis passing through vertices  $(ZP)$  and  $(QR)$  separating two quintuplets of vertices according to the vertex inversions  $X \leftrightarrow Y$ ,  $Z \leftrightarrow P$ , and  $Q \leftrightarrow R$ .

As a result of these three cases, we have a total number of  $196 + 2(49) = 294$  distinct valid triangulations resulting from the inclusion of either  $\overline{(PR)(ZQ)}$  as the first diagonal, or triangles  $(YR)(XP)(ZQ)$  and  $(YZ)(XQ)(PR)$  as the first three diagonals. This proves our claim that  $T = 294$  in the duodecagonoid-II isomorphism class of connected perimeters.  $\square$

This concludes the proof of Proposition 3.6.  $\square$

## Bibliography

- [1] R. Abgrall and R. Sorell. Discrete equations for physical and numerical compressible multiphase mixtures. *J. Comp. Phys.*, 186:361–396, 2003.
- [2] W. Bo, B. Cheng, J. Du, B. Fix, E. George, J. Glimm, J. Grove, X. Jia, H. Jin, H. Lee, Y. Li, X. Li, X. Liu, D. H. Sharp, L. Wu, and Yan Yu. Recent progress in the stochastic analysis of turbulent mixing. *Contemporary Mathematics*, 2005. Submitted. Stony University Preprint Number SUNYSB-AMS-05-18, Los Alamos National Laboratory LAUR Number LAUR-05-7102.
- [3] W. Bo, H. Jin, D. Kim, X. Liu, H. Lee, J.N. Pestieau, Y. Yu, J. Glimm, and J. W. Grove. Compressible multi species multiphase flow models. *Phys. Rev. E*, 2007. Submitted. Stony Brook University Preprint Number SUNYSB-AMS-07-02, Los Alamos National Laboratory LAUR Number LAUR-07-1964.
- [4] M. Brouillette. The Richtmyer-Meshkov instability. *Annu. Rev. Fluid Mech.*, 34:445–68, 2002.
- [5] B. Cheng. An overview of mix models. Technical report, Los Alamos National Laboratory, Los Alamos, NM 87545, 2005.
- [6] B. Cheng, J. Glimm, D. Saltz, and D. H. Sharp. Boundary conditions for a two pressure two phase flow model. *Physica D*, 133:84–105, 1999.
- [7] B. Cheng, J. Glimm, and D. H. Sharp. Density dependence of Rayleigh-Taylor and Richtmyer-Meshkov mixing fronts. *Phys. Lett. A*, 268:366–374, 2000.
- [8] B. Cheng, J. Glimm, and D. H. Sharp. A 3-D RNG bubble merger model for Rayleigh-Taylor mixing. *Chaos*, 12:267–274, 2002.

- [9] B. Cheng, J. Glimm, and D. H. Sharp. Dynamical evolution of the Rayleigh-Taylor and Richtmyer-Meshkov mixing fronts. *Phys. Rev. E*, 66:1–7, 2002. Paper No. 036312.
- [10] B. Cheng, J. Glimm, D. H. Sharp, and Y. Yu. A multiphase flow model for the unstable mixing of layered incompressible materials. *Phys. of Fluids*, 17, 2005. Paper No. 087102. LANL Preprint Number LA-UR-05-0078. Stony Brook University Preprint Number SUNYSB-AMS-05-01.
- [11] D. A. Drew. Mathematical modeling of two-phase flow. *Ann. Rev. Fluid Mech.*, 15:261–291, 1983.
- [12] E. George and J. Glimm. Self similarity of Rayleigh-Taylor mixing rates. *Phys. Fluids*, 17:054101, 2005. Stony Brook University Preprint number SUNYSB-AMS-04-05.
- [13] E. George, J. Glimm, X. L. Li, Y. H. Li, and X. F. Liu. The influence of scale-breaking phenomena on turbulent mixing rates. *Phys. Rev. E*, 2005. In Press. Stony Brook University Preprint number SUNYSB-AMS-05-11.
- [14] E. George, J. Glimm, X. L. Li, A. Marchese, and Z. L. Xu. A comparison of experimental, theoretical, and numerical simulation Rayleigh-Taylor mixing rates. *Proc. National Academy of Sci.*, 99:2587–2592, 2002.
- [15] J. Glimm, J. W. Grove, X.-L. Li, and D. C. Tan. Robust computational algorithms for dynamic interface tracking in three dimensions. *SIAM J. Sci. Comp.*, 21:2240–2256, 2000.
- [16] J. Glimm, H. Jin, M. Laforest, F. Tangerman, and Y. Zhang. A two pressure numerical model of two fluid mixing. *SIAM J. Multiscale Model. Simul.*, 1:458–484, 2003.
- [17] J. Glimm, D. Saltz, and D. H. Sharp. Renormalization group solution of two-phase flow equations for Rayleigh-Taylor mixing. *Phys. Lett. A*, 222:171–176, 1996.
- [18] J. Glimm, D. Saltz, and D. H. Sharp. Two-pressure two-phase flow. In G.-Q. Chen, Y. Li, and X. Zhu, editors, *Nonlinear Partial Differential Equations*, pages 124–148. World Scientific, Singapore, 1998.
- [19] J. Glimm, D. Saltz, and D. H. Sharp. Two-phase modeling of a fluid mixing layer. *J. Fluid Mech.*, 378:119–143, 1999.

- [20] J. M. Harris, J. L. Hirst, and M. J. Mossinghoff. *Combinatorics and Graph Theory*. Springer-Verlag, New York, U.S.A., 2000.
- [21] H. Jin, J. Glimm, and D. H. Sharp. Two-pressure two-phase flow models. *Phys. Lett. A*, 2005. In press. Stony Brook University Preprint number SUNYSB-AMS-05-19 and Los Alamos National Laboratory LAUR Number LA-UR-05-7229.
- [22] H. Jin, X. F. Liu, T. Lu, B. Cheng, J. Glimm, and D. H. Sharp. Rayleigh-Taylor mixing rates for compressible flow. *Phys. Fluids*, 17:024104–1–024104–10, 2005. Stony Brook University Preprint number SUNYSB-AMS-04-06 and Los Alamos National Laboratory LAUR Number LA-04-1384.
- [23] R. E. Kidder. Inertial fusion energy. *Nucl. Fusion*, 14:797, 1974.
- [24] D. Kim, J. N. Pestieau, and J. Glimm. Volume fractions and surface areas for 3-D grid cells cut by an interface. Technical Report SUNYSB-AMS-07-01, State Univ. of New York at Stony Brook, 2007.
- [25] Gabriel Lamé. Extrait d’une lettre de M. Lamé à M. Liouville sur cette question: Un polygone convexe étant donné, de combien de manières peut-on le partager en triangles au moyen de diagonales? *Journal de Mathématiques Pures et Appliquées (Journal de Liouville)*, 3:505–507, 1838.
- [26] D. Layzer. On the instability of superimposed fluids in a gravitational field. *Astrophys. J.*, 122:1–12, 1955.
- [27] T. Lee, Y. Yu, M. Zhao, J. Glimm, X. Li, and K. Ye. Error analysis of composite shock interaction problems. *Conference Proceedings of PMC04*, 2004. University at Stony Brook Preprint Number SB-AMS-04-08.
- [28] G. H. Markstein. Flow disturbances induced near a slightly wavy contact surface, or flame front, traversed by a shock wave. *J. Aero. Sci.*, pages 238–39, 1957.
- [29] E. E. Meshkov. Instability of the interface of two gases accelerated by a shock wave. *Izv. Akad. Nauk SSSR, Mekh. Zhidk. Gaz.*, 5:151, 1969.
- [30] J. O’Rourke. *Computational Geometry in C*. Cambridge University Press, Cambridge, U.K., 1994.

- [31] G. Polya and R. C. Reade. *Combinatorial Enumeration of Groups, Graphs and Chemical Compounds*. Springer-Verlag, New York, U.S.A., 1987.
- [32] K. I. Read. Experimental investigation of turbulent mixing by Rayleigh-Taylor instability. *Physica D*, 12:45–58, 1984.
- [33] R. D. Richtmyer. Taylor instability in shock acceleration of compressible fluids. *Comm. Pure Appl. Math.*, 13:297–319, 1960.
- [34] R. Saurel and R. Abgrall. A multiphase godunov method for compressible multifluid and multiphase flows. *J. Comput. Phys.*, 150:425–467, 1999.
- [35] R. Saurel, O. Le Metayer, J. Massoni, and S. Gavrilyuk. Shock jump relations for multiphase mixtures with stiff mechanical properties. 2005.
- [36] V. S. Smeeton and D. L. Youngs. Experimental investigation of turbulent mixing by Rayleigh-Taylor instability (part 3). AWE Report Number 0 35/87, Atomic Weapons Establishment (AWE), 1987.
- [37] G. I. Taylor. The instability of liquid surfaces when accelerated in a direction perpendicular to their planes I. *Proc. R Soc. London A*, 201:192–196, 1950.
- [38] A. Tucker. *Applied Combinatorics*. John Wiley and Sons, New York, U.S.A., 1995.
- [39] Y. Yu, M. Zhao, T. Lee, N. Pestieau, W. Bo, J. Glimm, and J. W. Grove. Uncertainty quantification for chaotic computational fluid dynamics. *J. Comp. Phys.*, 2005. Stony Brook Preprint number SB-AMS-05-16 and LANL preprint number LA-UR-05-6212; submitted.